uOttawa

Attosecond *In Situ* Measurement and Recombination

Graham Gardiner Brown

A thesis submitted in partial fulfillment of the
requirements for the Doctorate in Philosophy
degree in Physics

Department of Physics
Faculty of Science
University of Ottawa

Supervisor : Dr. Paul Bruce Corkum

Abstract

The spectral phase of high harmonic and attosecond pulses is typically shaped by the interaction of the recollision electron with the strong field in the continuum. However, the phase of the transition moment coupling bound and continuum states can be significant in shaping the emitted radiation. The measurement of transition moment phase shifts can reveal information about attosecond electron dynamics and structure. Here, I demonstrate that all-optical approaches to attosecond measurement, based on perturbing recollision with a weak infrared field, are sensitive to transition moment phase shifts arising from electronic structure and multielectron interaction using analytical theory, *ab initio* simulation, and experiment. The insensitivity of all-optical approaches to transition moment phase shifts arising from ionic structure is found to be a result of a first-order cancellation of the effect of the perturbing field on the recollision electron wave packet and the transition moment. Prior to these findings, it was widely believed that all-optical methods were insensitive to the transition moment phase. The insensitivity of all-optical measurement to both ionic structure and propagation effects will permit for the unambiguous isolation of electron structure and multielectron interaction in attosecond measurement. These results will allow any laboratory capable of generating attosecond pulses to perform measurements of the transition moment phase without an additional experimental apparatus, even at wavelengths where the single photoionization cross-section becomes small.

Résumé

La phase spectrale des impulsions harmoniques d'ordre élevé et attosecondes est généralement façonnée par l'interaction de l'électron de recollision avec le champ fort dans le continuum. Cependant, la phase du moment de transition couplant les états liés et le continuum peut jouer un rôle important dans la formation du rayonnement émis. La mesure des décalages de phase du moment de transition peut révéler des informations sur la dynamique et la structure des électrons attoseconde. Je démontre ici que les approches tout-optiques de la mesure attoseconde, basées sur la perturbation de la recollision avec un faible champ infrarouge, sont sensibles aux déphasages du moment de transition provenant de la structure électronique et de l'interaction multi-électronique en utilisant la théorie analytique, la simulation ab initio et l'expérience. L'insensibilité des approches tout-optique aux déphasages du moment de transition résultant de la structure ionique est le résultat d'une annulation de premier ordre de l'effet du champ perturbateur sur le paquet d'ondes électronique de recollision et le moment de transition. Avant ces résultats, on pensait généralement que les méthodes tout-optiques étaient insensibles à la phase du moment de transition. L'insensibilité de la mesure tout-optique à la structure ionique et aux effets de propagation permettra d'isoler sans ambiguïté la structure électronique et l'interaction multi-électronique dans la mesure de l'attoseconde. Ces résultats permettront à tout laboratoire capable de générer des impulsions attosecondes d'effectuer des mesures de la phase du moment de transition sans appareil expérimental supplémentaire, même à des longueurs d'onde où la section transversale de photoionisation unique devient faible.

Acknowledgements

Despite my name appearing alone as the author of this thesis, scientific research is rarely a solitary endeavour. The ideas presented here are the result of years of working in an environment with some of the most brilliant people I have had the pleasure of meeting. Some people contributed directly to the development this thesis and others in indirect, yet important, ways.

I'd first like to thank my supervisor, Paul, for his unwavering support. My discussions with him throughout my PhD changed how I think about and approach science. His spirited, collaborative, and open approach to research and new ideas are things I hope to take with me as I move onto the next phase of my research career. Despite working in an experimental group, my studies took an unexpected turn towards theory. The catalysts for this were years-long equipment delays and a regrettably intense exposure to Newtonian mechanics. During these times, I honed my theoretical skills in describing strong field dynamics in multielectron systems. Paul supported my efforts constantly and encouraged me to chase whichever idea interested me at the time, so long as I was chasing a good one. Working in Paul's group, I benefitted from independence, which allowed me to forge my own path, but I also benefitted from Paul's expert guidance which provided me with the necessary direction that inexperienced researchers lack. His influence on this work is everywhere and can hardly be summarized in a single paragraph. I'm profoundly grateful to him for giving me the opportunity to work in this wonderful group and everything he has done for me.

I'd also like to thank the colleagues who contributed directly to this work. In no order of importance, the first I will mention is Dong Hyuk Ko. He has been a fantastic mentor, teacher, and friend during my time here. He is always ready to help anyone in the lab and I benefitted from his expertise countless times. Most importantly, he was the person who first showed me the power of massively parallel computation which ended up being the computational foundation of this thesis. Our kimchi nights at Alirang are some of my favourite memories from my time here.

The second person directly involved with this work who I'd like to thank is Chunmei Zhang. Her experimental work studying the Cooper minimum in argon is what propelled our subgroup into taking a closer look at attosecond *in situ* measurement and the transition moment phase. She is a master with laser and OPA systems and, again, I learned a great deal from her in the lab. Although my theoretical work provided a much needed foundation

for our conclusions, it would not have been possible without her work. Her contribution cannot be overstated. She has been a superb colleague, mentor, and friend.

The rest of our group, with whom I did not work as closely, was also important in the development of my research. The Attoscience group at the National Research Council and the University of Ottawa is a wonderfully comfortable and happy working environment with no shortage of brilliant minds. Through late night discussions and work sessions, the exchange of ideas and friendship, Fanqi Kong, Mathew Briton, Alan Godfrey, Martin Chiasson, and others made my PhD work enjoyable and stimulating. The rest of the group with whom I did not work, mostly based at NRC, exposed me to many new ideas and ways of thinking. In particular, Andre Staudte's steadfast commitment to convening the groups at the University of Ottawa and National Research Council for regular meetings exposed me to countless interesting ideas and people and helped me develop as a public speaker.

I also need to thank the people in my life not involved in research. My partner Aybüke Özel provided unwavering support and tolerance for my nearly nocturnal lifestyle during the final days of my PhD. Now that this is done, I promise I will (mostly) sleep like a normal person. My grandmother, Helen, ingrained in me a love of reading and my grandfather, Colin, taught me the joy of tinkering with things, both of which have proven invaluable in my research. My mother, Karen, and my siblings Laura and Evan provided constant love and support throughout my life, without which I could not have finished this.

Contents

List of Acronyms

APT attosecond pulse train. 20, 21

C-SFA correlated strong field approximation. 105, 107, 110, 111

DFT density functional theory. 40–44, 54, 87, 88, 100

FROG frequency-resolved optical gating. 23, 32

GDR giant dipole resonance. 98–102, 105, 110

GGA generalized gradient approximation. 42

GP-GPU general-purpose graphical processing unit. 47, 57

HHG high-harmonic generation. 2, 5, 17, 28, 34, 35, 60, 80, 84, 85, 95, 108, 112, 115

JASLAB Joint Attosecond Science Laboratory. 24

LB94 Leeuwen-Baerends density functional. 42, 43, 53, 87, 88, 99, 100

LDA local-density approximation. 42, 53

QRS quantitative rescattering theory. 16, 17, 35, 36, 59, 61

RABBIT Reconstruction of Attosecond Beating by Interference of Two-Photon Transitions. 20–23, 26, 65

SAE single-active electron. 7, 8, 85, 88

SFA strong field approximation. 3, 6, 9, 15, 16, 18, 23, 25, 36, 59, 60, 63, 65, 71, 72, 75, 80, 92, 93, 97, 99, 101, 103, 104, 106, 108, 111, 112, 114

TD-DFT time-dependent density functional theory. 43, 44, 53, 56, 62, 87, 89, 91, 93, 95, 96, 99–101, 110–112

TDSE time-dependent Schrödinger equation. 3, 7, 16, 28, 29, 44, 65, 73, 77, 78, 83, 110

XUV extreme ultraviolet. 3, 4, 20, 21, 23–25, 30–33, 76, 79, 80, 95, 115

List of Figures

List of Tables

Complete List of Publications

Authors with an asterisk (∗) contributed equally to the manuscript.

Unpublished

— C. Zhang*, **G. G. Brown***, D. H. Ko, P. B. Corkum. Optical Measurement of Photorecombination Time Delays. *Nature Photonics* (in review)

— **G. G. Brown**, D. H. Ko, P. B. Corkum, C. Zhang. Attosecond Measurement via High Harmonic Generation in Low Frequency Fields. *Physical Review A* (in review)

— **G. G. Brown**, D. H. Ko, P. B. Corkum, C. Zhang. Measuring and Controlling Resonance-Enhanced Recollision with Infrared Fields. Physical Review X (submitted)

— D. H. Ko, **G. G. Brown**, C. Zhang, P. B. Corkum. Near-field imaging of dipole emission modulated by an optical grating. Optica (in review)

— **G. G. Brown**, D. H. Ko, P. B. Corkum, C. Zhang. Characterizing Many-Body Dynamics by Perturbing Electron-Ion Collisions with Infrared Fields. (in preparation)

Published

— D. H. Ko, **G. G. Brown**, Chunmei Zhang, P. B. Corkum. Delay Measurement of Attosecond Emission in Solids. Journal Of Physics B: Atomic, Molecular And Optical Physics 53, 124001 (2020)

— J. Li, Y. Wang, T. Guo, J. White, M. Weidman, Y. Wu, K. Hu, M. F. Jager, C. J. Kaplan, R. Geneaux, D. M. Neumark, S. R. Leone, **Graham G. Brown**, P. B. Corkum, Z. Chang. Beam Optimization in a 25 TW Femtosecond Laser System for High Harmonic Generation. Journal Of Physics B: Atomic, Molecular And Optical Physics 53, 145602 (2020)

— F. Kong, C. Zhang, H. Larocque, F. Bouchard, Z. Li, M. Taucer, **G. G. Brown**, S. Severino, T. J. Hammond, E. Karimi, P. B. Corkum. Spin-Constrained Orbital-Angular-Momentum Control in High-Harmonic Generation. Physical Review Research 1, 032008 (2019)

— F. Kong, C. Zhang, H. Larocque, Z. Li, F. Bouchard, D. H. Ko, **G. G. Brown**, A. Korobenko, T. J. Hammond, R. W. Boyd, E. Karimi, P. B. Corkum. Vectorizing the

Spatial Structure of High-Harmonic Radiation from Gas. Nature Communications 10, 2020 (2019)

— M. Britton, P. Laferrière, D. H. Ko, Z. Li, F. Kong, **G. G. Brown**, A. Naumov, C. Zhang, L. Arissian, P. B. Corkum. Testing the Role of Recollision in N_2^+ Air Lasing. Phys. Rev. Lett. 120, 133208 (2018)

— Z. Li, F. Kong, **G. G. Brown**, T. J. Hammond, D. H. Ko, C. Zhang, P. B. Corkum. Perturbing laser field dependent high harmonic phase modulations. Journal Of Physics B: Atomic, Molecular And Optical Physics **51**, 125601 (2018)

— F. Kong, C. Zhang, F. Bouchard, Z. Li, **G. G. Brown**, D. H. Ko, T. J. Hammond, L. Arissian, R. W. Boyd, E. Karimi and P. B. Corkum. Controlling the orbital angular momentum of high harmonic vortices. Nat Commun 8, 14970 (2017)

— Z. Li, **G. G. Brown**, D. H. Ko, F. Kong, L. Arissian, and P. B. Corkum. Perturbative High Harmonic Wave Front Control. Phys. Rev. Lett. **118**, 033905

— T. J. Hammond, **G. G. Brown**, K. T. Kim, D. M. Villeneuve, P. B. Corkum,. Attosecond pulses measured from the attosecond lighthouse. Nature Photon **10**, 171-175 (2016)

— T. J. Hammond, S. Monchocé, C. Zhang, **G. G. Brown**, P. B. Corkum, and D. M. Villeneuve. Femtosecond time-domain observation of atmospheric absorption in the near-infrared spectrum. Phys. Rev. A **94**, 063410

— C. Zhang, **G. G. Brown**, K. T. Kim, D. M. Villeneuve, P. B. Corkum. Full characterization of an attosecond pulse generated using an infrared driver. Sci Rep **6**, 26771 (2016)

Part I

Introduction

Chapter 1

Introduction

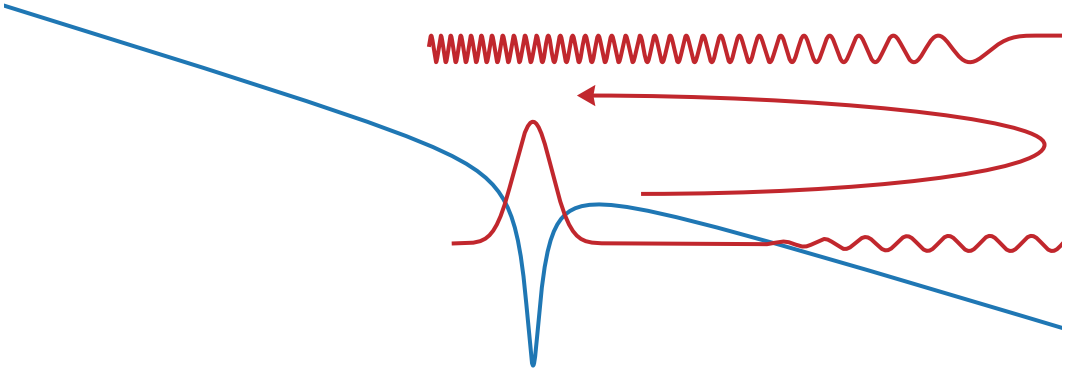

Figure 1.1 – When subjected to an intense field, an electron (red) bound by an ionic potential (blue) can tunnel into the continuum, depicted by the lower oscillating red curve. The resultant wavefunction consists of bound and freed components. Accelerated by the field, the continuum portion of the electron wavefunction can return (upper oscillating red curve) to its parent ion and interfere with the bound component. This interference leads to a rapidly oscillating dipole moment and the emission of attosecond pulses.

Interference is one of the most fundamental means through which physical processes are measured and is a characteristic of the wave-particle duality which distinguishes quantum mechanical and classical descriptions of matter. Recollision, a process often described using classical language [1], is a result of quantum interference [2]. This is depicted in Fig. 1.1. When a sufficiently strong electric field is incident on a quantum system, an electron (red) bound by a potential (blue) may tunnel into the continuum, resulting in a wavefunction containing both bound and free components. Once freed, the component of the electron wavefunction in the continuum is accelerated by the strong field (red arrow) and is first driven away from its parent ion and then driven back towards it. As the continuum wave packet overlaps with its parent ion, the interference of the bound and freed components of the wavefunction results in a rapidly oscillating dipole moment. The radiation emitted by this process, known as high-harmonic generation (HHG), can span huge bandwidths, and

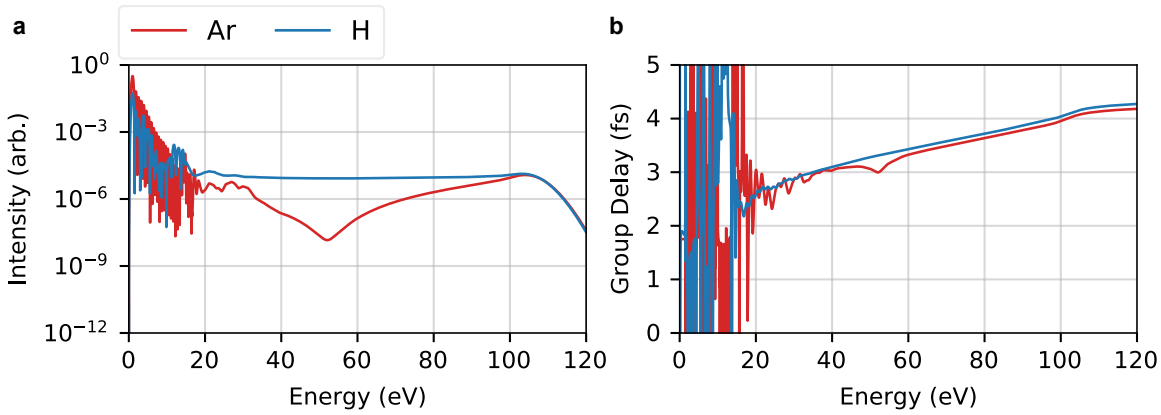

Figure 1.2 – (a) The attosecond pulse spectra generated by a single-cycle driving field of wavelength 1.8 µm and peak intensity of 1×10^{14} W/cm^2 from a hydrogenic atom with a nuclear charge of 1.078 (blue) and an argon atom (red). Both atoms have an ionization potential of 15.8 eV. The hydrogenic atom has a slowly varying transition moment and its spectrum exhibits a broad plateau until the cutoff energy near 100 eV. The argon atom, however, exhibits a spectral minimum near 50 eV in its transition moment and attosecond pulse spectrum known as the Cooper minimum. (b) The group delay of the attosecond pulse spectra in (a). The hydrogenic atom group delay varies linearly with energy throughout the plateau and is shifted for clarity. The group delay of argon is similar to that from hydrogenic atom, but exhibits a deviation from the linear group delay around 50 eV due to the Cooper minimum. Short trajectories are selected through the use of absorbing boundaries [5].

has become a widely used source of coherent XUV and soft X-ray light and attosecond pulses.

Our understanding of recollision comes from the theoretical work of Kulander *et al.* [3] and the publication of the seminal three-step model by Corkum in 1993 [1]. These works showed that an electron which tunnels into the continuum in the presence of a strong field follows trajectories dictated by the field, recollides with its parent ion, and emits an XUV photon (see Appendix B). Shortly after, a quantum mechanical theory, which has become known as the strong field approximation (SFA) or the Lewenstein model, placed the classical model on a rigorous quantum mechanical foundation [2]. A path-integral approach [4] to solving the time-dependent Schrödinger equation (TDSE) within this model gives rise to recollision trajectories which coincide with those from the classical model. Components of the continuum electron wavefunction which deviate from these classical trajectories are suppressed by destructive interference. Only the components of the recollision electron wave packet which resemble classical trajectories interfere constructively and contribute to the observed dipole radiation.

In most systems, these dominant components and, thereby, the spectral phase of the emitted radiation are typically determined by the interaction of the continuum electron with the strong field. This gives rise to an inherent quadratic chirp in attosecond pulses com-

monly known as the *atto-chirp* [6]. An exemplary attosecond pulse spectrum calculated from a hydrogenic atom with an ionization potential of 15.8 eV (with a nuclear charge of 1.078) driven by a single-cycle 1.8 µm driving field of peak intensity 1×10^{14} W/cm^2 is shown in Fig. 1.2 (a) by the solid blue line. The spectrum exhibits a plateau structure characteristic of recollision processes until a cutoff energy near 100 eV. The group delay (i.e. the frequency derivative of the spectral phase) is shown in Fig. 1.2 (b) by the blue line and exhibits a linear slope associated with the *atto-chirp*.

In more complex systems, however, the shape of the ionic potential, the bound electron wavefunction, or interactions of the recollision electron with the system's other electrons can result in complex phase structures being imprinted onto the emitted radiation through the transition moment coupling bound and continuum states [7, 8, 9]. An example of this is the Cooper minimum in argon, a spectral minimum in high harmonic spectra which results from the nodal structure of the $3p$ orbital radial wavefunction. This minimum occurs due to a sign-change in the $3p$ radial orbital, equivalent to a π phase-shift, being imprinted onto the transition moment. The effect of this on attosecond pulse generation is depicted in Fig. 1.2. The attosecond pulse intensity spectrum from a model argon atom in (a) (red) exhibits a spectral minimum near 50 eV and the group delay in (b) (red) deviates from the expected *atto-chirp* around the spectral minimum due to the transition moment phase shift. The interference of the continuum and structured bound state, as observed through the dipole moment, reveals information about the electronic structure of the ground state wavefunction.

Transition moment phase shifts such as these are ubiquitous in nature and can provide a wealth of information regarding the electronic structure of matter. They may arise from ionic structure (e.g. two-centre interference [10]), electronic structure (e.g. Cooper minima [7]), or multielectron interaction (e.g. the giant dipole resonance in xenon [8]). Within recollision, they have been observed in atomic, molecular, and solid-state systems and are typically measured through the effect of the transition moment on the group delay of attosecond pulses or ionization induced by attosecond pulses. Since recollision appears to be a universal response of matter to strong fields [2, 11, 12], measurements of these phase shifts during recollision will be important in nearly all areas of physical chemistry.

The conventional approach to measuring transition moment phase shifts in attosecond science consists of using an attosecond pulse to photoionize a medium in the presence of a co-phased infrared field. Such measurements have provided tremendous insight into electronic structure and dynamics [13, 14, 7]. However, their implementation can be challenging. The requirement for an attosecond pulse to photoionize a target medium necessitates large pulse energies. Since recollision is an inherently inefficient XUV generation process [15], this requires the use of sophisticated femtosecond laser sources to generate energetic attosecond pulses. Further, it is required that these pulses be well separated from the infrared field which drove their generation and, thus, spectral filters which diminish the useable attosecond pulse energy for measurement are required. This problem will be exacerbated as attosecond science progresses towards studying processes at higher energies [16]. This follows from two separate phenomena: (i) photoionization cross-sections rapidly decrease with photon energy

[17] and (ii) the generation of attosecond pulses at high frequencies requires long wavelength λ_0 driving lasers (since the maximum photon energy $\propto \lambda_0^2$ [2]) and the efficiency of HHG scales as $\lambda_0^{-6.3\pm1.1}$ [18].

An alternative approach to attosecond measurement was proposed and demonstrated in 2006 by Dudovich *et al.* [19]. By perturbing the recollision process with a weak infrared field, a controlled phase shift can be imparted onto the recollision electron. Varying this phase shift results in a modulation of the observed attosecond pulse spectrum and these modulations contain information about the recollision process. This measurement is performed entirely optically, both simplifying and improving the efficiency of attosecond measurement. While this all-optical approach to attosecond measurement is significantly more efficient than photoionization-based measurement, it has not been widely adopted within attosecond science because it is believed that these all-optical measurements are insensitive to transition moment phase shifts. It is believed perturbations of the recollision electron wave packet do not affect recombination dynamics sufficiently to be observable [9]. This is supported by numerical studies comparing photoionization-based and all-optical measurements in a diatomic molecular system, which exhibits a spectral minimum and transition moment phase shift due to two-centre interference [9]. While this study showed that photoionization-based measurement was sensitive to the transition moment phase shift, it was completely absent from the all-optical measurement.

If we consider again how interference manifests in recollision, however, it is not clear why this should be the case. The components of the recollision electron wave packet which dominate dipole emission are those whose phase is complementary to both the strong field driven dynamics in the continuum and the bound-state to which the recollision electron recombines. In simple systems, the transition moment phase is slowly varying and has virtually no effect in determining which components of the recollision electron wave packet constructively interfere when compared with the strong field in the continuum [2]. In systems with a rapidly varying transition moment phase shift, however, the variation of the transition moment phase over a given energy range can be on the same order as that of the phase accrued by the electron in the continuum. In such cases, only the components of the recollision electron wave packet which are appropriately phased with respect to both the strong-field continuum dynamics and the transition moment phase will interfere constructively and contribute to dipole emission. In other words, the transition moment affects which components of the recollision wave packet dominate dipole emission and, thus, its effect should manifest in an all-optical measurement.

In this thesis, I demonstrate that all-optical attosecond measurement is sensitive to the transition moment phase. This sensitivity, however, depends on the nature of the transition moment phase shift and how it affects recollision trajectories. In particular, I demonstrate that all-optical methods are insensitive to transition moment phase shifts arising from ionic structure because these phase shifts arise from a quantum path interference of recollision trajectories which vary slightly from trajectories in a simple atomic system. In contrast, transition moment phase shifts arising from electronic structure and multielectron interac-

tion affect recollision trajectories and can be measured. I do this using analytic models, *ab initio* simulation, and experiment. These results suggest new routes towards attosecond measurement of electron dynamics related to transition moment phase shifts and multielectron interaction using experimental systems available to any laboratory capable of generating high harmonic radiation.

The structure of this thesis is as follows:

— Chapters 2 and 3 introduce concepts of strong field physics and attosecond pulse measurement relevant to this thesis.

— The theory used in describing recollision in multielectron systems and its numerical implementation are described in Chapters 4 and 5.

— The measurement of transition moment phase shifts in single-active electron systems using all-optical techniques is discussed within the SFA in Chapter 6.

— Time-dependent Schrödinger equation simulations of *in situ* measurement in one-dimensional systems with transition moment phase shifts due to ionic structure and multielectron interaction are investigated in Chapter 7.

— Experimental and *ab initio* simulated all-optical measurements of the transition moment phase around the Cooper minimum in argon are presented in Chapter 8.

— The spectral characteristics of attosecond pulses generated in xenon around the giant dipole resonance and their all-optical measurement are investigated in Chapter 9.

— Chapter 10 summarizes the conclusions of this work and discusses the outlook for all-optical measurement within attosecond science.

Hartree atomic units (i.e. $\hbar = m_e = e = 1$) are used throughout, unless otherwise stated.

Chapter 2

Introduction to Strong Field Physics

Outline: In order to describe the all-optical measurement of recollision dynamics, it is first necessary to introduce the formalism of the Lewenstein model of recollision and high harmonic generation (i.e. the strong field approximation).

I first consider a system of electrons described by the state $|\Psi(t)\rangle$ at time t. The dynamics of the system are governed by the time-dependent Schrödinger equation (TDSE):

$$i\frac{\partial}{\partial t}|\Psi(t)\rangle = \hat{\mathbf{H}}(t)|\Psi(t)\rangle\,, \tag{2.1}$$

where $\hat{\mathbf{H}}(t)$ is the Hamiltonian operator which describes the total energy of the state $|\Psi(t)\rangle$. From this, the time evolution of the state between times t_0 and t can be described using a propagator operator, $\hat{\mathbf{U}}(t,t_0)$:

$$|\Psi(t)\rangle = \hat{\mathbf{U}}(t,t_0)|\Psi(t_0)\rangle\,. \tag{2.2}$$

From eq. (2.1), the propagator operator must satisfy the following:

$$\hat{\mathbf{U}}(t_0,t_0) = \hat{\mathbf{I}}, \tag{2.3}$$

$$\hat{\mathbf{U}}(t,t_1)\hat{\mathbf{U}}(t_1,t_0) = \hat{\mathbf{U}}(t,t_0), \tag{2.4}$$

$$i\frac{\partial\hat{\mathbf{U}}(t,t_0)}{\partial t} = \hat{\mathbf{H}}(t)\hat{\mathbf{U}}(t,t_0). \tag{2.5}$$

The formal solution for $\hat{\mathbf{U}}(t,t_0)$ is the exponential of the time-ordered integration of the Hamiltonian between times t_0 and t:

$$\hat{\mathbf{U}}(t,t_0) = \exp\left[-i\int_{t_0}^{t}\hat{\mathbf{H}}(\tau)d\tau\right]. \tag{2.6}$$

In order to describe recollision, it is first necessary to establish the electronic system and introduce necessary approximations. I consider a single-active electron (SAE) in an atom

or molecule interacting with a strong electric field. Within the SAE approximation, it is assumed that only a single electron is influenced by the strong field and all other electrons are frozen. The Hamiltonian describing this system is composed of a static component, $\hat{\mathbf{H}}_0$, which describes the interaction of the electron with the ion and a time-dependent component, $\hat{\mathbf{H}}_{int}(t)$, which describes the interaction of the electronic system with the strong field:

$$\hat{\mathbf{H}}(t) = \hat{\mathbf{H}}_0 + \hat{\mathbf{H}}_{int}(t). \tag{2.7}$$

The static component of the Hamiltonian is defined as follows:

$$\hat{\mathbf{H}}_0 = \frac{\hat{\mathbf{k}}^2}{2} + v_0(\mathbf{r}), \tag{2.8}$$

where $\hat{\mathbf{k}} = -i\nabla_{\mathbf{r}}$ is the momentum operator, $\mathbf{r}$ is the electron position, and $v_0(\mathbf{r})$ is the potential felt by the electron due to the ion. The interaction of the electron with the strong field is described within the length gauge and dipole approximation, such that

$$\hat{\mathbf{H}}_{int}(\mathbf{r}, t) = -\hat{\mathbf{d}} \cdot \mathbf{F}(t), \tag{2.9}$$

where $\hat{\mathbf{d}} = -\hat{\mathbf{r}}$ is the dipole operator and $\mathbf{F}(t)$ is the electric field at time t.

I assume that the electron is initially in its ground state $|\psi_0\rangle$ with energy E_0 at time t_0. The temporal evolution of the system between times t_0 and t_r can be partitioned into times before and after the strong field *turns on* at time t_b. As will be demonstrated below, the times t_b and t_r correspond to the times of ionization and recombination for recollision trajectories. Between times t_0 and t_b, the propagator is found from the static Hamiltonian, $\hat{\mathbf{H}}_0$:

$$\hat{\mathbf{U}}_0(t_b, t_0) = \exp\left[-i \int_{t_0}^{t_b} \hat{\mathbf{H}}_0 \, d\tau\right]. \tag{2.10}$$

Between times t_b and t_r, the strong field is present and the propagator $\hat{\mathbf{U}}(t_r, t_b)$ is determined by the full Hamiltonian in eq. (2.7):

$$\hat{\mathbf{U}}(t_r, t_b) = \exp\left[-i \int_{t_b}^{t_r} \left(\hat{\mathbf{H}}_0 + \hat{\mathbf{H}}_{int}(\mathbf{r}, \tau)\right) d\tau\right]. \tag{2.11}$$

With these definitions, the formal solution for the time-dependent wavefunction at time t_r after evolving from time t_0 is given as follows [20]:

$$|\Psi(t_r)\rangle = -i \int_{t_0}^{t_r} dt_b \hat{\mathbf{U}}(t_r, t_b) \hat{\mathbf{H}}_{int}(\mathbf{r}, t_b) \hat{\mathbf{U}}_0(t_b, t_0) \, |\psi_0\rangle + \hat{\mathbf{U}}_0(t_r, t_0) \, |\psi_0\rangle \,. \tag{2.12}$$

Since $|\psi_0\rangle$ is an eigenstate of $\hat{\mathbf{H}}_0$,

$$\hat{\mathbf{U}}_0(t, t_0) \, |\psi_0\rangle = e^{-iE_0(t-t_0)} \, |\psi_0\rangle \,, \tag{2.13}$$

and eq. (2.12) can be simplified as

$$|\Psi(t_r)\rangle = -i\int_{t_0}^{t_r} dt_b \hat{\mathbf{U}}(t_r,t_b)\hat{\mathbf{H}}_{int}(\mathbf{r},t_b)e^{-iE_0(t_b-t_0)}\,|\psi_0\rangle + e^{-iE_0(t_r-t_0)}\,|\psi_0\rangle\,. \tag{2.14}$$

Despite working with a single electron, solving eq. (2.14) with the full propagator is still a formidable task. It is here where the principal approximation of the SFA is introduced. In the continuum, the influence of the strong field on the recollision electron is much greater than that of the ionic potential. Accordingly, the influence of the ionic potential on the continuum electron is neglected and only the influence of the strong field on the continuum electron is included. This amounts to replacing the full Hamiltonian between times t_b and t_r with $\hat{\mathbf{H}}_V(t)$, known as the Volkov Hamiltonian, which describes a free electron interacting with an external field:

$$\hat{\mathbf{H}}_V(t) = \frac{(\hat{\mathbf{k}} + \mathbf{A}(t))^2}{2}, \tag{2.15}$$

where $\mathbf{A}(t)$ is the vector potential associated with the electric field $\mathbf{F}(t)$. Within this approximation, the continuum electron wavefunction at time t_b is treated as a plane wave with momentum $\mathbf{k}+\mathbf{A}(t_b)$. The propagator associated with $\hat{\mathbf{H}}_V(t)$ is called the Volkov propagator, can be found analytically, and is defined through the following:

$$\hat{\mathbf{U}}_V(t_r,t_b)\,|\mathbf{k}+\mathbf{A}(t_b)\rangle = e^{-iS(\mathbf{k},t_b,t_r)}\,|\mathbf{k}+\mathbf{A}(t_r)\rangle\,, \tag{2.16}$$

$$\langle\mathbf{r}|\mathbf{k}+\mathbf{A}(t)\rangle = \frac{1}{(2\pi)^{3/2}}e^{i(\mathbf{k}+\mathbf{A}(t))\cdot\mathbf{r}}, \tag{2.17}$$

$$S(\mathbf{k},t_b,t_r) = \frac{1}{2}\int_{t_b}^{t_r}\left[\mathbf{k}+\mathbf{A}(\tau)\right]^2 d\tau. \tag{2.18}$$

Since the set of plane waves forms a complete basis, i.e.

$$\hat{\mathbf{I}} = \int d\mathbf{k}\,|\mathbf{k}+\mathbf{A}(t)\rangle\,\langle\mathbf{k}+\mathbf{A}(t)|\,, \tag{2.19}$$

the problem can be simplified by inserting eq. (2.19) into eq. (2.14) and replacing $\hat{\mathbf{U}}(t_r,t_b)$ with $\hat{\mathbf{U}}_V(t_r,t_b)$:

$$\begin{aligned}|\Psi(t_r)\rangle = -i\int d\mathbf{k}\int_{t_0}^{t_r} dt_b e^{-iS(\mathbf{k},t_b,t_r)}\,|\mathbf{k}+\mathbf{A}(t_r)\rangle\,\langle\mathbf{k}+\mathbf{A}(t_b)|\,\hat{\mathbf{r}}\cdot\mathbf{F}(t_b)\,|\psi_0\rangle\,e^{-iE_0(t_b-t_0)} \\ + e^{-iE_0(t-t_0)}(t,t_0)\,|\psi_0\rangle\,.\end{aligned} \tag{2.20}$$

With this, the wavefunction $|\Psi(t_r)\rangle$ can be partitioned into its bound and free components, $|\Psi_0(t_r)\rangle$ and $|\Psi_c(t_r)\rangle$, respectively:

$$|\Psi(t_r)\rangle = |\Psi_c(t_r)\rangle + |\Psi_0(t_r)\rangle\,, \tag{2.21}$$

$$|\Psi_0(t_r)\rangle = e^{-iE_0(t_r-t_0)}\,|\psi_0\rangle\,, \tag{2.22}$$

$$|\Psi_c(t_r)\rangle = -i\int d\mathbf{k}\int_{t_0}^{t_r} dt_b e^{-iS(\mathbf{k},t_b,t_r)}\,|\mathbf{k}+\mathbf{A}(t_r)\rangle\,\langle\mathbf{k}+\mathbf{A}(t_b)|\,\hat{\mathbf{r}}\cdot\mathbf{F}(t_b)\,|\psi_0\rangle\,e^{-iE_0(t_b-t_0)}. \tag{2.23}$$

The time-dependent dipole moment, $\hat{\mathbf{D}}(t_r)$, is then found as follows:

$$\begin{aligned}\mathbf{D}(t_r) &= \langle\Psi(t_r)|\hat{\mathbf{d}}|\Psi(t_r)\rangle \\ &= \langle\Psi_c(t_r)|\hat{\mathbf{d}}|\Psi_c(t_r)\rangle + \langle\Psi_0(t_r)|\hat{\mathbf{d}}|\Psi_c(t_r)\rangle + \langle\Psi_c(t_r)|\hat{\mathbf{d}}|\Psi_0(t_r)\rangle + \langle\Psi_0(t_r)|\hat{\mathbf{d}}|\Psi_0(t_r)\rangle.\end{aligned} \tag{2.24}$$

It is assumed that continuum-continuum transition are negligible and that the ground state has no permanent dipole:

$$\langle\Psi_0(t_r)|\hat{\mathbf{d}}|\Psi_0(t_r)\rangle = \langle\Psi_c(t_r)|\hat{\mathbf{d}}|\Psi_c(t_r)\rangle = 0. \tag{2.25}$$

With this, replacing the ground state energy E_0 with the ionization potential $I_p = -E_0$, and introducing the transition moment $\mathbf{d}(\mathbf{k}) = \langle\mathbf{k}|\hat{\mathbf{r}}|\psi_0\rangle$ at momentum $\mathbf{k}$, the final expression for the dipole moment is obtained:

$$\mathbf{D}(t_r) = -i\int d\mathbf{k}\int_{t_0}^{t_r} dt_b \mathbf{d}^*\left(\mathbf{k}+\mathbf{A}(t_r)\right) e^{-i[S(\mathbf{k},t_b,t_r)+I_p(t_r-t_b)]}\mathbf{F}(t_b)\cdot\mathbf{d}\left(\mathbf{k}+\mathbf{A}(t_b)\right) + c.c. \tag{2.26}$$

Finally, the dipole spectrum $\tilde{D}(\Omega)$ at frequency Ω can be found from the Fourier transform of eq. (2.26):

$$\tilde{\mathbf{D}}(\Omega) = -i\int_{-\infty}^{\infty} dt_r \int d\mathbf{k}\int_{t_0}^{t_r} dt_b \mathbf{d}^*\left(\mathbf{k}+\mathbf{A}(t_r)\right) e^{-i[S(\mathbf{k},t_b,t_r)+I_p(t_r-t_b)]}\mathbf{F}(t_b)\cdot\mathbf{d}\left(\mathbf{k}+\mathbf{A}(t_b)\right) e^{i\Omega t_r}, \tag{2.27}$$

where the complex conjugate has been omitted for brevity.

2.1 The Strong Field Approximation Dipole Moment and Saddle-Point Integration

The integrals in eqs. (2.26) and (2.27) can be calculated numerically relatively easily, but an alternative approach based on saddle-point integration [21] allows for faster calculation of

the dipole moment and provides a link to the classical recollision model [1]. The saddle-point method is based on the approximation that, for integrands with a rapidly varying phase, the components of the integrand which dominate the integral are those for which the integrand phase is stationary. The integral is then approximated as a Gaussian integral around these points.

As an example, I consider a function $f(x) = f_0(x)e^{i\Phi(x)}$, where $f_0(x)$ and the phase $\Phi(x)$ are slowly and rapidly varying, respectively. The point x_s where $\Phi'(x_s) = 0$ is referred to as a saddle-point solution. Around this point,

$$\Phi(x) \approx \Phi(x_s) + \frac{1}{2}\Phi''(x_s)(x - x_s)^2. \tag{2.28}$$

For $a < x_s < b$, I then have the following:

$$\begin{aligned}\int_a^b f(x)dx &= \int_a^b f_0(x)e^{i\Phi(x)}dx \\ &\approx f_0(x_s)e^{i\Phi(x_s)}\int_a^b e^{i\Phi''(x_s)(x-x_s)^2/2}dx \\ &= \sqrt{\frac{2\pi i}{\Phi''(x_s)}}f_0(x_s)e^{i\Phi(x_s)}.\end{aligned} \tag{2.29}$$

For the case where there are multiple saddle-point solutions, the integral is approximated as a discrete sum of contributions in the form of eq. (2.29):

$$\int_a^b f(x)dx \approx \sum_{x_s}\sqrt{\frac{2\pi i}{\Phi''(x_s)}}f_0(x_s)e^{i\Phi(x_s)}. \tag{2.30}$$

2.1.1 The Strong Field Approximation Dipole Moment in the Frequency Domain

Going back to the recollision dipole moment, I first consider the application of the saddle-point method to the dipole spectrum in eq. (2.27) and assume the transition moment $\mathbf{d}(\mathbf{k})$ is slowly varying. Further, I assume the strong field is polarized along $\hat{\mathbf{z}}$ and omit vector notation, as all vector quantities will be parallel to $\hat{\mathbf{z}}$. The integrand phase $\Phi_{tot}(k, t_b, t_r)$ is given as follows:

$$\Phi_{tot}(k, t_b, t_r) = \Omega t_r - I_p(t_r - t_b) - S\left(k, t_b, t_r\right). \tag{2.31}$$

The saddle-points for this integral can be found by setting the derivatives of the total phase with respect to k, t_b, and t_r to zero, which yields the following set of equations:

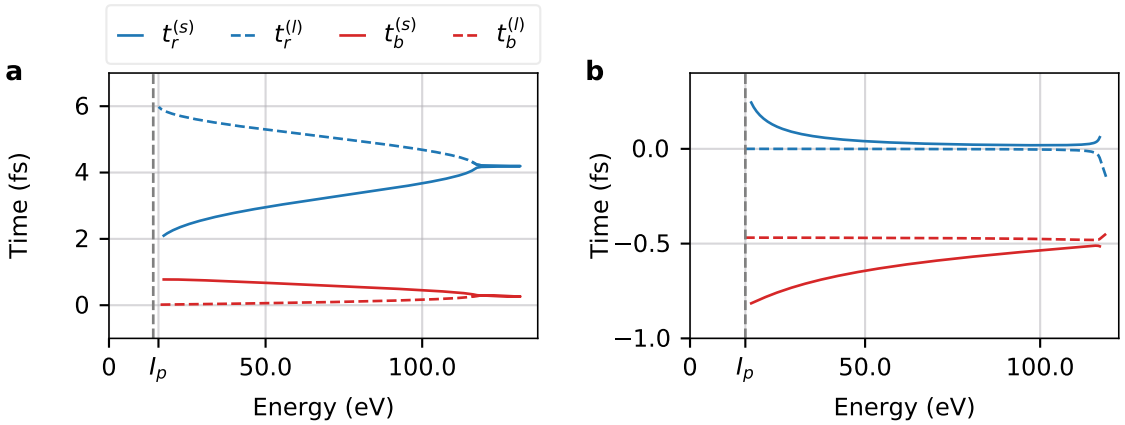

Figure 2.1 – The solutions to eqs. (2.32 - 2.34) for the real (a) and imaginary (b) components of the times of ionization (red) and recombination (blue), t_b and t_r, respectively, plotted against the emitted photon energy calculated with a sinusoidal driving field of wavelength 1.8 µm and peak intensity of 1×10^{14} W/cm^2. The short (long) trajectory solutions are depicted by solid (dashed) lines, with their labels (s and l, respectively) in the legend appearing as superscripts. The dashed vertical grey line denotes the ionization potential of the atom at 15.8 eV (i.e. the minimum emitted photon energy).

$$\frac{\partial \Phi_{tot}}{\partial k} = 0 = \int_{t_b}^{t_r} [k + A(\tau)]\, d\tau \tag{2.32}$$

$$\frac{\partial \Phi_{tot}}{\partial t_b} = 0 = \frac{[k + A(t_b)]^2}{2} + I_p, \tag{2.33}$$

$$\frac{\partial \Phi_{tot}}{\partial t_r} = 0 = \frac{[k + A(t_r)]^2}{2} + I_p - \Omega. \tag{2.34}$$

These equations are numerically solved for the saddle-point solutions k, t_b, and t_r, which provide a clear link between the quantum mechanical and classical recollision models [1]:

— Eq. (2.32) has the form of a displacement condition and reflects the requirement that an electron ionizing at time t_b must return to its original position at time t_r in order to coherently emit a photon.

— Eq. (2.33) describes the tunnelling step at time t_b and imposes the requirement for energy conservation during tunnelling. Since $I_p > 0$, this equation must be solved using complex time.

— Finally, eq. (2.34) describes the recombination step at time t_r and imposes the requirement for energy conservation as the electron recombines into its initial state and emits a photon of frequency Ω.

Figs. 2.1 (a) and (b) depict the real and imaginary saddle-point solutions, respectively, for the times of ionization (red) and recombination (blue) as a function of emitted photon

energy calculated within a single half-cycle of a cosine driving electric field of wavelength 1.8 µm and peak intensity of 1×10^{14} W/cm^2. The ionization potential of the atom is denoted by a dashed vertical grey line. I first discuss the real saddle-point solutions. In the low energy region (i.e. below 116 eV), there are two distinct times of ionization and recombination for each emitted photon energy. These solutions are distinguished according to the time the electron spends in the continuum and are labelled as short (solid) and long (dashed) trajectories. Within this region, the attosecond pulse spectral intensity is relatively flat, as demonstrated in Fig. 1.2. Accordingly, this spectral region is referred to as the *plateau*. Above 116 eV, the short and long trajectories coalesce and their distinction becomes ambiguous. The attosecond pulse spectral intensity decays exponentially in this region, referred to as the *cutoff*.

The imaginary times of ionization are related to the amplitude of the continuum electron wave packet [2]. The long trajectory ionization times occur near the peak of the electric field half-cycle (i.e. near $t = 0$), where the field is strongest, and the range of ionization times is narrow. Accordingly, the long trajectory imaginary ionization time is relatively constant throughout the spectrum. In contrast, the short trajectories ionize at later times when the field is weaker. Consequently, the imaginary times of ionization are larger for short trajectories, particularly at low energies near I_p.

The real recombination times for both the long and short trajectories within the plateau exhibit an approximately linear dependence on the emitted photon energy, but with opposite slopes. Due to the comparatively narrow window of ionization times, the variation of the recombination time with energy is the predominant factor in determining the group delay of the emitted attosecond pulse. The near linear dependence of the recombination time on energy gives rise to the quadratic phase described in Chapter 1 known as the *atto-chirp*. Above the cutoff, the imaginary recombination time for both the long and short trajectories diverge. However, only the long trajectory solutions remain physical, as the short trajectory imaginary recombination time diverges towards positive infinity.

Since the imaginary times of ionization for long trajectories is smaller than those for short trajectories, it is evident that the continuum electron wave packet is dominated by long trajectory components. Despite this, experimentally observed attosecond pulse spectra are typically dominated by short trajectory emission. This is due to phase matching conditions, which favour short trajectory emission [22]. This is particularly true for long wavelength driving lasers. Consequently, I focus on short trajectory throughout this thesis.

Since eq. 2.32 is linear with the canonical momentum k, k can be uniquely solved for in terms of t_b and t_r:

$$k = -\left(t_r - t_b\right)^{-1} \int_{t_b}^{t_r} A(\tau) d\tau. \tag{2.35}$$

With this, the integral over k can be approximated using the saddle-point method. Since the integral over momentum is three-dimensional, the prefactor in the saddle-point integration

is found through the Hessian matrix:

$$\det\left[S''_{k,k}\right] = (t_r - t_b)\,. \tag{2.36}$$

The dipole spectrum in eq. (2.27) then takes the following form:

$$\begin{aligned}\tilde{\mathbf{D}}(\Omega) = \sum_{j=1}^{N_{sp}} \sqrt{\frac{2\pi i}{S''_{t_r,t_r}} \cdot \frac{2\pi i}{S''_{t_b,t_b}}} \left(\frac{2\pi i}{t_r^{(j)} - t_b^{(j)} + i\epsilon}\right)^{3/2} d^*(k^{(j)} + A(t_r^{(j)}))e^{-i[S(k^{(j)},t_b^{(j)},t_r^{(j)}) + I_p(t_r^{(j)} - t_b^{(j)})]} \\ \times F(t_b^{(j)})d(k^{(j)} + A(t_b^{(j)}))e^{i\Omega t_r^{(j)}},\end{aligned} \tag{2.37}$$

where the summation runs over all N_{sp} sets of saddle-point solutions $k^{(j)}, t_b^{(j)}, t_r^{(j)}$ which lead to photon emission at frequency Ω. The term ϵ is introduced into the prefactor from the momentum integration in order to regularize the integral when $t_r - t_b$ is small, for which the saddle-point approximation is not applicable.

Eq. (2.37) can be factorized into the product of three terms, each representing a step of the three-step recollision model:

$$\tilde{D}(\Omega) = \sum_{j=1}^{N_{sp}} a_{rec}(k^{(j)}, t_r^{(j)}) a_{prop}(k^{(j)}, t_b^{(j)}, t_r^{(j)}) a_{ion}(k^{(j)}, t_b^{(j)}), \tag{2.38}$$

where

$$a_{ion}(k, t_b) = \sqrt{\frac{2\pi}{iS''_{t_b,t_b}}} e^{-iS(k,t'_b,t_b)} d(k + A(t_b)), \tag{2.39}$$

$$a_{pro}(k, t_b, t_r) = \left(\frac{2\pi}{t_r - t_b + i\epsilon}\right)^{3/2} e^{-iS(k,t_b,t_r)}, \tag{2.40}$$

$$a_{rec}(k, t_r) = \sqrt{\frac{2\pi}{iS''_{t_r,t_r}}} e^{-iS(k,t_r,t'_r)} d^*(k + A(t_r)). \tag{2.41}$$

Above, the primed times t' denote the imaginary component of the time t (i.e. $t' = i\ \mathrm{Im}[t]$).

2.1.2 The Strong Field Approximation Dipole Moment in the Time Domain

Alternatively, the dipole moment can be calculated in the time domain using eq. (2.26). For this case, the integrand phase is given as follows:

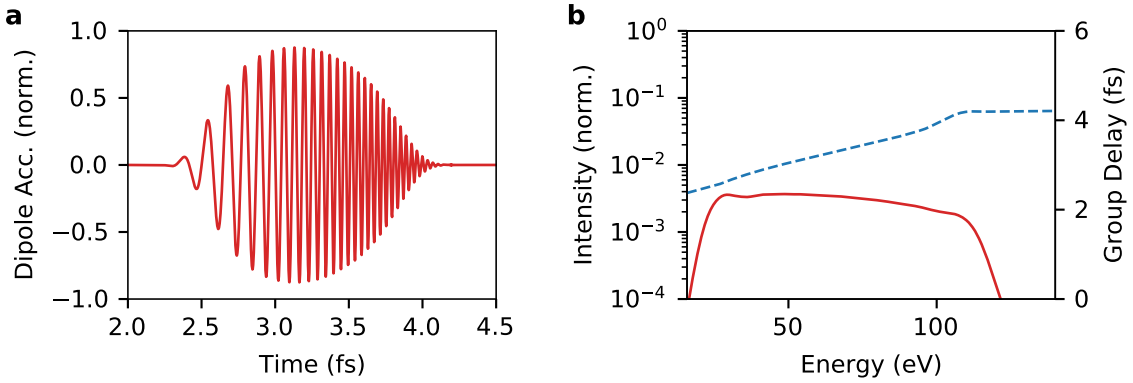

Figure 2.2 – The solutions to eqs. (2.32-2.34) f or the real (a) and imaginary (b) components of ϕ_b and ϕ_r plotted against the emitted photon energy in units of the ponderomotive energy of the recollision electron. A sine-squared window is imposed onto the time-domain dipole acceleration.

$$\Phi_{tot}(k, t_b, t_r) = -I_p(t_r - t_b) - S(k, t_b, t_r). \tag{2.42}$$

Applying the saddle-point approximation yields the following two saddle-point equations for k and t_b:

$$\frac{\partial S}{\partial k} = 0 = \int_{t_b}^{t_r} [k + A(\tau)]\, d\tau, \tag{2.43}$$

$$\frac{\partial S}{\partial t_b} = 0 = \frac{[k + A(t_b)]^2}{2} + I_p. \tag{2.44}$$

These two equations can be solved with the recombination time t_r acting as a parameter. With this, the time domain dipole moment at time t_r is then given as follows:

$$D(t_r) = i\sqrt{\frac{2\pi}{iS''_{t_b,t_b}}}\left(\frac{2\pi}{\det\left[iS''_{k,k}\right]}\right)^{3/2} d^*(k + A(t_r))e^{-i[S(k,t_b,t_r)+I_p(t_r-t_b)]}F(t_b)d(k + A(t_b)), \tag{2.45}$$

The dipole spectrum is then found by evaluating the Fourier transform of eq. (2.45).

The dipole acceleration and attosecond pulse spectrum calculated using the time-domain dipole moment including only short trajectories from the SFA with a sinusoidal driving field of wavelength 1.8 µm and peak intensity of 1×10^{14} W/cm^2 are shown in Figs. 2.2 (a) and (b), respectively. A sine-squared window is used on the dipole acceleration and the linear *atto-chirp* is clearly visible within the temporal plot of the dipole acceleration. The spectral

intensity (red, left axis) in (b) exhibits the plateau structure characteristic of recollision until the cutoff above 100 eV. The group delay (dashed blue, right axis), calculated from the frequency derivative of the spectral phase, closely resembles the recombination times shown in Fig. 2.1 (a).

Some subtle features of the SFA model are omitted here for the sake of brevity. Namely, eq. (2.45) describes only a single trajectory recombining at time t_r. This is valid for recollision within a single half-cycle of the driving field, but multiple returns of a continuum electron ejected during other half-cycles can also be included [2]. Also, special treatment of the cutoff when using saddle-point integration is required. This is because the variation of the integrand phase is no longer well approximated by a second-order expansion, as in eq. (2.28) [23]. These features, while important, are not relevant to this thesis.

2.2 The Transition Moment Phase

The original description of the SFA assumes that the phase of the transition moment is slowly varying and, thus, can be neglected in the saddle-point analysis. This is a good approximation for many systems. In some systems, however, the variation of the transition moment phase can be on the same order as the semi-classical action $S(k, t_b, t_r)$ [7, 8]. This phase is imprinted onto the emitted attosecond pulse and measuring these phase shits reveals information about the structure and dynamics which underlie recollision processes. Several strategies have been employed in describing attosecond pulses generated in systems with a rapidly varying transition moment phase. The most robust method is to solve the TDSE numerically, as done in Fig. 1.2, but this approach is both computationally demanding and does not provide the understanding analytical models such as the SFA do. Another approach is to incorporate the transition moment phase shift into the saddle-point analysis within the SFA. This can be done for transition moment phase shifts which vary quickly but sufficiently slowly such that the saddle-point approximation remains valid. This approach is used in Chapter 6 to investigate all-optical measurements of the transition moment phase using the SFA.

The last approach discussed here, known as quantitative rescattering theory (QRS) [24], is based on the factorization of the frequency-domain dipole moment in eq. (2.38). QRS simplifies the calculation of recollision processes in complex systems and accounts for the transition moment phase in a simple way. The principal approximation in QRS is to assume that, since the emitted photon energy is directly related to the electron momentum at the time of recollision, the recombination transition element can be expressed solely through the energy of the emitted radiation:

$$a_{rec}(k + A(t_r)) = a_{rec}(\Omega). \tag{2.46}$$

It is also assumed that $a_{rec}(\Omega)$ is independent of the external laser field [24]. With this, the recombination term in the factorized dipole can be taken outside the summation, as it no

longer depends on the saddle-point solutions:

$$\begin{aligned}\tilde{D}(\Omega) &= a_{rec}(\Omega)\sum_{j=1}^{N_{sp}} a_{pro}(k^{(j)}, t_b^{(j)}, t_r^{(j)}) a_{ion}(k^{(j)}, t_b^{(j)}, t_r^{(j)}) \\ &= a_{rec}(\Omega) W(\Omega),\end{aligned} \tag{2.47}$$

where the product within the summation over the saddle-point solutions is interpreted as describing the continuum electron wave packet at energy Ω, $W(\Omega)$.

The utility of this becomes apparent if one assumes that the continuum electron wave packet is largely independent of the ion. With this assumption, the recollision dipole spectrum can be calculated in a simple system (e.g. hydrogenic atom) and scaled with the transition moment of a more complex system. If we let the super-scripts (0) and (T) denote quantities calculated from a simple and desired target system, respectively, the dipole spectrum from the target system can be approximated as

$$\begin{aligned}\tilde{D}^{(T)}(\Omega) &= \frac{a_{rec}^{(T)}(\Omega)}{a_{rec}^{(0)}(\Omega)} \tilde{D}^{(0)}(\Omega) \\ &= a_{rec}^{(T)}(\Omega) W^{(0)}(\Omega).\end{aligned} \tag{2.48}$$

That is, the recollision electron wave packet calculated from a simple system is simply scaled by the transition moment of a more complex system. With this, the transition moment in complex systems can be extracted from experimentally measured attosecond pulse spectra by scaling the measured spectra with calculated quantities from simple systems.

QRS has been tested numerically in many systems and is widely used to simplify calculation. In particular, its use for describing HHG in argon has been used to demonstrate its validity [24]. It is important, however, to recognize its limitations [25]:

- More than two trajectories can recombine and emit a photon of a given energy in orthogonally-polarized two-colour fields [26]. The recombination dipole in such cases is not simply a function of energy, as expressed in eq. (2.46), but of momentum as well.
- In systems where the transition moment exhibits a spectral minimum or a sufficiently rapidly varying phase shift, the saddle-point approximation used in the derivation of eq. (2.46) is no longer applicable [7, 27].
- In some systems, the interactions between the recollision electron and ion cannot be neglected and dynamic multielectron interaction must be accounted for [28].

The most important implications of QRS for this work are the assumptions that the recolli-

sion electron wave packet is independent of its source and that the recombination transition element is independent of the laser field. All-optical attosecond measurement, discussed in Chapter 3, is based on perturbing the recollision electron wave packet with a weak infrared field. If the electron wave packet is independent of the ion and the transition moment is independent of the laser, all-optical measurements should be insensitive to features of the transition moment.

Summary: With the formalism of the SFA established, the methods used to measure recollision dynamics are described using the SFA in the next chapter.

Chapter 3

Measuring Recollision Dynamics

Outline: Various methods of attosecond measurement are described. The most commonly used methods, those based on photoionization using attosecond pulses (referred to as *ex situ* measurement), are described first. All-optical techniques (referred to as *in situ* measurement) are then described and compared with *ex situ* measurement. Each variation of *in situ* measurement used in this thesis is labelled with a link to the corresponding chapter where it is used.

I contributed to the theoretical development of the single-image *in situ* measurement described in §3.2.3 [29].

Due to their high frequency content, the measurement of attosecond pulses cannot be accomplished with the same methods used to characterize infrared femtosecond pulses [30]. Two broad classes of measurement techniques have been developed [31]. The first class of measurement is based on photoionization of an atom by an attosecond pulse in the presence of a co-phased infrared field and is performed after the attosecond pulse is generated. Accordingly, this class of measurement is known as *ex situ* measurement. The second class of measurement perturbs the recollision process with a weak infrared field and is performed by recording the effect of the perturbing field on the observed attosecond pulse spectrum. Since this measurement is performed during the recollision process itself, this class of measurement is known as *in situ* measurement.

Ex situ and *in situ* measurement are closely related. Both use a weak infrared pulse as a probing mechanism. The critical difference between the two classes is the point at which the measurement is performed. Since *ex situ* measurements characterize the attosecond pulse directly, it is well-accepted that these methods fully characterize an attosecond pulse assuming the transition moment of the ionized atom is well understood. In contrast, *in situ* methods are performed on the recollision wave packet and are, thus, not a measurement of the emitted attosecond pulse. Consequently, the utility of *in situ* measurement to measure attosecond dynamics associated with the parent ion has been the subject of intense debate within the attosecond science community [9]. In particular, it has been questioned whether

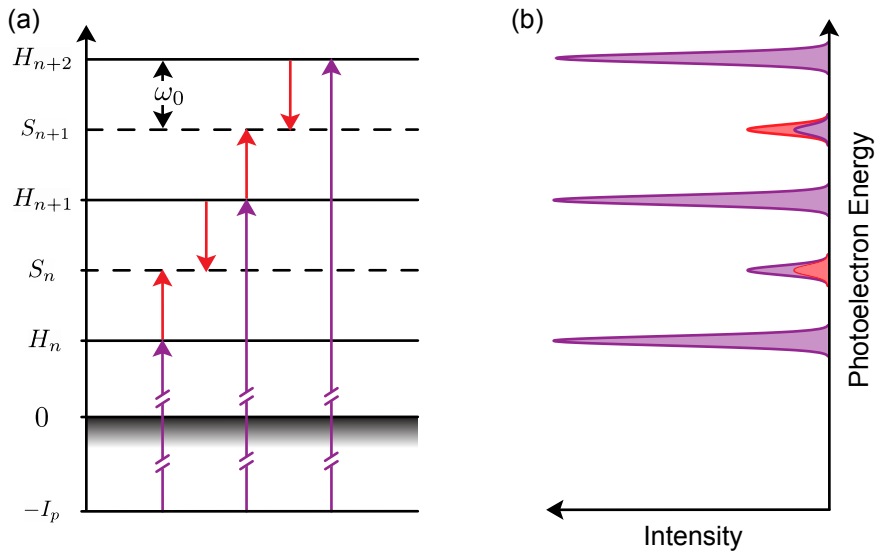

Figure 3.1 – The diagram for the first attosecond pulse train measurement technique, RABBIT. An XUV photon can excite an electron from the ground state of energy $-I_p$ to the continuum (purple arrows). When ionized by an attosecond pulse train, the photoelectron wave packet is a replica of the pulse train and exhibits harmonic peaks at energies $H_n = (2n+1)\omega_0 - I_p$ (integer n). In the presence of an infrared field, the electron can absorb or emit one infrared photon, producing sidebands energies S_n (red arrows). The superposition of the absorption and emission pathways to the sidebands imprints the difference in spectral phase between the harmonic peaks surrounding the sideband. The variation of these sidebands with the delay between the APT and infrared field is used to reconstruct the attosecond pulse train group delay.

in situ measurement is sensitive to the transition moment phase imprinted onto the emitted radiation during recombination.

This chapter consists of an introduction to both *ex situ* and *in situ* attosecond measurement and includes detailed descriptions of the forms of *in situ* measurement used herein. The descriptions of *in situ* measurement are presented as originally published and without reference to transition moment phase shifts. The discussion of *in situ* measurement and the transition moment phase will begin in Chapter 6.

3.1 *Ex Situ* Measurement

3.1.1 Reconstruction of Attosecond Beating by Interference of Two-photon Transition

The measurement of attosecond pulses was first demonstrated experimentally by P.M. Paul *et al.* [32] and was based on a theoretical model of photoionization developed by V.

Véniard *et al.* [33]. The experiment used a technique now known as Reconstruction of Attosecond Beating by Interference of Two-Photon Transitions (RABBIT). This technique, based on photoionization, is capable of measuring the spectral phase (up to a constant) and amplitude of attosecond pulse trains.

Fig. 3.1 (a) depicts the RABBIT measurement scheme. An attosecond pulse train (APT) generated by an infrared field of frequency ω_0 containing harmonic peaks of $(2n+1)\omega_0$ (integer n) and a co-phased infrared field of frequency ω_0 are used to photoionize a target atom of ionization potential I_p. In the absence of the co-phased infrared field, the APT removes an electron from the ground state $|g\rangle$ and produces a photoelectron replica of the APT with harmonic peaks at energies $H_n = (2n+1)\omega_0 - I_p$. This is depicted by the purple arrows coupling the ground state and the energies H_n in Fig. 3.1 (a). With the infrared field, two-photon processes involving ionization by an XUV photon and the emission or absorption of infrared photons can occur, shifting the photoelectron energy by $\pm\omega_0$. This results in the observation of peaks in the photoelectron spectrum at energies $S_n = 2n\omega_0 - I_p$, known as side-bands, between the peaks H_n and H_{n+1}, as is depicted by the red arrows in Fig. 3.1 (a).

Fig. 3.1 (b) depicts an exemplary photoelectron spectrum, with strong signal at energies H_n, H_{n+1}, and H_{n+2} corresponding to the odd harmonics from the attosecond pulse train and sidebands at energies S_n and S_{n+1} shown in purple. The strength of the sideband signal at energy S_n depends on three parameters: the XUV and infrared pulse delay τ, the spectral phase of the harmonics corresponding to H_n and H_{n+1}, Φ_n and Φ_{n+1}, respectively, and the difference in the phase of the transition moment of the ionizing medium for sideband n, $\Delta\Phi_{at,n}$:

$$S_n(\tau) \propto \cos\left(2\omega_0\tau + (\Phi_{n+1} - \Phi_n) + \Delta\Phi_{at,n}\right), \tag{3.1}$$

As the delay τ is varied, the sideband intensity will modulate. This is depicted by the red sideband signals in (b), which shows side-band signals for two different infrared-attosecond pulse delays. The phase of the sideband modulation can be found by evaluating the Fourier transform of the measured sideband signal with respect to τ:

$$\mathcal{F}\left[S_n(\tau)\right] \propto e^{-i(\Delta\Phi_{at,n}+\Phi_{n+1}-\Phi_{n-1})}\delta(2\omega_0 - \Omega) + e^{i(\Delta\Phi_{at,n}+\Phi_{n+1}-\Phi_{n-1})}\delta(\Omega - 2\omega_0). \tag{3.2}$$

Assuming that $\Delta\Phi_{at,n}$ is known or negligible, this provides a measurement of the difference in phase between the harmonics H_n and H_{n+1}. This difference is related to the attosecond pulse group delay, $\tau_{gd}(\Omega)$, using a finite difference approximation to the frequency-derivative of the spectral phase:

$$\begin{aligned} \tau_{gd}(\Omega) &= -\frac{\partial\Phi}{\partial\Omega} \\ &\approx \frac{\Phi_{n+1} - \Phi_n}{2\omega_0}. \end{aligned} \tag{3.3}$$

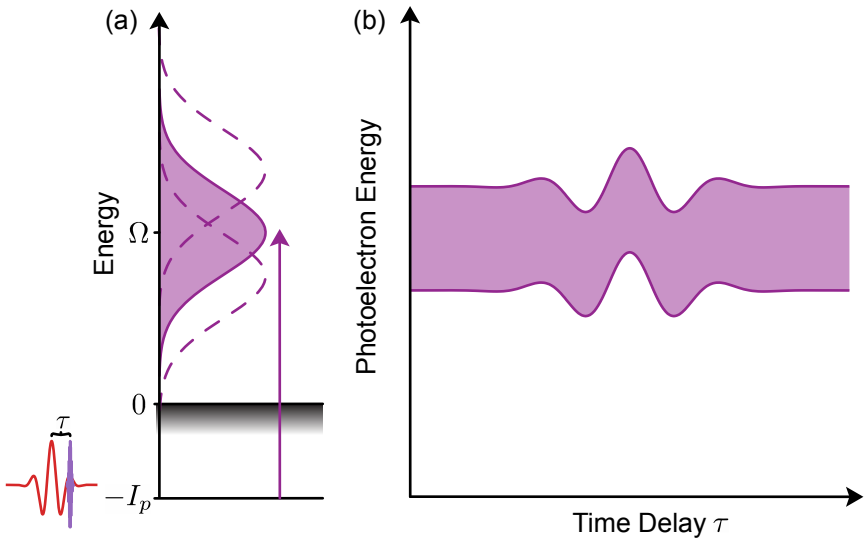

Figure 3.2 – An isolated attosecond pulse of central frequency $\Omega + I_p$ ionizes an atom and creates a photoelectron of energy Ω. In the presence of an infrared field delayed by a time τ (inset on bottom left), the photoelectron energy modulates according to eq. (3.6). This modulation is used to reconstruct the ionizing attosecond pulse using the same formalism as in frequency-resolved optical gating [36].

This provides a measurement of the transition moment phase shift during recombination, which is contained within the phase of the harmonics. Alternatively, measurements of the transition moment phase shift during photoionization can be accomplished by using high harmonics generated in a known system, such that the harmonic phases are known and $\Delta\Phi_{at,n}$ is unknown. In this case, the deviation of the measured phase from the conventional *atto-chirp* in eq. (3.2) can be used to determine $\Delta\Phi_{at,n}$.

In the original implementation of RABBIT, the sideband signal was integrated over its bandwidth in order to obtain a single measurement for each sideband. An extension of this technique known as rainbow RABBIT evaluates the phase for each spectral component within the sideband bandwidth and has been used to characterize Fano resonances in photoionization [34].

3.1.2 Attosecond Streaking

With Dr. TJ Hammond, I used this technique to perform a streaking measurement of attosecond pulses generated using the attosecond lighthouse technique [35].

Attosecond streaking is an extension of the photoionization-based RABBIT technique used to measure isolated attosecond pulses [37, 38]. In a RABBIT measurement, the harmonic structure of the measured attosecond pulse train allows measurements of sideband intensities to occur background-free. The spectrum of an isolated attosecond pulse, how-

ever, is a continuum and a background-free RABBIT measurement cannot be performed due to the absence of harmonic structure. Instead, the shift in momentum imparted by the infrared field onto the photoelectron is used to perform the measurement.

A diagram depicting a streaking measurement is shown in Fig. 3.2. Like RABBIT, attosecond streaking relies on an isolated attosecond pulse photoionizing a target atom in the presence of an infrared field. It is assumed that both the XUV and infrared pulses are of the same polarization, that the ionized electron is promoted directly from the ground state to the continuum, and that the generated photoelectron spectrum is an exact replica of the incident attosecond pulse. The initial momentum, k_i, of the freed electron can be found through energy conservation [30]:

$$k_i = \sqrt{2(\Omega - I_p)}, \tag{3.4}$$

where Ω is the frequency of the attosecond pulse. In the presence of the infrared field, the electron accelerated by the infrared field, resulting in a change in the electron momentum, Δk, which depends on its time of ionization τ:

$$\Delta k = -\int_{\tau}^{\infty} E(t)dt = -A(\tau), \tag{3.5}$$

where $E(t)$ and $A(t)$ are the temporal profiles of the infrared electric field and vector potential at time t and τ is the time of ionization. The resultant change in kinetic energy, $\Delta K(\tau)$, of the photoelectron can then be expressed as

$$\Delta K(\tau) = -A(\tau)\sqrt{2(\Omega - I_p)}, \tag{3.6}$$

This variation is depicted in Fig. 3.2 by the dashed curves on the left. As the attosecond-infrared pulse delay is varied, a spectrogram is obtained, as drawn on the right. From this, the profile of the infrared field can be observed and the measurement of the attosecond pulse group delay can be obtained, as described below.

Within the SFA, the transition amplitude, $a(\mathbf{k})$, of the ionized photoelectron wave packet at time t with canonical momentum $\mathbf{k}$ ionized by an attosecond pulse with electric field $\mathbf{F}_{xuv}(t)$ in the presence of an infrared field with vector potential $\mathbf{A}(t)$ can be described as

$$a(\mathbf{k}, \tau) = -i\int_{-\infty}^{\infty} dt\, \mathbf{F}_{xuv}(t-\tau)\cdot\mathbf{d}(\mathbf{k}+\mathbf{A}(t))G\left(t-\tau\right)e^{i(k^2/2+I_p)t}, \tag{3.7}$$

where

$$G(t) = \exp\left[-\int_{t}^{\infty}\left[\mathbf{k}\cdot\mathbf{A}(\tau) + A^2(\tau)\right]d\tau\right]. \tag{3.8}$$

This equation is the same form as used in frequency-resolved optical gating (FROG) characterization methods [36]. Thus, the attosecond pulse spectral phase can be reconstructed (up to a constant) from the streaking spectrogram using a phase retrieval algorithm.

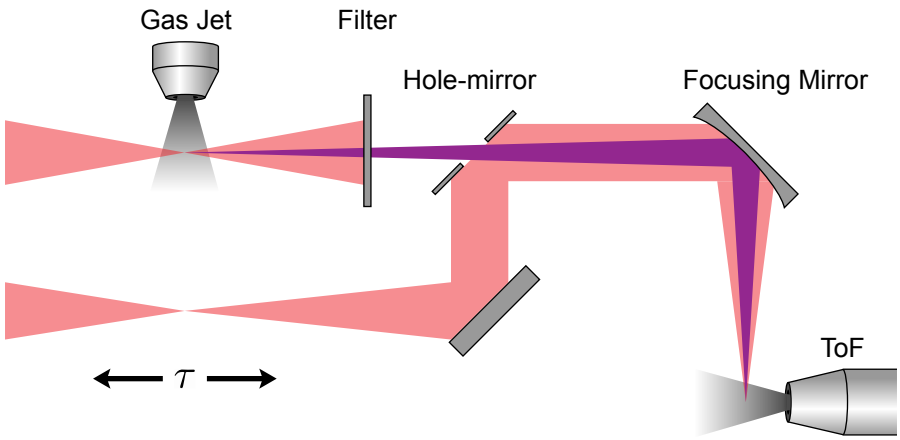

Figure 3.3 – The experimental diagram for attosecond *ex situ* measurements as performed in the JASLAB. An infrared field (red) is focused into a gas jet (diffuse grey), where XUV radiation (purple) is generated. The infrared is filtered out and the XUV is recombined with a weak co-phased infrared field using a hole-mirror. The combined infrared and XUV fields are then focused into a photoelectron spectrometer to perform the *ex situ* measurement. The perturbing infrared field is focused in order to ensure a good overlap with the XUV beam in the photoelectron spectrometer.

3.1.3 Implementation of *Ex Situ* Measurement

Fig. 3.3 depicts a typical experimental setup for an *ex situ* measurement [35]. It consists of a high harmonic/attosecond pulse generation apparatus and a time-of-flight photoelectron spectrometer. The driving infrared field (red) is removed from the attosecond beam (purple) by a spectral filter and passed through a hole-mirror. A co-phased weak infrared field delayed by a time τ is combined with attosecond beam by reflecting off the hole-mirror and the two-colour field is then focused into the photoelectron spectrometer. The perturbing infrared field is focused prior to the focusing into the photoelectron spectrometer in order to ensure sufficient overlap of the XUV and perturbing beams in the photoelectron spectrometer.

Although attosecond *ex situ* measurement has proven to be an incredibly useful tool to measure attosecond electron dynamics and are well accepted within the attosecond science community, they are difficult to implement. In order to efficiently photoionize a target atom, large attosecond pulse energies and, thus, sophisticated high-power femtosecond laser sources are required. Further, they require an experimental apparatus to perform the photoelectron measurement in addition to the system used to generate the attosecond pulses all contained within a large vacuum system. Finally, they require the use of spectral filters to remove the strong infrared driving field from the attosecond beam and an additional means of combining the attosecond and probing infrared beam into a single beam line with a controlled delay. These difficulties limit *ex situ* measurement to well-equipped laboratories and motivated the development of attosecond *in situ* measurement, the subject of the next section.

3.2 *In Situ* Measurement

An alternative form of measurement, known as *in situ* measurement, which circumvents the need for a photoelectron spectrometer, can be accomplished by adding a perturbing field to the recollision process [31]. The perturbing field modulates recollision trajectories and, thus, the observed attosecond pulse spectrum. Like in *ex situ* measurement, the variation of the spectral modulations with respect to the perturbing field is monitored and related to the underlying recollision dynamics.

Several variations of attosecond *in situ* measurement exist which are used to characterize attosecond pulse trains [19, 26] or isolated attosecond pulses [39, 29] using perturbing fields of parallel or perpendicular polarization with respect to the driving field. In essence, all these techniques use the perturbing field to direct XUV radiation onto unused components of the unperturbed attosecond pulse spectrum (either spatially or spectrally). In this thesis, I focus on techniques which use a perturbing field polarized parallel to the driving field.

In situ measurement can be understood by considering the effect of the perturbing field on the recollision process within the SFA. The recollision dipole moment for a simple atom with ground state $|\psi_0\rangle$ and ionization potential I_p is as given in eq. (2.27):

$$\tilde{D}(\Omega) = -i \int dk \int_{-\infty}^{\infty} dt_r \int_{-\infty}^{t_r} dt_b d^*(k + A(t_r)) e^{-iI_p(t_r - t_b) - iS(k,t_b,t_r)} F(t_b) d(k + A(t_b)) e^{i\Omega t_r}, \tag{3.9}$$

where k is the canonical momentum of the electron, t_b is the ionization time, t_r is the recombination time, $A(t)$ is the vector potential of the driving field at time t, $F(t_b)$ is the driving electric field at time t_b, $S(k, t_b, t_r)$ is the semi-classical action, $d(k)$ is the transition moment at momentum k, and vector notation has been omitted because all vector quantities are parallel to $\hat{\mathbf{z}}$.

I now consider recollision driven and perturbed by sinusoidal fields, such that the driving and perturbing vector potentials at time t are given as follows:

$$A(t) = A_0 \sin(\omega_0 t), \tag{3.10}$$

$$A_p(t, \phi) = \eta A_0 \sin\left(n\omega_0 t + \phi\right), \tag{3.11}$$

where A_0 is the driving field vector potential amplitude, ω_0 is the driving field frequency, ϕ is the relative phase between the driving and perturbing fields, $\eta \ll 1$ is the relative amplitude between the perturbing and driving fields, and n is the harmonic-order of the perturbing field. Since $\eta \ll 1$, the semi-classical action including the perturbing field can be expanded to first-order in η, yielding an expression for the perturbation-induced phase shift $\sigma_0(k, t_b, t_r, \phi)$:

$$S(k, t_b, t_r) = \frac{1}{2}\int_{t_b}^{t_r} [k + A(\tau)]^2 \, d\tau + \int_{t_b}^{t_r} (k + A(\tau)) \cdot A_p(\tau, \phi) d\tau + \mathcal{O}\left(\eta^2\right). \tag{3.12}$$

From this, the perturbation-induced phase shift is

$$\sigma_0(k, t_b, t_r, \phi) = \int_{t_b}^{t_r} (k + A(\tau, \phi)) \cdot A_p(\tau) d\tau. \tag{3.13}$$

The phase shift described in eq. 3.13 induces a modulation in the observed high harmonic and attosecond pulse spectra [19, 39]. This modulation is independent of any spectral dispersion occurring after attosecond pulse generation (e.g. dispersive propagation effects) and do not involve a secondary target medium with a possibly unknown transition moment phase. Consequently, attosecond *in situ* measurement focuses exclusively on recollision dynamics and not the spectral characteristics of the emitted attosecond pulse.

While all forms of *in situ* measurement rely on perturbing recollision trajectories in this way, the experimental analysis will depend on the form of *in situ* measurement used. In this thesis, I study collinear and non-collinear forms of measurement for which the perturbing field has either the same frequency or is a second harmonic of the driving field. The details of each method used are discussed below.

3.2.1 Collinear $\omega - 2\omega$ Measurement

Context This technique is used in *ab initio* simulations of an *in situ* measurement of the group delay around the Cooper minimum in argon in Chapter 8.

Attosecond *in situ* measurement was first devised and achieved experimentally by Dudovich *et al.* in 2006 [19]. They perturbed the recollision process with a collinear, co-polarized, and co-phased weak second-harmonic of the driving laser field, performing the *in situ* analogue of a RABBIT measurement [32]. For this measurement, the perturbing field is given as

$$A_p(t, \phi) = \eta A_0 \sin\left(2\omega_0 t + \phi\right), \tag{3.14}$$

and the relative phase ϕ is controlled through a time-delay τ between the driving and perturbing fields. With eqs. (3.13) and (3.14), the perturbation-induced phase shift for a given recollision trajectory has the following form:

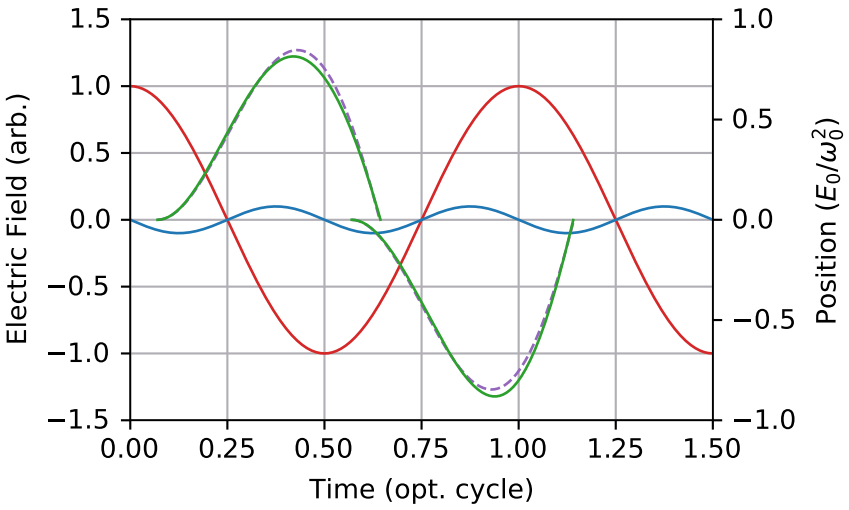

Figure 3.4 – The collinear $\omega - 2\omega$ *in situ* measurement uses a perturbing field to modulate electron trajectories. When driven solely by the strong driving field (solid red), the electron trajectories (dashed purple) in adjacent half-cycles are equal but opposite in sign. Due to the second-harmonic perturbing field (solid blue), the trajectories are modulated such that those in adjacent half-cycles (solid green) are no longer equal but opposite. In the left and right half-cycles, the trajectory is pushed inwards and outwards, respectively. This breaking of half-cycle symmetry results in a $2\sigma(k, t_b, t_r, \phi)$ phase difference between trajectories in adjacent half-cycles and the emission of even-harmonics.

$$\begin{aligned}\sigma(k, t_b, t_r, \phi) &= -\frac{k \sin(\phi) \sin(\omega(t_b - t_r)) \cos(\omega_0(t_b + t_r))}{\omega_0} \\ &\quad - \frac{k \cos(\phi) \sin(\omega_0(t_b + t_r)) \sin(\omega_0(t_b - t_r))}{\omega_0} \\ &= \sigma_c(k, t_b, t_r) \sin(\phi) + \sigma_s(k, t_b, t_r) \cos(\phi) \\ &= \Sigma(k, t_b, t_r) \cos(\phi - \theta(k, t_b, t_r)),\end{aligned} \tag{3.15}$$

where

$$\Sigma(k, t_b, t_r) = \sqrt{\sigma_s^2(k, t_b, t_r) + \sigma_c^2(k, t_b, t_r)}, \tag{3.16}$$

$$\theta(k, t_b, t_r) = \arctan\left(\frac{\sigma_c(k, t_b, t_r)}{\sigma_s(k, t_b, t_r)}\right), \tag{3.17}$$

and $\sigma_c(k, t_b, t_r)$ and $\sigma_s(k, t_b, t_r)$ are found to be the following:

$$\sigma_c(k,t_b,t_r) = A_0\eta\Bigg(\frac{A_0(-3\cos(\omega_0 t_b)+\cos(3\omega_0 t_b)+3\cos(\omega_0 t_r)-\cos(3\omega_0 t_r))}{6\omega_0} + \frac{3k(\sin(2\omega_0 t_r)-\sin(2\omega_0 t_b))}{6\omega_0}\Bigg), \tag{3.18}$$

$$\sigma_s(k,t_b,t_r) = A_0\eta\Bigg(\frac{A_0\left(-3\sin(\omega_0 t_b)+\sin(3\omega_0 t_b)+4\sin^3(\omega_0 t_r)\right)}{6\omega_0} + \frac{3k\cos(2\omega_0 t_b)-3k\cos(2\omega_0 t_r)}{6\omega_0}\Bigg). \tag{3.19}$$

I now consider the perturbed dipole emission from adjacent half-cycles of the driving field, $D_L(t)$ and $D_R(t)$, which are labelled as left L and right R, respectively. The half-cycle symmetry of HHG requires that the unperturbed dipole emission from these half-cycles have a π-phase difference (i.e. $D_L(t) = -D_R(t)$). Since the perturbing field is a second-harmonic of the driving field, however, the perturbation-induced phase shifts for these half cycles are equal but opposite in sign. This asymmetry is depicted in Fig. 3.4, which depicts unperturbed (dashed purple) and perturbed (solid green) recollision trajectories (plotted on right axis) in adjacent cycles of the driving field (red, plotted on left axis). The perturbing field (solid blue) is also plotted on the left. In the left half-cycle the electron trajectory is pushed inwards by the perturbing field, while the trajectory in the right half-cycle is pushed outwards. This results in a phase difference of $2\sigma(k,t_b,t_r,\phi)$ between the emission in these half-cycles, breaking the half-cycle asymmetry which leads to the emission of even-harmonics of the driving field.

This emission of even harmonics due to the breaking of half-cycle asymmetry is demonstrated in Fig. 3.5. Fig. 3.5 (a) shows the high harmonic spectrum generated by an 800 nm flat-top pulse from a one-dimensional TDSE simulation. Fig. 3.5 (b) shows the HHG spectra from the same system with a second-harmonic perturbing field with a relative phase ϕ of 0 (blue) and $\pi/2$ (orange) rad, in which weak even harmonics are observed. From this, it is evident that the intensity of the even-harmonic signal at a given energy depends on the relative phase of the perturbing field.

The dependence of the even harmonic generation on the relative phase can be understood by superposing the perturbed dipole emission from the left and right half-cycles:

$$\begin{aligned} D(t) &= D_L(t)e^{i\sigma(k,t_b,t_r,\phi)} + D_R(t)e^{-i\sigma(k,t_b,t_r,\phi)} \\ &= D_L(t)\left(e^{i\sigma(k,t_b,t_r,\phi)} - e^{-i\sigma(k,t_b,t_r,\phi)}\right) \\ &\approx \sigma(k,t_b,t_r,\phi)D_L(t), \end{aligned} \tag{3.20}$$

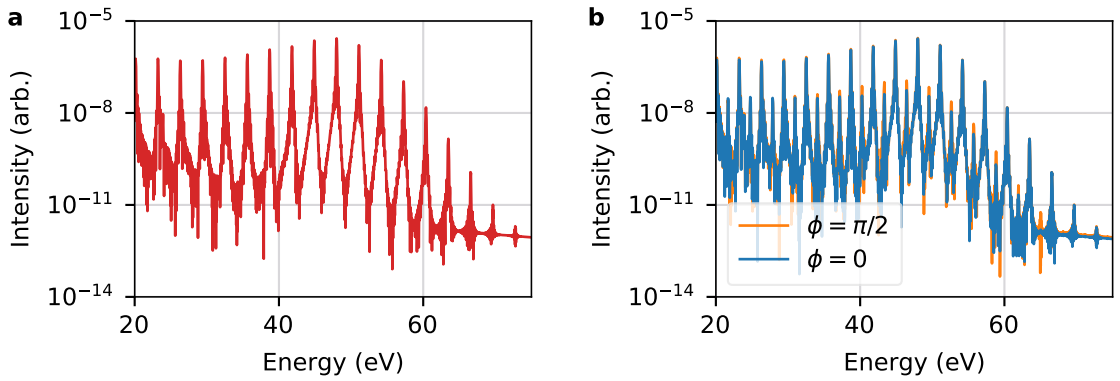

Figure 3.5 – (a) The unperturbed high harmonic spectrum from a one-dimensional TDSE simulation of an atom with an ionization potential of 24 eV. The driving field is a 30-cycle flat-top pulse of wavelength 800 nm and peak intensity of 1×10^{14} W/cm^2 (b) The high harmonic spectrum from the system in (a) with a second-harmonic perturbing field of relative intensity 10^{-4} and relative phase ϕ of 0 (blue) and $\pi/2$ (orange) rad. Due to the perturbing field, even harmonics are observed. The intensity of a given even harmonic depends on the relative phase ϕ.

since $\eta \ll 1$. The even-harmonic dipole spectrum is then found by taking the Fourier transform of eq. (3.20) at frequency $2n\omega_0$ (integer n):

$$\begin{aligned}\tilde{D}(2n\omega_0) &= \int_{-\infty}^{\infty} \Sigma(k, t_b, t_r) \cos\left(\phi - \theta(k, t_b, t_r)\right) D_L(t_r) e^{i2n\omega_0 t_r} dt_r \\ &\propto \frac{e^{i\Phi_{tot}(k,t_b,t_r)} \cos(\phi - \theta(k, t_b, t_r))}{\sqrt{\Phi''_{tot}(k, t_b, t_r)}},\end{aligned} \tag{3.21}$$

where the saddle-point solution of the integral in eq. (3.21) has been applied and

$$\Phi_{tot}(k, t_b, t_r) = -i \ln\left(D_L(t) + \Sigma(k, t_b, t_r)\right). \tag{3.22}$$

Thus, the variation of the even-harmonic intensity with ϕ reveals information about recollision dynamics through the function $\theta(k, t_b, t_r)$:

$$\left|\tilde{D}(2n\omega_0)\right|^2 \propto \cos^2\left(\phi - \theta(k, t_b, t_r)\right). \tag{3.23}$$

Fig. 3.6 depicts how the even-harmonic intensity varies with the relative phase ϕ acccording to eq. (3.23). The maximizing relative phase (red overlaid line) is calculated from $\theta(k, t_b, t_r)$ and varies linearly with respect to the recombination time t_r [19]. As ϕ is scanned, the relative phase which maximizes the even-harmonic signal, $\phi_{max} = \theta(k, t_b, t_r)$, is recorded and the emission times of the even harmonics can be determined, since $\theta(k, t_b, t_r)$ has an analytical expression.

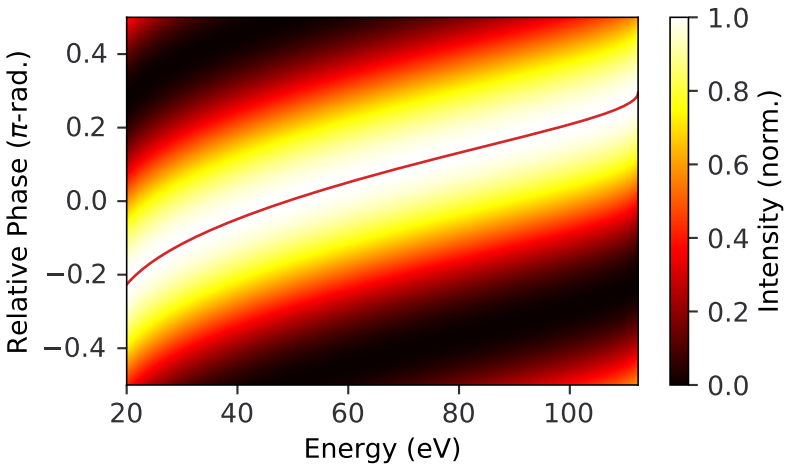

Figure 3.6 – The spectrogram depicting the variation of the even-harmonic intensity with the relative phase between the perturbing and driving fields in a collinear *in situ* experiment. The overlaid red line depicts relative phase which maximizes the even-harmonic signal for each energy. The driving field intensity and wavelength are 1.0×10^{14} W/cm^2 and 1.8 µm, repsectively, and the ionization potential of the target atom is 15.8 eV. The relative intensity of the perturbing field is 10^{-4}.

3.2.2 Non-collinear $\omega - 2\omega$ Measurement

Context: This technique is used in the experimental *in situ* measurement of the group delay around the Cooper minimum in argon in Chapter 8 [40]. It is also used in an unrelated work, for which I performed theoretical analysis [41].

Since isolated attosecond pulses exhibit continuous spectra, the use of even-harmonics as a background-free measurement of isolated attosecond pulses cannot be accomplished. Consequently, *in situ* measurement was extended to the measurement of isolated attosecond pulses by introducing the perturbing beam at an angle with respect to the driving field. The perturbing field directs the perturbed attosecond pulse emission off-axis at an angle which depends on both the XUV photon energy and the delay between the driving and perturbing fields. The non-collinear *in situ* measurement of an isolated attosecond pulse was devised and first accomplished by Kim *et al.* in 2013 [39]. Although different in implementation, the non-collinear method operates similarly to the collinear case.

The experimental diagram for this measurement is shown in Fig. 3.7. (a) The driving (red) and perturbing (blue) fields are focused into a gas jet at a relative angle θ_p and a time-delay τ. (b) Due to the non-collinear geometry, the time-delayed second-harmonic perturbing field modulates the generated XUV wavefronts (red to blue), resulting in a delay and energy-dependent deflection angle $\theta_\Omega(\tau)$. The far-field spectrum is then recorded in an XUV spectrometer and the deflection angle of each spectral component is recorded as a function of

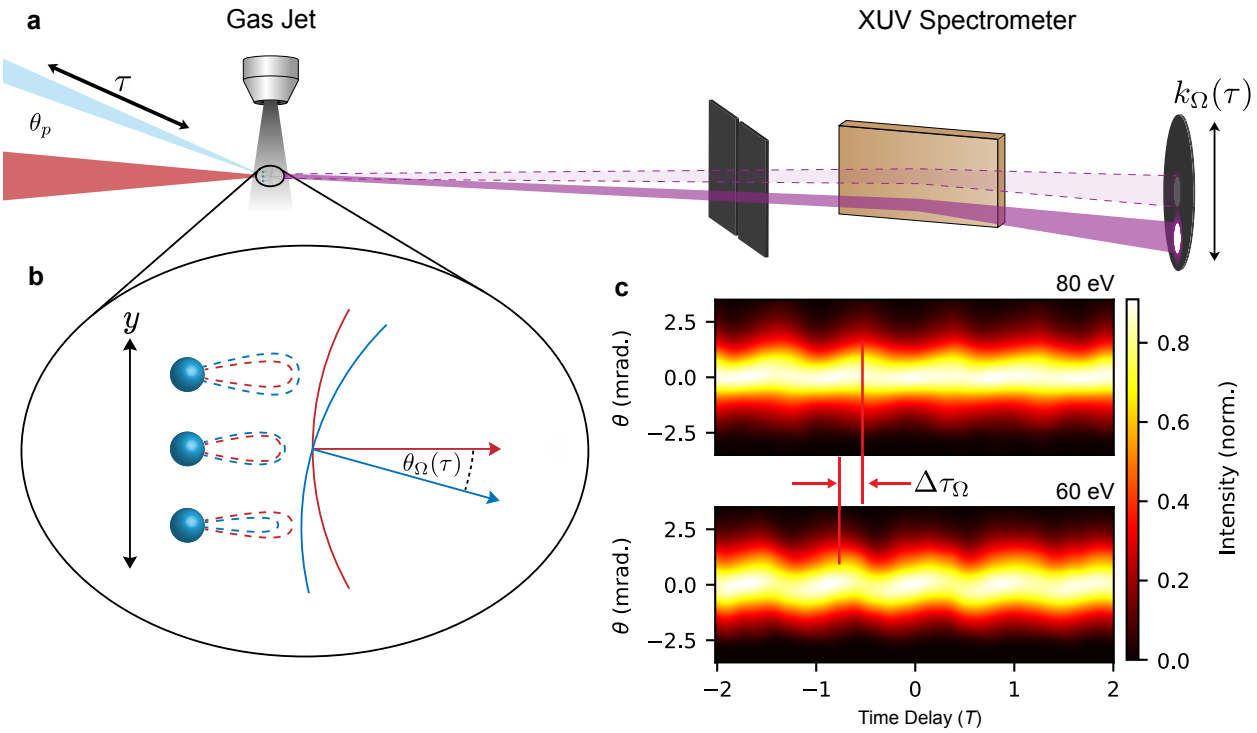

Figure 3.7 – (a) For the non-collinear $\omega - 2\omega$ *in situ* measurement, the driving field (red) and a perturbing second harmonic (light blue) with time delay τ and relative angle θ_p are focused into the gas jet. As shown in (b), the perturbation modulates the recollision trajectories across the driving beam front (red to blue). The wavefront of each frequency component of the perturbed XUV beam is modified (red to blue), resulting in a delay- and energy-dependent propagation angle $\theta_\Omega(\tau)$ with respect to the unperturbed beam (dashed purple lines). For each spectral component, the modulations in $\theta_\Omega(\tau)$ are recorded in the XUV spectrometer as a function of time delay. (c) The relative phase of the modulations in $\theta_\Omega(\tau)$ between two energies is proportional to the difference in each energy's group delay. This is shown for energies 80 (top) and 60 eV (bottom).

time delay. (c) The phase difference between the recorded modulations for different energies reveals the difference in group delay $\Delta\tau_\Omega$ for these energies, as shown for the frequencies 80 (top) and 60 eV (bottom) recorded from the argon measurement presented in Chapter 8.

The relative phase ϕ between the perturbing and driving fields depends both on the time delay τ between the two pulses and the vertical position y along the beam front:

$$\phi = k_p \theta_p \left(y - \frac{c\tau}{\theta_p} \right), \tag{3.24}$$

where k_p is the wave-vector of the perturbing field and c is the speed of light. In the near-field, the dipole emission at frequency Ω and position y, $\tilde{D}(\Omega, y)$, is described as follows:

$$\tilde{D}(\Omega, y) = \tilde{D}_0(\Omega, y)\,(1 + \alpha_\Omega(\phi))\,e^{i\sigma_\Omega(\phi)}, \tag{3.25}$$

where $\alpha_\Omega(\phi)$, $\tilde{D}_0(\Omega, y)$ is the unperturbed dipole emission, and $\sigma_\Omega(\phi)$ are the amplitude and phase modulations of the dipole emission at frequency Ω due to the perturbing field, respectively [39]. The phase modulation is as given in eq. (3.13) and depends linearly on the emission time for frequency Ω [19].

The observed dipole spectrum in the far-field can then be approximated as follows:

$$\tilde{D}^{(far)}(\theta_y, \phi) = \int_{-\infty}^{\infty} \tilde{D}(\Omega, y)\,(1 + \alpha_\Omega(\phi))\,e^{i\sigma_\Omega(\phi)} e^{ik_\Omega \theta_y y} dy. \tag{3.26}$$

The effect of the perturbing field can be expressed using a gate function $G(y - c\tau/\theta_p)$:

$$G\left(y - \frac{c\tau}{\theta_p}\right) = \left(1 + \alpha_\Omega\left(y - \frac{c\tau}{\theta_p}\right)\right) e^{i\sigma_\Omega(y - c\tau/\theta_p)}. \tag{3.27}$$

Thus, the observed intensity spectrum in the far-field is described as

$$\left|\tilde{D}^{(far)}(\Omega, y - \frac{c\tau}{\theta_p})\right|^2 = \left|\int_{-\infty}^{\infty} \tilde{D}(\Omega, y) G\left(y - \frac{c\tau}{\theta_p}\right) e^{ik_\Omega \theta_y y} dy\right|^2. \tag{3.28}$$

The spectrogram described by eq. (3.28) is the same form as used in FROG. A phase retrieval algorithm is then used to uniquely determine the terms $\tilde{D}(\Omega, y)$ and $G(y - c\tau/\theta_p)$ and, thus, characterize the attosecond pulse intensity and phase up to a constant. The y-dependence of the measurement has been used to characterize isolated attosecond pulses in both space and time [39, 41].

3.2.3 Single Image *In Situ* Measurement

Context: The single-image *in situ* technique [29] is used in the *ab initio* simulations of *in situ* measurement in multielectron systems presented in Chapter 7 and Chapter 9.

The single-image *in situ* measurement technique [29] extends *in situ* measurement to a regime wherein attosecond measurement can be accomplished using a single image of the generated XUV spectrum. The experimental diagram for the single-image *in situ* measurement is depicted in Fig. 3.8. (a) Like the non-collinear $\omega - 2\omega$ measurement, a weak perturbing field is focused into the gas jet at an angle θ_p relative to the driving field. In this case, however, the perturbing field frequency is the same as the fundamental driving field, ω_0. (b) This results in a modulation of the recollision trajectories (red to blue) and, thus, the generated XUV beam front across the driving field beam. The XUV beam in the gas jet is then re-imaged onto the XUV spectrometer using a pair of toroidal mirrors and spectrally resolved. (c) The spectrally resolved near-field dipole image is then used to measure recollision dynamics, as explained below.

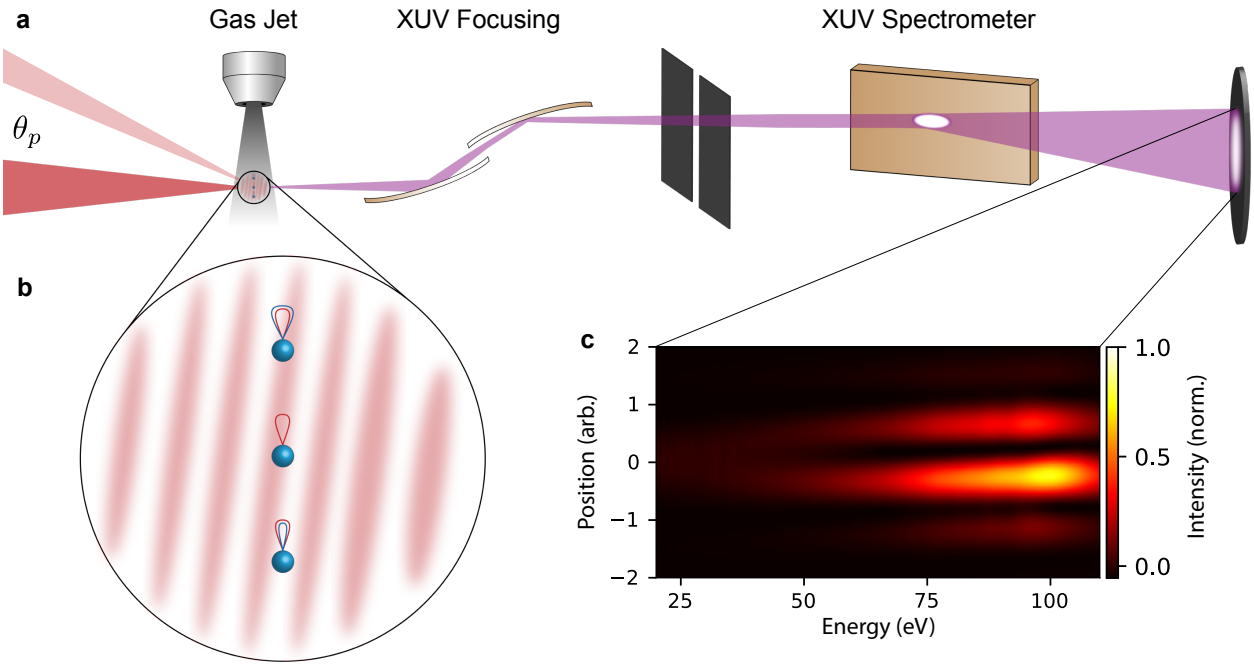

Figure 3.8 – The experimental diagram for the single-image *in situ* measurement. (a) A strong beam (dark red) and oblique weak perturbing field (light red) are focused into a gas jet. (b) The non-collinear geometry results in an optical grating in the gas jet which modulates recollision trajectories (red to blue) and, thereby, the near-field XUV wavefronts. (c) The near-field XUV beam is then imaged onto the XUV spectrometer using a pair of focusing toroidal mirrors and the near-field modulations due to the perturbing field are recorded.

Due to the non-collinear geometry, an effective time delay, $\tau(y)$, which depends on the vertical position y is introduced between the driving and perturbing fields:

$$\tau(y) = \frac{y}{c} \sin(\theta_p), \tag{3.29}$$

This leads to a phase difference between the perturbing and driving fields $\phi(y) = k_0 y \sin(\theta_p)$. The near-field dipole spectrum at frequency Ω can then be described as follows:

$$\begin{aligned} \tilde{D}(y,\Omega) &= \int_{-\infty}^{\infty} dt_r D(t) e^{i\sigma(k,t_b,t_r,\phi(y))} e^{i\Omega t_r} \\ &\propto D(y,t_r) e^{i\sigma(k,t_b,t_r,\phi(y))} e^{i\Omega t_r} \\ &\approx D(y,t_r)\left(1 - i\sigma_0(k,t_b,t_r,\phi)\right) e^{i\Omega \bar{t}_r}, \end{aligned} \tag{3.30}$$

where the integral in the first line is solved using the saddle-point approximation in the second line. As before, $\sigma_0(k,t_b,t_r,\phi)$ in the single-image *in situ* measurement can be decomposed into fast and slowly varying components:

$$\begin{aligned}\sigma_0(k, t_b, t_r, \phi) &= \sigma_c(k, t_b, t_r)\sin(\phi) + \sigma_s(k, t_b, t_r)\cos(\phi) \\ &= \Sigma(k, t_b, t_r)\cos\left(\phi(y) - \theta(k, t_b, t_r)\right),\end{aligned} \tag{3.31}$$

where

$$\sigma_c(k, t_b, t_r) = \frac{A_0(-2t_b\omega_0 + \sin(2t_b\omega_0) + 2t_r\omega_0 - \sin(2t_r\omega_0)) + 4k\cos(t_b\omega_0) - 4k\cos(t_r\omega_0)}{4\omega_0}, \tag{3.32}$$

$$\sigma_s(k, t_b, t_r) = -\frac{(\sin(t_b\omega_0) - \sin(t_r\omega_0))(A_0(\sin(t_b\omega_0) + \sin(t_r\omega_0)) + 2k)}{2\omega_0}, \tag{3.33}$$

$$\Sigma(k, t_b, t_r) = \sqrt{\sigma_s^2(k, t_b, t_r) + \sigma_c^2(k, t_b, t_r)}, \tag{3.34}$$

$$\theta(k, t_b, t_r) = \arctan\left(\frac{\sigma_c(k, t_b, t_r)}{\sigma_s(k, t_b, t_r)}\right). \tag{3.35}$$

With this,

$$\left|\tilde{D}(y, \Omega)\right|^2 \propto \left|D(\bar{t}_r)\right|^2 \left(1 + \Sigma^2(k, t_b, t_r)\cos^2(\phi - \theta(k, t_b, t_r)\right). \tag{3.36}$$

The only dependence on $\phi(y)$ is within the cosine term. Thus, the spectral intensity is maximized when

$$\phi(y) = \theta(k, t_b, t_r). \tag{3.37}$$

By imaging the near-field dipole emission, the variation of the attosecond pulse spectrum with $\phi(y)$ can be directly observed and the position at which the spectrum is maximized is mapped to $\phi(y)$ and, thereby, the recollision dynamics using eq. (3.37).

3.3 Comparing *In Situ* and *Ex Situ* Measurement

The widespread adoption of *in situ* measurement has been encumbered by a critical difference between the two measurements, stemming from where during the recollision process the measurement is performed. Since *ex situ* measurements are performed after the generation of the attosecond pulse, it is well-accepted that *ex situ* techniques fully characterize an attosecond pulse. This includes the transition moment between the ground state and continuum in both the generating and target atoms, which is often the parameter of interest. There is little controversy about this and attosecond *ex situ* measurement is viewed as the most robust form of attosecond measurement. On the other hand, *in situ* measurements are a measurement of the recollision electron wave packet and their domain of measurement is less clear. The importance of this was demonstrated by Spanner *et al.* [9], who compared simulated *in situ* and *ex situ* measurements. They studied HHG from a one-dimensional

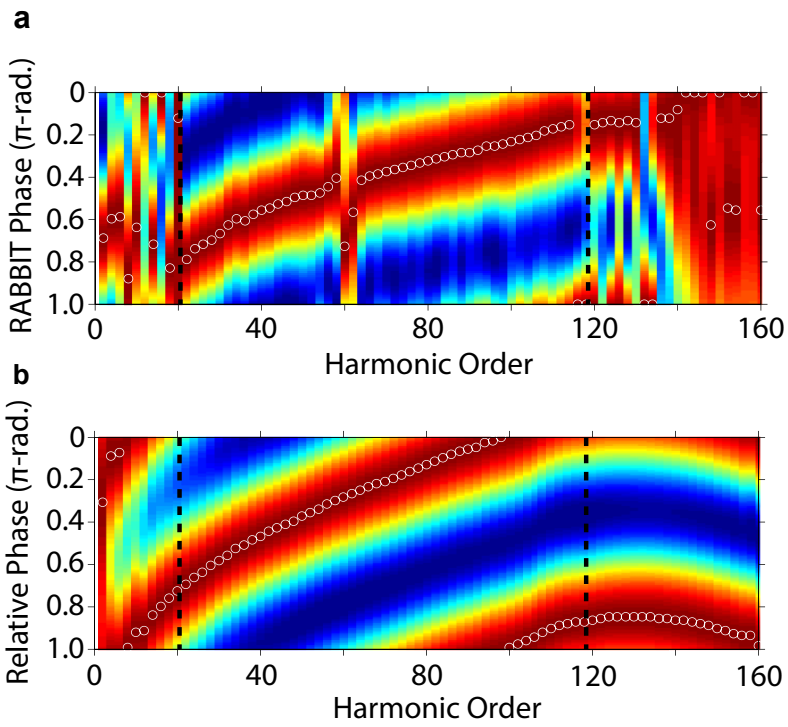

Figure 3.9 – The results of simulated (a) *ex situ* and (b) *in situ* measurements of recollision in a one-dimensional two-centre molecule. While the *ex situ* measurement is sensitive to the phase jump due two-centre interference near harmonic 60, the phase jump is completely absent in the *in situ* result. These figures are adapted with permission from [9].

diatomic molecule. Due to two-centre interference arising from the ionic structure of the molecule, the transition moment exhibits a spectral minimum and corresponding phase shift which is reflected in the emitted HHG spectrum. The results of their simulated *ex situ* and *in situ* measurements are shown in Fig. 3.9 (a) and (b), respectively. While the *ex situ* result clearly reflects the phase variation due to the two-centre interference near the 60^{th} harmonic, this phase variation is completely absent from the *in situ* result. From this, it was concluded that *in situ* measurement is insensitive to the transition moment phase.

This view is supported by QRS, as described in Chapter 2. Within QRS, it is assumed that the recollision electron wave packet is independent of its target and that the recombination transition moment is unaffected by the laser field. From eq. (2.48), the dipole spectrum from a target system with a transition moment phase within QRS is

$$\tilde{D}^{(T)}(\Omega) = \frac{a_{rec}^{(T)}(\Omega)}{a_{rec}^{(0)}} \tilde{D}^{(0)}(\Omega), \tag{3.38}$$

where the superscripts (0) and (T) correspond to a simple atom and the target system, respectively, $a_{rec}^{(j)}(\Omega)$ is the recombination component of the dipole spectrum ($j = 0, T$), and

$\tilde{D}^{(0)}(\Omega)$ is the dipole spectrum from the simple atom. Identifying $W^{(0)}(\Omega) = \frac{D^{(0)}(\Omega)}{a^{(0)}_{rec}(\Omega)}$ as the recollision electron wave packet and letting $a^{(T)}_{rec}(\Omega) = |a^{(T)}_{rec}(\Omega)|e^{i\Phi(\Omega)}$, the perturbed dipole emission from a collinear $\omega - 2\omega$ measurement within QRS can be expressed as

$$\begin{aligned}\left|\tilde{D}^{(T)}(\Omega)\right|^2 &\propto \left||a^{(T)}_{rec}(\Omega)|e^{i\Phi(\Omega)}W^{(0)}(\Omega)\cos\left(\phi - \theta^{(0)}(k,t_b,t_r)\right)\right|^2 \\ &\propto \cos^2\left(\phi - \theta^{(0)}(k,t_b,t_r)\right),\end{aligned} \tag{3.39}$$

where $\theta^{(0)}(k,t_b,t_r)$ is the maximizing phase from the simple system. That is, QRS predicts *in situ* measurement to be insensitive to the transition moment phase.

Within recollision, the signatures of electronic structure and dynamics within the generating medium of interest to most researchers are typically encoded onto the emitted radiation during the recombination step. Due to this apparent insensitivity to transition moment phase shifts, the utility of *in situ* measurement within attosecond science appears limited to the measurement of continuum dynamics which are well-described by the SFA and have been studied extensively.

Summary: With the methodology of *in situ* measurement established, I can now investigate the sensitivity of these techniques to the transition moment phase. The transition moment phase shifts investigated here, however, result from electronic structure and dynamics in multielectron systems. Thus, the next two chapters detail the theory and programs developed to simulate such systems.

Part II

Theory and Methods

Chapter 4

Describing Multielectron Systems

Outline: The theories used in this thesis to describe multielectron systems are briefly described. This includes reduced dimensional systems and time-dependent density functional theory.

4.1 The Schrödinger Equation for Single- and Many-Particle Systems

For a single-active electron, the Schrödinger equations reads as follows:

$$i\frac{\partial\psi}{\partial t} = \left(-\frac{\Delta}{2} + v_0(\mathbf{r})\right)\psi(\mathbf{r},t), \tag{4.1}$$

where $\psi(\mathbf{r},t)$ is the electron wavefunction at position $\mathbf{r}$ and time t, Δ is the Laplacian operator, and $v_0(\mathbf{r})$ is the external potential. Extending this to include multiple electrons is straight-forward [42]:

$$i\frac{\partial\psi}{\partial t} = \left(\sum_{m=1}^{N_e}\left(-\frac{\Delta_m}{2} + v_0\left(\mathbf{r}_m\right)\right) + \frac{1}{2}\sum_{m\neq n}\frac{1}{|\mathbf{r}_m - \mathbf{r}_n|}\right)\psi\left(\mathbf{r}_1,\cdots,\mathbf{r}_{N_e},t\right), \tag{4.2}$$

where $\mathbf{r}_m$ and Δ_m are the position and Laplacian acting on the m^{th} electron, $1/|\mathbf{r}_m - \mathbf{r}_n|$ represents the Coulomb interaction between the m^{th} and n^{th} electrons, and the wavefunction $\psi(\mathbf{r}_1,\cdots,\mathbf{r}_{N_e})$ has $3N_e$ dimensions.

In three-dimensions, describing systems with more than two electrons using eq. (4.2) is not yet possible with current computational methods and resources. This is because the number of points required for describing the multielectron wavefunction scales exponentially with both grid size and the number of electrons. For example, $N_x^{3N_e}$ distinct points are required to describe an N_e-electron wavefunction on a three-dimensional grid consisting of N_x points in each dimension. Exact solutions for three-dimensional multielectron systems have only been accomplished for the case of two electrons. Consequently, approximations to

the exact many-body wavefunction are required [43].

Many strategies designed to circumvent this issue have been employed in order to approximate multielectron systems. This includes multi-configuration Hartree-Fock [44], configuration-interaction singles [45] (doubles, etc...), and particle-in-cell approaches [46]. In this thesis, reduced dimensional models [47] and density functional theory [48] are both used to describe multielectron systems and will be briefly described here.

4.2 Reduced Dimensional Systems

Reduced dimensional models are a conceptually simple approach to describe multielectron systems. By considering a system consisting of one-dimensional electrons, the dimensionality of the multielectron problem is sufficiently reduced such that exact solutions to eq. (4.2) can be achieved relatively easily. While many aspects of true three-dimensional systems are lost in this description, these models treat multielectron interaction within the confines of the model exactly. This allows for the study of double-excitation beyond conventional approximate multielectron theories. Here, I use this model to study recollision-induced double excitation in a one-dimensional helium atom.

In one dimension, the Hamiltonian for a single electron system is given as follows:

$$\hat{\mathbf{H}} = -\frac{1}{2}\frac{\partial^2}{\partial x^2} + v_0(x), \tag{4.3}$$

where x is the electron position and $v_0(x)$ is the ionic potential. The two-electron Hamiltonian for the one-dimensional helium atom is a natural extension of this:

$$\hat{\mathbf{H}}_{2e} = -\frac{1}{2}\left(\frac{\partial^2}{\partial x_1^2} + \frac{\partial^2}{\partial x_2^2}\right) + v_0(x_1) + v_0(x_2) + v_{ee}(x_1, x_2), \tag{4.4}$$

where x_j is the position of the j^{th} electron and $v_{ee}(x_1, x_2)$ represents the electron-electron interaction potential. Both $v_0(x_j)$ and $v_{ee}(x_1, x_2)$ are approximated by a soft-core Coulomb potential:

$$v_0(x) = -\frac{Z}{\sqrt{x^2 + \alpha^2}}, \tag{4.5}$$

$$v_{ee}(x_1, x_2) = \frac{1}{\sqrt{(x_1 - x_2)^2 + \beta^2}}, \tag{4.6}$$

where the parameters α and β soften the Coulomb singularity at the origin. I consider a spin-singlet state such that the spatial wavefunction is symmetric. The Hamiltonian in eq. (4.4) does not depend on spin and, thus, the spin of the wavefunction is conserved throughout time propagation. The numerical implementation of this model is described in Chapter 5

and is used in Chapter 7 to study Fano resonances in recollision.

4.3 Density-Functional Theory

One of the most widely used approximations used to describe many-electron systems is density functional theory (DFT) [49]. DFT circumvents the exponential increase in required computational resources for describing many-electron systems by approximating the system as N non-interacting three-dimensional electron orbitals which are related through the three-dimensional electron density. This is done using functionals of the electron density which approximate the effective potentials arising from electron correlation in the exact system.

DFT has exhibited tremendous success in describing the electronic structure of atoms, molecules [50], and solid-state media [51]. DFT is especially suited for the strong-field dynamics considered here for two reasons [52]: (i) during strong-field processes, the interaction with the strong-field typically dominates over electron exchange and correlation effects; (ii) collective behaviour observed in recollision, such as plasmonic resonances [8], are well-described by DFT [48].

4.3.1 Ground State Density Functional Theory

DFT was first derived as a time-independent theory used to describe the ground state of multielectron systems. The foundation for ground state DFT was established through two theorems known as the Hohenberg-Kohn theorems [53]. The first theorem relates a system's ground state electron density and potential.

Theorem 1. The external potential, $v_{ext}(\mathbf{r})$, and hence the total energy, is a unique functional of the electron density, $n(\mathbf{r})$.

The electron density is found through the many-body wavefunction as follows:

$$n(\mathbf{r}_1) = N_e \int \Psi^* \left(\{\mathbf{r}_j\}_{j=1}^{N_e}\right) \Psi \left(\{\mathbf{r}_j\}_{j=1}^{N_e}\right) d\mathbf{r}_2 \cdots d\mathbf{r}_{N_e}, \tag{4.7}$$

where N_e is the number of electrons in the system, $\mathbf{r}_j$ is the position of the j^{th} electron, and $\Psi\left(\{\mathbf{r}_j\}_{j=1}^{N_e}\right)$ is the exact many-electron wavefunction. The correspondence between the electron density and potential can be established using a proof by contradiction. It is first assumed that there are two distinct potentials, $v_1(\mathbf{r})$ and $v_2(\mathbf{r})$, which result in the same ground state electron density. The two potentials produce two Hamiltonians, $\hat{\mathbf{H}}_1$ and $\hat{\mathbf{H}}_2$, which have two different ground states, $|\Psi_1\rangle$ and $|\Psi_2\rangle$.

Let $E_0^{(1)}$ and $E_0^{(2)}$ denote the ground state energies for the first and second systems, respectively. Since $\hat{\mathbf{H}}_1 \neq \hat{\mathbf{H}}_2$ and $|\Psi_1\rangle \neq |\Psi_2\rangle$, the following must be true:

$$
\begin{aligned}
E_0^{(1)} &< \left\langle \Psi_2 \middle| \hat{\mathbf{H}}_1 \middle| \Psi_2 \right\rangle \\
&= \left\langle \Psi_2 \middle| \hat{\mathbf{H}}_2 \middle| \Psi_2 \right\rangle + \left\langle \Psi_2 \middle| \hat{\mathbf{H}}_1 - \hat{\mathbf{H}}_2 \middle| \Psi_2 \right\rangle \\
&= E_0^{(2)} + \int n_0(\mathbf{r}) \left[v_1(\mathbf{r}) - v_2(\mathbf{r}) \right] d\mathbf{r}.
\end{aligned} \tag{4.8}
$$

A similar expression can be found by interchanging the subscripts:

$$
E_0^{(2)} < E_0^{(1)} + \int n_0(\mathbf{r}) \left[v_2(\mathbf{r}) - v_1(\mathbf{r}) \right] d\mathbf{r}. \tag{4.9}
$$

Adding eqs. (4.8) and (4.9) yields a contradiction, proving the correspondence between the ground state electron density and the ground state potential:

$$
E_0^{(1)} + E_0^{(2)} < E_0^{(1)} + E_0^{(2)}. \tag{4.10}
$$

Theorem 2. The ground state energy can be obtained variationally: the density that minimizes the total energy is the exact ground state density.

Since the first theorem establishes the relationship between the density and potential, the density must then also determine the ground state wavefunction. This can be expressed through a functional relationship relating the total energy to the electron density:

$$
E\left[n\right](\mathbf{r}) = \int n(\mathbf{r}) v_0(\mathbf{r}) d\mathbf{r} + F\left[n\right](\mathbf{r}), \tag{4.11}
$$

where $v_0(\mathbf{r})$ is the external potential and $F[n](\mathbf{r})$ is an unknown functional of the electron density. With the relationship between the electron density and the ground state potential and wavefunction established (aside from the form of $F[n](\mathbf{r})$), a practical method for finding the ground state density is required. Walter Kohn and Lu Jeu Sham developed a framework known as Kohn-Sham DFT which outlines this procedure.

A set of N_e fictitious non-interacting electron orbitals $\{\phi_j\}_{j=1}^{N_e}$, known as Kohn-Sham orbitals, whose density is identical to a system of interest is defined. The determination of the ground state can be accomplished by dividing the functional $F[n]$ into three contributions:

$$
F[n] = T_0[n] + E_H[n] + E_{xc}[n], \tag{4.12}
$$

where $T_0[n]$ is the exact kinetic energy functional, $E_H[n]$ is the energy from the classical electron-electron repulsion (i.e. the Hartree energy), and $E_{xc}[n]$ is the energy from electron exchange-correlation effects. This is then used with a Lagrange parameter μ in order to perform a minimization of $E[n](\mathbf{r}) - \mu N_e$. This leads to the following:

$$\begin{aligned}\mu &= \frac{\delta T_0}{\delta n(\mathbf{r})} + \frac{\delta E_H}{\delta n(\mathbf{r})} + \frac{\delta E_{xc}}{\delta n(\mathbf{r})} + v_0(\mathbf{r}) \\ &= \frac{\delta T_0}{\delta n(\mathbf{r})} + v_h[n](\mathbf{r}) + v_{xc}[n](\mathbf{r}) + v_0(\mathbf{r}),\end{aligned} \tag{4.13}$$

where $v_h[n](\mathbf{r})$ and $v_{xc}[n](\mathbf{r})$ are the potentials due to the Hartree and exchange-correlation interactions. Although the kinetic energy functional is not known, it is approximated through the kinetic energy of each electron orbital:

$$T_0[v_{eff}] = \sum_j \langle \varphi_j | \hat{\mathbf{T}} | \varphi_j \rangle, \tag{4.14}$$

where $\hat{\mathbf{T}}$ is the single-particle kinetic energy operator and $\varphi_j(\mathbf{r})$ is the j^{th} Kohn-Sham orbital. The classical Hartree potential is calculated by solving the Poisson equation for the electron density:

$$v_h[n](\mathbf{r}) = \int \frac{n(\mathbf{r}')}{|\mathbf{r} - \mathbf{r}'|} d\mathbf{r}. \tag{4.15}$$

The exchange-correlation potential, $v_{xc}[n](\mathbf{r})$, is calculated using a functional of the electron density, $\epsilon_{(\xi)}[n](\mathbf{r})$, for the total exchange-correlation energy, where ξ denotes the approximation for the functional used. With this,

$$E_{xc}[n](\mathbf{r}) = \int \epsilon_{(\xi)}[n](\mathbf{r}) n(\mathbf{r}) d^3r. \tag{4.16}$$

From eqs. (4.13) and (4.16), the exchange-correlation potential is given as

$$v_{xc}^{(\xi)}[n](\mathbf{r}) = \epsilon_{(\xi)}[n](\mathbf{r}) + n(\mathbf{r}) \frac{\delta \epsilon_{(\xi)}[n](\mathbf{r})}{\delta n(\mathbf{r})}. \tag{4.17}$$

The principal approximation used in DFT is the approximation to the functional describing exchange and correlation effects, for which the true form is unknown. Many approximations to this functional exist. The most commonly used approximation is the local-density approximation (LDA) [49], which is the exact solution for the functional for a homogeneous electron gas. The exchange-correlation potential arising from this approximation is

$$v_{xc}^{(LDA)}(r) = -\left(\frac{3}{\pi}\right)^{1/3} n^{1/3}(r). \tag{4.18}$$

Although surprisingly effective, this approximation is insufficient for describing atomic systems and needs to be supplemented. Here, an extension of the LDA which uses both the electron density and its gradient is used. This class of functionals is referred to as generalized gradient approximation (GGA) functionals. I use the LB94 functional [54], for which the exchange-correlation potential is given as follows:

$$v_{xc}^{(LB94)}(r) = v_{xc}^{(LDA)}(r) - \beta \left(\frac{n(r)}{2}\right)^{1/3} \frac{x^2}{1 + 3\beta \operatorname{arcsinh}(x)}, \tag{4.19}$$

$$x = \frac{|\nabla n|}{n^{4/3}(\mathbf{r})}. \tag{4.20}$$

Thus, the entire system can be described using an effective single-body potential, $v_{eff}[n](\mathbf{r})$,

$$v_{eff}[n](\mathbf{r}) = v_0(\mathbf{r}) + v_h[n](\mathbf{r}) + v_{xc}^{(\xi)}[n](\mathbf{r}). \tag{4.21}$$

In this thesis, two atomic systems are modelled using DFT: argon and xenon. The LB94 functional adequately reproduces the ionization potentials and orbital energies of both systems (see Table 8.1 and 9.1 for the Kohn-Sham orbital energies in argon and xenon, respectively).

The multielectron system can then be solved using methods similar to those in solving single-active electron systems, as the system is described through a non-interacting Hamiltonian, known as the Kohn-Sham Hamiltonian, and can be diagonalized directly:

$$\hat{\mathbf{H}}_{ks} = -\frac{\Delta}{2} + v_{eff}[n](\mathbf{r}), \tag{4.22}$$

where Δ is the Laplacian operator.

4.3.2 Time-Dependent Density Functional Theory

In 1984, Runge and Gross developed a time-dependent extension of DFT [55]. They established a one-to-one mapping between the time-dependent electron density and the time-dependent potential for a given initial state. Time-dependent density functional theory (TD-DFT) permits the real-time propagation of multielectron systems [56], allowing for the calculation of excitations and the dipole response from multielectron systems. The foundation for TD-DFT is based on minimization of the action functional.

Like in ground state DFT, an effectively single-particle Schrödinger equation, known as the time-dependent Kohn-Sham equation, is used to describe the time propagation of the multielectron system:

$$i\frac{\partial \varphi}{\partial t} = \left\{-\frac{\Delta}{2} + v_0(\mathbf{r}, t) + v_h[n](\mathbf{r}, t) + v_{xc}^{(\xi)}[n](\mathbf{r}, t)\right\} \varphi(\mathbf{r}, t), \tag{4.23}$$

where $\varphi(\mathbf{r}, t)$ is a Kohn-Sham orbital. This brief description summarizes the essential elements of TD-DFT used here.

4.3.3 Limitations of TD-DFT

Although TD-DFT is a profoundly useful method to describe multielectron systems, it is important to understand its limitations. Implementations of TD-DFT are necessarily approximate solutions to the multielectron TDSE, as the exact form of the exchange-correlation potential $v_{xc}[n](\mathbf{r},t)$ is unknown. These limitations have become known as the *deadly sins* of TD-DFT [48]:

— Errors in the ground state will lead to errors in time-dependent calculations.

— Although $v_{xc}[n](\mathbf{r},t)$ is known to be non-local in space, the most widely used and practical approximations to it are local (or semi-local through the gradient of the electron density).

— Similarly, $v_{xc}[n](\mathbf{r},t)$ is known to be dependent on the electron density for all times $t' \leq t$. However, virtually all implementations of TD-DFT use an adiabatic approximation which calculate $v_{xc}[n](\mathbf{r},t)$ from the density at time t alone. This leads to a poor description of multiple excitations within TD-DFT and is why reduced dimensional systems are used to investigate double-excitation in this work.

— Kohn-Sham orbitals are only eigenstates of an auxiliary system which yields the same ground state density. Consequently, observables calculated from interactions between orbitals are not generally equivalent to those calculated from the exact wavefunction.

Despite this, TD-DFT is useful in describing the recollision processes investigated here. The dipole moment, the observable through which recollision dynamics are measured, is calculated directly from the electron density:

$$D(t) = \int \mathbf{r}\, n(\mathbf{r},t) d^3r. \tag{4.24}$$

Further, I use DFT to investigate recollision dynamics in argon and xenon. The approximations to $v_{xc}[n](\mathbf{r},t)$ used here accurately describe the ground state of these systems (see Chapters 8 and 9). Thus, the Cooper minimum in argon, which results from the electronic structure of the ground state, is well-described within TD-DFT. With regards to xenon, plasmonic and collective excitations are well-described by TD-DFT and this is reflected in the calculated attosecond pulse spectra.

Summary: This short description of DFT is by no means complete. For interested readers, a good summary of recent developments in TD-DFT can be found in [48]. The next chapter describes the numerical implementation of the theory presented in this chapter.

Chapter 5

Numerical Methods for Solving Multi-electron Systems

Outline: This chapter describes the numerical programs developed for this thesis to describe strong-field processes in multi-electron atomic and molecular systems. In particular, the general-purpose graphical processing unit implementation of the one-dimensional helium model and spin-restricted time-dependent density functional theory for azimuthally symmetric systems using the NVIDIA CUDA-C framework is described.

The programs described here were developed from scratch and optimized to perform simulated two pulse strong field experiments. They are used in three publications of mine [57, 58, 40] and are available for use. Access is described in Appendix A.

5.1 One-Dimensional Helium Model

Working within the length gauge and dipole approximation, the time-dependent Schrödinger equation for the one-dimensional helium atom is given as follows:

$$i\frac{\partial\psi}{\partial t} = \left\{ -\frac{1}{2}\left(\frac{\partial^2}{\partial x_1^2} + \frac{\partial^2}{\partial x_2^2}\right) + v_0(x_1) + v_0(x_2) + v_{ee}(x_1, x_2) + (x_1 + x_2)F(t) \right\}\psi(x_1, x_2, t), \tag{5.1}$$

where x_j is the position of the j^{th} electron, $v_0(x_j)$ is the ionic potential felt by the j^{th} electron as given by eq. (4.5), $v_{ee}(x_1, x_2)$ represents the multi-electron interaction potential as in eq. (4.6), and $F(t)$ is the external time-dependent electric field. The softening parameters used in the soft-core ionic and electron-electron potentials, α and β, respectively, are tuned ($\alpha^2 = 0.5, \beta^2 = 0.339$) such that the neutral and singly-ionized ground state energies, E_g and $E_g^{(+)}$, match those of the three-dimensional helium atom (i.e. $E_g = -79$ eV and $E_g^{(+)} = -54.4$ eV). The system is represented on a uniform grid with 2048 grid points with

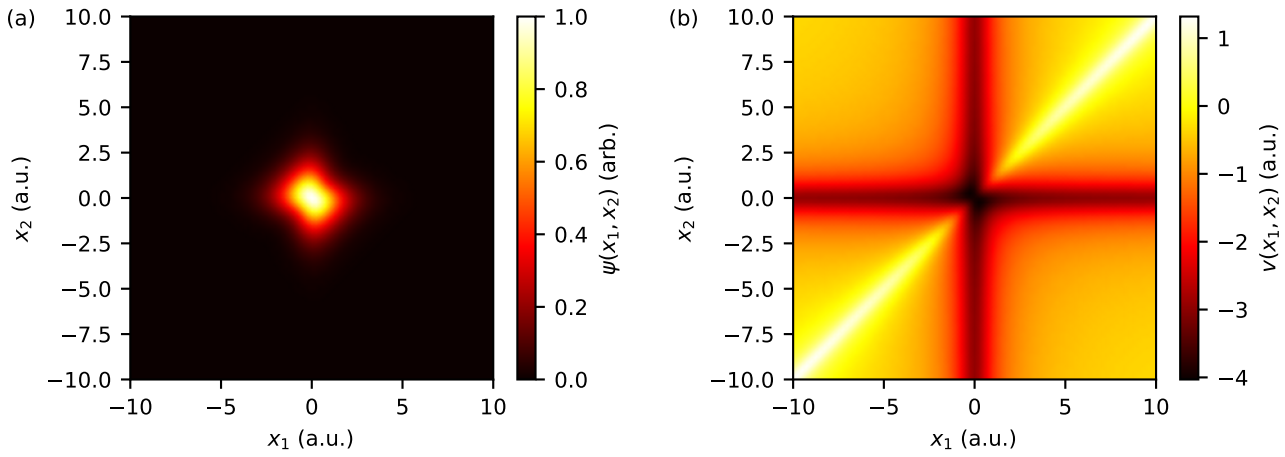

Figure 5.1 – (a) The ground state wavefunction for the one-dimensional helium atom found with the Hamiltonian defined in eqs. (4.4 - 4.6). (b) The total potential for the one-dimensional helium atom from eqs. (4.5) and (4.6). The numerical softening parameters ($\alpha^2 = 0.5$ and $\beta^2 = 0.339$) are tuned such that the ground state energies of the one-dimensional helium atom and its single-ion state agree with the three-dimensional helium atom.

a spacing of 0.25 a.u. Such a large computational grid was chosen to ensure contributions to the dipole acceleration from long trajectories and the reflection of the components of the continuum wave packet from the absorbing boundary are minimized.

Given that each electron is described using a one-dimensional Cartesian grid, the total Hamiltonian can be partitioned into components diagonal in position- and momentum-space ($\hat{\mathbf{H}}_0^{(x)}$ and $\hat{\mathbf{H}}_k^{(k)}$, respectively):

$$\hat{\mathbf{H}}_0^{(x)} = v_0(x_1) + v_0(x_2) + v_{ee}(x_1, x_2) + (x_1 + x_2)E(t), \tag{5.2}$$

$$\hat{\mathbf{H}}_0^{(k)} = \frac{\hat{k}_1^2 + \hat{k}_2^2}{2}, \tag{5.3}$$

where $\hat{k}_j$ is the momentum operators for the j^{th} electron. Therefore, the natural method to calculate the time advancement of the wavefunction is the Fourier split-step method [59]. The algorithm for the Fourier split-step method is shown in Algorithm 1. For each propagation step δ_t, the time interval is divided and $\hat{\mathbf{H}}_0^{(x)}$ is applied first over an interval $\delta_t/2$. The Fourier transform of the wavefunction is then calculated and $\hat{\mathbf{H}}_0^{(k)}$ is applied over an interval δ_t. Finally, the position-space wavefunction is calculated using an inverse Fourier transform, after which $\hat{\mathbf{H}}_0^{(x)}$ is applied over an interval $\delta_t/2$.

The ground state calculation is also calculated using this algorithm, using imaginary time propagation, and is accomplished by substituting $\delta_t \to -i\delta_t$ and $F(t) = 0$. An initial

guess for the ground state wavefunction is made and propagated in imaginary time until the wavefunction converges to the ground state. The result of this calculation and the total potential are shown in Fig. 5.1 (a) and (b), respectively.

Algorithm 1 Time propagation using the Fourier split-step method

for $j = 0$ to N_t **do**

$\psi(x_1, x_2) \rightarrow \exp\left[-i\left(H_0^{(x)}(x_1, x_2) + (x_1 + x_2)E(t_k)\right)\frac{\delta_t}{2}\right]\psi(x_1, x_2)$

$\psi(k_1, k_2) = \mathrm{FFT}\left[\psi(x_1, x_2)\right]$

$\psi(k_1, k_2) \rightarrow \exp\left[-iH_0^{(k)}\delta_t\right]\psi(k_1, k_2)$

$\psi(x_1, x_2) = \mathrm{FFT}^{-1}\left[\psi(k_1, k_2)\right]$

$\psi(x_1, x_2) \rightarrow \exp\left[-i\left(H_0^{(x)}(x_1, x_2) + (x_1 + x_2)E(t_k)\right)\frac{\delta_t}{2}\right]\psi(x_1, x_2)$

end for

The dipole acceleration spectrum at frequency Ω, $\tilde{a}(\Omega)$ is calculated at each time step using the Ehrenfest theorem and the ionic potential $v_{tot}(x_1, x_2) = v_0(x_1) + v_0(x_2)$:

$$\tilde{a}(\Omega) = \int \langle\psi(x_1, x_2, t)|\left(-\frac{\partial v_{tot}}{\partial x_1} - \frac{\partial v_{tot}}{\partial x_2} + E(t)\right)|\psi(x_1, x_2, t)\rangle e^{i\Omega t}dt. \tag{5.4}$$

The short-trajectory component of the recollision dipole are selected through the use of a transmission-free absorbing boundary [5].

This model is implemented in a general-purpose graphical processing unit (GP-GPU) program using NVIDIA CUDA-C [60]. It can be used to simulate one-dimensional two-electron or one-electron two-dimensional systems. Access to this program is given in Appendix A.

5.2 Implementation of Density Functional Theory

The time-dependent Kohn-Sham equation is given as follows:

$$i\frac{\partial\varphi_\alpha}{\partial t} = \left(-\frac{\Delta}{2} + v_0(\mathbf{r}) + v_h[n](\mathbf{r}, t) + v_{xc}[n](\mathbf{r}, t)\right)\varphi_\alpha(\mathbf{r}, t), \tag{5.5}$$

where Δ is the Laplacian operator, $v_0(\mathbf{r})$ is the external potential, $v_h[n](\mathbf{r}, t)$ is the Hartree potential (i.e. classical Coulomb repulsion between electrons), $v_{xc}[n](\mathbf{r}, t)$ is the exchange-correlation potential, and $\varphi_\alpha(\mathbf{r}, t)$ is a Kohn-Sham orbital at position $\mathbf{r}$ and time t. The systems considered here all exhibit spherical symmetry. This is exploited by describing the Kohn-Sham orbitals using a spherical harmonic expansion:

$$\varphi_\alpha(\mathbf{r}, t) = \sum_{l=0}^{N_L}\sum_{m=-l}^{l}\varphi_{\alpha;l,m}(r, t)Y_{l,m}(\Theta), \tag{5.6}$$

where N_L is the maximum considered orbital angular momentum, $\varphi_{\alpha;l,m}(r,t)$ is the component of the Kohn-Sham orbital with orbital angular momentum l and magnetic quantum number m, and $Y_{l,m}(\Theta)$ is the spherical harmonic of orbital angular momentum at solid angle Θ. Further, all external fields considered here are are linearly polarized and parallel. Thus, the magnetic quantum number, m_α, for the α^{th} Kohn-Sham orbital is a constant of motion and is determined by the electron configuration of the considered system:

$$\varphi_\alpha(\mathbf{r},t) = \sum_{l=m_\alpha}^{N_l} \varphi_{\alpha;l}(r) Y_{l,m_\alpha}(\Theta). \tag{5.7}$$

Numerically, $\phi_\alpha(\mathbf{r},t)$ is represented as a matrix whose columns are each of the orbital's l-components:

$$\varphi_\alpha(\mathbf{r},t) = \begin{pmatrix} \varphi_{\alpha;m_\alpha}(r,t) & \varphi_{\alpha;m_\alpha+1}(r,t) & \cdots \varphi_{\alpha;L}(r,t) \end{pmatrix}. \tag{5.8}$$

The interaction with the external electric field $\mathbf{F}(t)$ polarized along $\hat{\mathbf{z}}$ is described using the dipole approximation. With this, the time-dependent Kohn-Sham equation including the strong field for each l-component of the α^{th} orbital is given as

$$i\frac{\partial \varphi_{\alpha;l}}{\partial t} = \left(-\frac{1}{2}\frac{\partial^2}{\partial r^2} + \frac{l(l+1)}{2r^2} + v_0(r) + v_h[n](\mathbf{r},t) + v_{xc}[n](\mathbf{r},t) + F(t) r\cos(\theta) \right) \varphi_{\alpha;l}(r,t). \tag{5.9}$$

The methods used to describe each of the terms in this will be described below.

5.2.1 The Radial Grid

The radial grid is described using Gauss-Lobatto quadrature [61]. With this, the radius r is mapped to $x \in [-1,1]$:

$$r(x) = \frac{R_{max}\zeta}{2}\frac{1+x}{1-x+\zeta}, \tag{5.10}$$

where R_{max} corresponds to the maximum radius of the simulation and ζ is a parameter controlling the variation of $r(x)$ with x. The endpoints of the grid are fixed at $x = \pm 1$ and not included within the radial vector. The inner points are evaluated at the zeros of the first-derivative of the N_g^{th} Legendre polynomial, where $N_g = N_r + 1$. With this, any function $f(x)$ can be expressed as follows:

$$f(x) \approx \sum_{k=0}^{N_g} a_k P_k(x) = \sum_{k=0}^{N_g} f(x_k) g_k(x), \tag{5.11}$$

where $g_k(x)$ is the cardinal function of the grid:

$$g_k(x) = -\frac{1}{N_g(N_g+1)P_{N_g}(x_k)}\frac{(1-x^2)P'_{N_g}(x)}{x-x_k}. \tag{5.12}$$

With this, the ij^{th} element of the second-order radial derivative matrix, $\hat{\mathbf{D}}_r^{(2)}$ is given as follows [62]:

$$\hat{\mathbf{D}}_{r;i,j}^{(2)} = \begin{cases} N_g(N_g+1)(N_g(N_g+1)-2)/24 & i=j \text{ and } i,j \in [0,N_g] \\ [N_g(N_g+1)-2]/4 & i \neq j \text{ and } i,j \in [0,N_g] \\ -N_g(N_g+1)/[3(1-x_i^2)] & i=j \text{ and } i,j \notin [0,N_g] \\ -2/(x_i-x_j)^2 & i \neq j \text{ and } i,j \notin [0,N_g] \end{cases}. \tag{5.13}$$

The numerical representation of the α^{th} Kohn-Sham orbital $\tilde{\varphi}_{\alpha,l}[r](x)$, absorbs the variation of the grid with respect to x and is normalized such that

$$\tilde{\varphi}_{\alpha,l}[r](x_k) = \frac{1}{N}\frac{\sqrt{r'(x_k)}}{P_{N_g}(x_k)}\varphi[r](x_k), \tag{5.14}$$

where N is the normalization constant.

5.2.2 The Hartree Potential

The calculation of the Hartree potential depends on the electron density. With the α^{th} Kohn-Sham orbital as given by eq. (5.6) and g_α representing its occupation number, the electron density is given as follows:

$$n(\mathbf{r},t) = \sum_\alpha g_\alpha (-1)^{m_\alpha} \sum_{l_1}\sum_{l_2} \varphi^*_{\alpha;l_1}(r)\varphi_{\alpha;l_2}(r) Y_{l_1,-m_\alpha}(\Theta) Y_{l_2,m_\alpha}(\Theta). \tag{5.15}$$

The Hartree potential can be found by using the multipolar expansion of the Coulomb interaction kernel [63]:

$$\frac{1}{|\mathbf{r}-\mathbf{r}'|} = \sum_L \frac{4\pi}{2L+1}\frac{r_<^L}{r_>^{L+1}} \sum_{M=-L}^{L} Y_{L,M}(\Theta) Y^*_{L,M}(\Theta'), \tag{5.16}$$

where $r_<$ ($r_>$) represents the smaller (larger) of the radii r and r' and Θ' represents the solid-angle for position $\mathbf{r}'$. With eqs. (5.15) and (5.16), the Hartree potential is then found to be the following:

$$\begin{aligned} v_h(\mathbf{r}) = \sum_L \frac{4\pi}{2L+1} \sum_{M=-L}^{L} Y_{L,M}(\Theta) \sum_\alpha g_\alpha (-1)^{m_\alpha+M} \sum_{l_1,l_2} \int_0^\infty \frac{r_<^L}{r_>^{L+1}} \varphi^*_{\alpha;l_1}(r')\varphi_{\alpha;l_2}(r')dr' \\ \times \int_{\Theta'} Y_{l_1,-m_\alpha}(\Theta') Y_{L,-M}(\Omega') Y_{l_1,m_\alpha}(\Theta') d\Theta'. \end{aligned} \tag{5.17}$$

I let $\xi^{l_2,m_\alpha}_{l_1,m_\alpha;L,M}$ denote the angular integral over Ω' in eq. (5.17). The integrals of the product of three spherical harmonics can be found using the Wigner-3J symbol [64]:

$$\begin{aligned}\xi^{l_2,m_\alpha}_{l_1,m_\alpha;L,M} &= \int_{\Theta'} Y_{l_1,-m_\alpha}(\Theta')Y_{L,-M}(\Theta')Y_{l_2,m_\alpha}(\Theta')d\Theta' \\ &= \sqrt{\frac{(2l_1+1)(2l_2+1)(2L+1)}{4\pi}} \begin{pmatrix} l_1 & L & l_2 \\ 0 & 0 & 0 \end{pmatrix} \begin{pmatrix} l_1 & L & l_2 \\ -m_0 & M & m_0 \end{pmatrix}.\end{aligned} \tag{5.18}$$

As the simulation is restricted to a linear polarization, all components with $M \neq 0$ are zero. The Hartree potential is calculated using eqs. (5.17) and (5.18) up to a maximum $L = 3$. With this, the Hartree potential is described as

$$v_h[n](\mathbf{r},t) \approx v_h^{(0)}[n](r,t) + v_h^{(1)}[n](r,t)\cos(\vartheta) + v_h^{(2)}[n](r,t)\frac{1}{2}\left(3\cos^2(\vartheta)-1\right), \tag{5.19}$$

where ϑ is the polar angle for position $\mathbf{r}$. The expressions for $v_h^{(l)}[n](r,t)$ are described below.

The Monopole Term For the monopole term, $L = M = 0$:

$$\xi^{l_2,m_\alpha}_{l_1,m_\alpha;0,0} = (-1)^{m_\alpha}\frac{1}{\sqrt{4\pi}}, \tag{5.20}$$

Therefore,

$$v_h^{(0)}(r) = \sum_\alpha g_\alpha \sum_l \int_0^\infty \frac{|\varphi_{\alpha;l}(r')|^2}{r_>}dr' \tag{5.21}$$

The Dipole Term For the dipole term, $L = 1$:

$$\xi^{l_2,m_\alpha}_{l_1,m_\alpha;1,0} = \sqrt{\frac{(2l_1+2)(3)(2l_2+1)}{4\pi}} \begin{pmatrix} l_1 & 1 & l_2 \\ -m_\alpha & 0 & m_\alpha \end{pmatrix} \begin{pmatrix} l_1 & 1 & l_2 \\ 0 & 0 & 0 \end{pmatrix}. \tag{5.22}$$

The last Wigner-3j symbol is zero unless $l_1 = l_2 \pm 1$. I first focus on the case for $l_1 = l_2 + 1 \equiv l + 1$:

$$\xi^{l+1,m_\alpha}_{l,m_\alpha;1,0} = (-1)^{m_\alpha}\sqrt{\frac{3}{4\pi}}\sqrt{\frac{(l+1)^2-m^2}{(2l+1)(2l+3)}}. \tag{5.23}$$

With this,

$$v^{(1)}_{h;l+1}(\mathbf{r},\vartheta) = \cos(\vartheta)\sum_{\alpha} g_\alpha \sum_l \sqrt{\frac{(l+1)^2 - m_\alpha^2}{(2l+1)(2l+3)}} \int_0^\infty \frac{r_<}{r_>^2}\varphi^*_{\alpha;l+1}(r')\varphi_{\alpha;l}(r')dr'. \tag{5.24}$$

For the case where $l_1 = l_2 - 1$,

$$v^{(1)}_{h;l-1}(\mathbf{r},\vartheta) = \cos(\vartheta)\sum_{\alpha} g_\alpha \sum_l \sqrt{\frac{l^2 - m_\alpha^2}{(2l+1)(2l-1)}} \int_0^\infty \frac{r_<}{r_>^2}\varphi^*_{\alpha;l-1}(r')\varphi_{\alpha;l}(r')dr'. \tag{5.25}$$

For simplicity, $c_{l,m}$ is defined as follows:

$$c_{l,m} = \sqrt{\frac{(l+1)^2 - m^2}{(2l+1)(2l+3)}}. \tag{5.26}$$

With this

$$\begin{aligned} v^{(1)}_h[n](r,\vartheta) &= \cos(\vartheta)\sum_{\alpha} g_\alpha \sum_l \int_0^\infty \left[c_{l,m}\varphi^*_{\alpha;l+1}(r) + c_{l-1,m}\varphi^*_{\alpha;l-1}(r)\right]\varphi_{\alpha;l}(r)dr' \\ &= \cos(\vartheta)u^{(1)}_h(r). \end{aligned} \tag{5.27}$$

The Quadrupole Term For the quadrupole term, $L = 2$:

$$\xi^{l+1,m_\alpha}_{l,m_\alpha;1,0} = \sqrt{\frac{(2l_1+1)(2l_2+1)(5)}{4\pi}} \begin{pmatrix} l_1 & 2 & l_2 \\ 0 & 0 & 0 \end{pmatrix} \begin{pmatrix} l_1 & 2 & l_2 \\ -m_0 & 0 & m_0 \end{pmatrix} \tag{5.28}$$

There are three cases to consider: $l_2 = l_1 - 2, l_2 = l_1, l_2 = l_1 + 2$. I first consider the case for $l_2 = l_1 - 2$:

$$\xi^{l+2,m_\alpha}_{l,m_\alpha;2,0} = (-1)^{m_\alpha}\frac{3}{2(2l+3)}\sqrt{\frac{5}{4\pi}}\sqrt{\frac{((l+1)^2 - m_\alpha^2)((l+2)^2 - m_\alpha^2)}{(2l+1)(2l+5)}}. \tag{5.29}$$

Since

$$Y_{2,0}(\Theta) = \frac{1}{2}\sqrt{\frac{5}{4\pi}}\left(3\cos^2(\vartheta) - 1\right), \tag{5.30}$$

$v^{(2)}_{h;l+2}(\mathbf{r},\vartheta)$ is given as

$$v^{(2)}_{h;l+2}(\mathbf{r},\vartheta) = \frac{1}{2}\left(3\cos^2(\vartheta)-1\right)\sum_\alpha g_\alpha \sum_l q_{l,m_\alpha}\int_0^\infty \frac{r^2_<}{r^3_>}\varphi^*_{\alpha;l+2}(r')\varphi_{\alpha;l}(r')dr', \tag{5.31}$$

where

$$q_{l,m_\alpha} = \frac{3}{2(2l+3)}\sqrt{\frac{((l+1)^2-m_\alpha^2)((l+2)^2-m_\alpha^2)}{(2l+1)(2l+5)}}. \tag{5.32}$$

For $l_2 = l-2$,

$$\xi^{l+2,m_\alpha}_{l,m_\alpha;2,0} = (-1)^{m_\alpha}\sqrt{\frac{5}{4\pi}}q_{l-2,m_\alpha}. \tag{5.33}$$

With this,

$$v^{(2)}_{h;l-2}(\mathbf{r},\vartheta) = \frac{1}{2}\left(3\cos^2(\vartheta)-1\right)\sum_\alpha g_\alpha \sum_l q_{l-2,m_\alpha}\int_0^\infty \frac{r^2_<}{r^3_>}\varphi^*_{\alpha;l-2}(r')\varphi_{\alpha;l}(r')dr', \tag{5.34}$$

For the $l_2 = l_1$ term,

$$\xi^{l,m_\alpha}_{l,m_\alpha;2,0} = (-1)^m\sqrt{\frac{5}{4\pi}}\frac{(l^2+l-3m^2)}{(2l-1)(2l+3)}. \tag{5.35}$$

Let $p_{l,m}$ be defined as follows:

$$p_{l,m} = \frac{l(l+1)-3m^2}{(2l-1)(2l+3)}. \tag{5.36}$$

With this,

$$v^{(2)}_{h;l-2}(\mathbf{r},\vartheta) = \frac{1}{2}\left(3\cos^2(\vartheta)-1\right)\sum_\alpha g_\alpha \sum_l p_{l,m_\alpha}\int_0^\infty \frac{r^2_<}{r^3_>}\left|\varphi_{\alpha;l}(r')\right|^2 dr', \tag{5.37}$$

The total quadrupole moment is then given as

$$\begin{aligned} v^{(2)}_h[n](r,\vartheta) = \frac{1}{2}\left(3\cos^2(\vartheta)-1\right)\sum_{\alpha,l} g_\alpha \int_0^\infty \frac{r^2_<}{r^3_>}\Big(& q_{l-2,m_\alpha}\varphi^*_{\alpha;l-2}(r') \\ & + p_{l,m}\varphi^*_{\alpha;l}(r') + q_{l,m}\varphi^*_{\alpha;l+2}(r')\Big)dr'. \end{aligned} \tag{5.38}$$

5.2.3 The Exchange-Correlation Potential

As mentioned in Chapter 4, the LB94 functional [54] is used to describe exchange-correlation effects. This functional supplements the LDA functional [49] with an expression related to the gradient of the electron density. The total exchange-correlation potential is given as

$$\begin{aligned} v_{xc}^{LB94}(r) &= v_{xc}^{(LDA)}(r) + v_{xc}^{(LB94)}[n, \nabla n](r) \\ &= -\left(\frac{3}{\pi}\right)^{1/3} n^{1/3}(r) - \beta \left(\frac{n(r)}{2}\right)^{1/3} \frac{x^2}{1 + 3\beta \operatorname{arcsinh}(x)}, \end{aligned} \tag{5.39}$$

where

$$x = \frac{|\nabla n|}{n^{4/3}(\mathbf{r})}. \tag{5.40}$$

Only the monopole term from the multipolar expansion of the exchange-correlation is retained. For the purposes of this work, this approximation is sufficient. The first application of the TD-DFT model studied here is the study of the Cooper minimum in argon, which results from the ground state electronic structure of argon and is well-described by the monopole term. The second application of the TD-DFT model is the study of the *giant dipole resonance* in xenon, which is well-described by the Hartree potential.

5.2.4 Ground State Calculation

The calculation of the ground state for the Kohn-Sham system requires the diagonalization of the Kohn-Sham Hamiltonian, $\hat{\mathbf{H}}_{ks}$:

$$\hat{\mathbf{H}}_{ks} = -\frac{\Delta}{2} + v_h[n](\mathbf{r}) + v_{xc}[n](\mathbf{r}). \tag{5.41}$$

The Hartree and exchange-correlation potentials and, thereby, the Kohn-Sham Hamiltonian depend on the ground state electron density. Consequently, the calculation of the ground state must be performed using an iterative algorithm, which is outlined in Algorithm 2.

An initial guess for the ground state is given by the set of orbitals found by diagonalizing eq. (5.41) with $v_h[n](\mathbf{r}) = v_{xc}[n](\mathbf{r}) = 0$. Here, the iterative process begins and the electron density is calculated from the set of Kohn-Sham orbitals. A linear combination of the new and old densities is then used to calculate the Hartree and exchange-correlation potentials. The weights of the new and old densities are ι and $\iota - 1$, respectively, with $\iota > 0$ and $\iota \ll 1$. This is done so as to avoid charge sloshing [65]. A new set of Kohn-Sham orbitals is then found by diagonalizing the Hamiltonian with the updated multielectron potentials. After each iteration, the convergence of each orbital's eigenvalue is calculated and the process repeats until all eigenvalues converge below a threshold ϵ_{min}.

Algorithm 2 DFT Ground State Calculation

Diagonalize hydrogenic atom with nuclear charge of Z and obtain set of Kohn-Sham orbitals $\{\varphi_j(r)\}_{j=1}^{N_e}$ and set of eigenvalues $\{E_j\}_{j=1}^{N_e}$.
Set $\epsilon = 1$.
Set initial density $n(\mathbf{r}) = 0$.
while $\max\{\epsilon_j\}_{j=1}^{N_e} > \epsilon_{min}$ **do**
    Calculate new electron density, $n_{new}(\mathbf{r})$.
    Mix new density with old: $n(\mathbf{r}) = \iota n_{new}(\mathbf{r}) + (1-\iota)n_{old}(\mathbf{r})$.
    Calculate Hartree and exchange-correlation potentials with $n(\mathbf{r})$.
    Diagonalize Hamiltonian including Hartree and exchange-correlation potentials and obtain new set of Kohn-Sham orbitals.
    Calculate convergence of eigenvalues, E_j, such that $\epsilon_j = |E_j^{(old)} - E_j^{(new)}|$.
end while

5.2.5 Time Propagation

Absorbing Boundary

In order to ensure only short trajectory contributions to the recollision dipole moment are included in the simulation, a complex absorbing potential is used, which is non-zero only for radii r greater than a fixed radius, R_{abc}. The absorbing boundary radius used is determined through the semi-classical excursion of an electron in an electric field of amplitude F_0 and frequency ω_0:

$$R_{abc} = \frac{F_0}{\omega_0^2}. \tag{5.42}$$

This corresponds to the maximum trajectory excursion of short-trajectories. I use a transmission-free absorbing boundary [5], which has been demonstrated to yield accurate results for strong-field proceesses [9, 66]. The absorbing boundary is incorporated into the Hamiltonian through the complex potential, $v_{abc}(r)$:

$$v_{abc}(r) = -iW(r), \tag{5.43}$$

where $W(r)$ is as given in [5].

The Propagator

The Hamiltonian acting on an orbital of angular quantum number l and magnetic quantum number m is given as follows:

$$\hat{\mathbf{H}} = \hat{\mathbf{H}}_0^{(l)} + \sum_{l_h=0}^{L_h} \hat{\mathbf{H}}_{(l_h)}, \tag{5.44}$$

$$\hat{\mathbf{H}}_0^{(l)} = -\frac{1}{2}\frac{\partial^2}{\partial r^2} + \frac{l(l+1)}{2r^2} + v_0(r) + v_h^{(0)}[n](r,0) + v_{xc}^{(0)}[n](r,0), \tag{5.45}$$

where $\hat{\mathbf{H}}_0^{(l)}(r)$ is is the ground state Hamiltonian for the l^{th} angular quantum number. A split-operator technique is used such that $\hat{\mathbf{H}}_0^{(l)}$, containing the multielectron potentials at time $t = 0$, remains static and is applied throughout the simulation. This allows for the propagator associated with this component to be calculated only once throughout the simulation.

The l_h^{th} multipole potentials are described with the Hamiltonian components $\hat{\mathbf{H}}_{(l_h)}$. The changes in the monopole multielectron interaction potentials from the initial ground state potentials are applied separately from $\hat{\mathbf{H}}_0^{(l)}$ in $\hat{\mathbf{H}}_{(0)}(t)$, which also includes the component of the quadrupole moment which couples with $l_h = 0$. The $\hat{\mathbf{H}}_{(l_h)}$ for $l_h \geq 1$ describe the higher-order multipolar expansion of the time-dependent multielectron interaction and interaction with an external field. For a Kohn-Sham orbital with angular and magnetic quantum numbers l and m,

$$\hat{\mathbf{H}}_{(0)}(t) = \Delta v_h^{(0)}[n](r,t) + p_{l,m} v_h^{(2)}(r,t) + \Delta v_{xc}^{(0)}[n](r,t), \tag{5.46}$$

$$\hat{\mathbf{H}}_{(1)}(t) = \hat{\mathbf{L}}^{(m)} \otimes \left(\hat{\mathbf{I}}_r \left(rF(t) + v_h^{(1)}[n](r,t)\right)\right), \tag{5.47}$$

$$\hat{\mathbf{H}}_{(2)}(t) = \hat{\mathbf{P}}^{(m)} \otimes \left(\hat{\mathbf{I}}_r v_h^{(2)}[n](r,t)\right), \tag{5.48}$$

$$\hat{\mathbf{L}}^{(m)} = \begin{pmatrix} 0 & c_{m,m} & 0 & 0 & \dots \\ c_{m,m} & 0 & c_{m+1,m} & 0 & \dots \\ 0 & c_{m+1,m} & 0 & c_{m+2,m} & \dots \\ 0 & 0 & c_{m+2,m} & 0 & \dots \\ \vdots & \vdots & \vdots & \vdots & \ddots \end{pmatrix}, \tag{5.49}$$

$$\hat{\mathbf{P}}^{(m)} = \begin{pmatrix} 0 & 0 & q_{m,m} & 0 & \dots \\ 0 & 0 & 0 & q_{m+1,m} & \dots \\ q_{m,m} & 0 & 0 & 0 & \dots \\ 0 & q_{m+1,m} & 0 & 0 & \dots \\ \vdots & \vdots & \vdots & \vdots & \ddots \end{pmatrix}, \tag{5.50}$$

where $\Delta v_h^{(0)}[n](r,t) = v_h^{(0)}[n](r,t) - v_h^{(0)}[n](r,0)$ and $\Delta v_{xc}^{(0)}[n](r,t) = v_{xc}^{(0)}[n](r,t) - v_{xc}^{(0)}[n](r,0)$ are the changes of the monopole multielectron interaction potential from the ground state results, $\hat{\mathbf{L}}^{(m)}$ and $\hat{\mathbf{P}}^{(m)}$ are the angular coupling matrices acting in the $l \geq m$ subspace, $\hat{\mathbf{I}}_r$ is the identity matrix in real-space, and $F(t)$ is the external electric field.

The full propagator for the l^{th} angular momentum component of a given orbital, $\hat{\mathbf{U}}^{(l)}(\delta_t)$ for a time-step δ_t is then calculated using a split-step algorithm:

$$\hat{\mathbf{U}}^{(l)}(\delta_t) = \left(\prod_{l_h=L_h}^{0} \exp\left(-i\frac{\delta_t}{2}\hat{\mathbf{H}}_{(l_h)}(t)\right)\right) \exp\left(-i\delta_t\hat{\mathbf{H}}_0^{(l)}(t)\right) \left(\prod_{l_h=0}^{L_h} \exp\left(-i\frac{\delta_t}{2}\hat{\mathbf{H}}_{(l_h)}(t)\right)\right), \tag{5.51}$$

where L_h is the order of the multipole expansion for the electron-electron interaction potential. For the monopole terms of the Hamiltonian acting on the ground state orbitals, the exponential of the Hamiltonian is expressed through the Crank-Nicholson method:

$$\exp\left(-i\delta_t\hat{\mathbf{H}}_0^{(l)}(t)\right) \approx \left(\hat{\mathbf{I}}_r + i\frac{\delta_t}{2}\hat{\mathbf{H}}_0^{(l)}\right)^{-1} \left(\hat{\mathbf{I}}_r - i\frac{\delta_t}{2}\hat{\mathbf{H}}_0^{(l)}\right). \tag{5.52}$$

For the monopole terms with l greater than a threshold L_0, this is expressed through a split-step operator method in order to circumvent numerical issues due to the stiffness of the Hamiltonian including the centrifugal barrier:

$$\begin{aligned}\exp\left(-i\delta_t\hat{\mathbf{H}}_0^{(l)}(t)\right) \approx \exp\left(-i\frac{\delta_t}{2}\frac{l(l+1)}{r^2}\right) \left(\hat{\mathbf{I}}_r + i\frac{\delta_t}{2}\hat{\mathbf{H}}_0^{(0)}\right)^{-1} \left(\hat{\mathbf{I}}_r - i\frac{\delta_t}{2}\hat{\mathbf{H}}_0^{(0)}\right) \\ \times \exp\left(-i\frac{\delta_t}{2}\frac{l(l+1)}{r^2}\right).\end{aligned} \tag{5.53}$$

This is calculated in advanced and saved for repeated use at each time step during the simulation. Since the $\hat{\mathbf{H}}_{(l)}$ are diagonal in r, their exponentiation is calculated directly in l-space only once at the beginning of the simulation. Thus, the only components of its associated propagator $\hat{\mathbf{U}}^{(l)}$ calculated at each time step are the changes to the multielectron interaction potentials. The algorithm used for propagation is shown in Algorithm 3.

Algorithm 3 Time propagation for the TD-DFT

for $j = 0$ to N_t **do**
  Calculate electron density, Hartree potential, and exchange-correlation potential
  for $l_h = L_h$ to 0 **do**
    $\varphi_\alpha \to \hat{\mathbf{U}}^{(l_h)}\varphi_\alpha$
  end for
  $\varphi_\alpha \to \hat{\mathbf{U}}_0\varphi_\alpha$
  for $l_h = 0$ to L_h **do**
    $\varphi_\alpha \to \hat{\mathbf{U}}^{(l_h)}\varphi_\alpha$
  end for
end for

Calculation of Observables

For a dipolar observable operator, $\hat{\mathbf{f}}$, represented by a function $f(r)$, the expectation value $f(t) = \langle\hat{\mathbf{f}}\rangle$ is calculated as follows [67]:

$$\begin{aligned} f(t) &= \int d^3r \sum_{\alpha,l,l'} \left(\varphi^*_{\alpha;l}(r,t)Y^*_{l,m_\alpha}(\Theta)\right) f(r)\cos(\vartheta)\left(\varphi_{\alpha;l'}(r,t)Y_{l',m_\alpha}(\Theta)\right) \\ &= \sum_{\alpha,l} \int_0^\infty \left[c_{l,m_\alpha}\varphi^*_{\alpha;l+1}(r,t) + c_{l-1,m_\alpha}\varphi^*_{\alpha;l-1}(r,t)\right] f(r)\varphi_{\alpha;l}(r)dr. \end{aligned} \tag{5.54}$$

$f(r) = r$ for the calculation of the dipole moment and $f(r) = -\partial v/\partial r$ for the dipole acceleration. The dipole spectrum is then calculated by first multiplying the dipole moment by a Kaiser window function [68], taking its second-order time derivative, and evaluating the Fourier transform of the result.

5.2.6 GP-GPU Implementation and Program Access

The program is written in a combination of Python and the GP-GPU programming language CUDA-C. The ground state, numerical grid, and propagator matrices are initially calculated in Python and then used in the CUDA-C program which performs the time propagation. Access to the source code is provided in Appendix A.

Summary: With this, the theory behind attosecond pulse measurement and the framework of the simulation models has been established. The next four chapters describe the *in situ* measurement of transition moment phase shifts in a variety of systems using analytic theory, numerical simulation, and experiment.

Part III

In Situ Measurement and the Transition Moment Phase

Chapter 6

Attosecond *In Situ* Measurement and Photorecombination

Outline: The measurement of transition moment phase shifts in single active electron systems using attosecond *in situ* techniques is described using the strong field approximation and shown to depend on the nature of the transition moment phase shift. This is done by including the transition moment phase in the saddle-point analysis used in the strong field approximation and then incorporating the effect of the perturbing field on the transition moment phase. Then, the sensitivity of *in situ* techniques to the transition moment phase is demonstrated using a model argon atom exhibiting a Cooper minimum. Finally, it is shown that *in situ* measurement is insensitive to transition moment phase shifts due to ionic structure due to the quantum path interference nature of two-centre interference.

The work presented in this chapter is based entirely on my own research and is included in one publication of mine [69].

When the SFA was first published, the important issue was high harmonic pulse production and the potential of using extreme nonlinear optics for measurement was not addressed [2]. Yet the formalism introduced in that paper clarifies the controversial issue of the sensitivity of *in situ* measurement to the transition moment phase, just as it clarified the issue of attosecond pulse production at the time it was published.

The controversy can be understood by considering the three-step model of high harmonic generation [1]. Although not stated at the time, the three steps appear independent [70]. QRS [24], introduced later, made the independence of the steps a formal assumption. If the steps are truly independent, then nonlinear optics can only measure those steps that are optically influenced and it is the recollision electron trajectory in the continuum that is most easily influenced. Thus, it would seem that nonlinear optics might have little to say about the dynamics of ionization or recombination.

However, one can easily understand an alternate perspective. The observation of coherent

radiation from recollision requires the recolliding electron to return to its initial state [2]. The requirement for recombination to the same initial state acts analogously to phase-matching in determining attosecond pulse emission. If the transition moment coupling the initial and continuum states is complex, then phase-matching favours components of the continuum electron wave packet appropriately phased with respect to both continuum dynamics and the transition moment. That is, the transition moment not only affects ionization and recombination, but which components of the continuum wave packet dominate dipole emission as well.

In this chapter, I will show how this occurs during recollision in single-active electron systems and, thereby, how fully optical measurements of attosecond dynamics can be accomplished. I do this by extending the SFA to account for phase shifts in the transition moment between bound and continuum states. I then describe the effect of the transition moment on *in situ* measurement [19] and investigate its application in systems with transition moment phase shifts due to spectral minima arising from electronic [71] and ionic structure [10, 9]. I then consider the effect of shape resonances in HHG [72]. These results show that the sensitivity of all-optical measurement to the transition moment phase depends on the nature of the phase shift. In particular, I show all-optical measurement is insensitive to phase shifts arising from ionic structure, but sensitive to phase shifts arising from electronic structure. The measurement of multielectron effects will be discussed in Chapters 7, Chapters 8, and 9.

6.1 The Strong-Field Approximation with a Transition Moment Phase

As in Chapter 2, I begin with a single-active electron atom with ground state $|\psi_0\rangle$ and ionization potential I_p interacting with a time-dependent strong laser field $\mathbf{F}(t)$ with vector potential $\mathbf{A}(t)$ polarized along $\hat{\mathbf{z}}$. Below, vector notation is omitted, as all parameters are parallel to $\hat{\mathbf{z}}$. I let $P(t) = k + A(t)$ denote the recollision electron kinetic momentum, where k is the electron canonical momentum. The same assumptions as in the original SFA [2] are used here: (i) the contribution of all bounds states except the ground state can be neglected, (ii) ground state depletion is neglected, and (iii) that the influence of the ionic potential in the continuum is neglected.

Within the SFA, the time-dependent recollision dipole moment at time t_r can be expressed as follows:

$$D(t_r) = -i \int dk \int_{-\infty}^{t_r} dt_b d^* \left(P(t_r)\right) e^{-i[S(k,t_b,t_r)+I_p(t_r-t_b)]} F(t_b) \cdot d\left(P(t_b)\right), \tag{6.1}$$

where t_b is the time of ionization, t_r is the time of recombination, $S(k, t_b, t_r)$ is the semiclassical action, and $d(k)$ is the complex transition moment along $\hat{z}$,

$$d(k) = \langle k|z|\psi_0\rangle. \tag{6.2}$$

In addition to the evolution of the ground state and the semi-classical action, I include the phase of the transition moment in the saddle-point analysis below. Proceeding similarly to QRS [24], I incorporate the known transition moment phase $\Phi(k) = \arg(d(k))$ at momentum k into the integrand. Working within the time domain, the total integrand phase is

$$\Phi_{tot}(k, t_b, t_r) = S(k, t_b, t_r) + I_p(t_r - t_b) + \Phi\left(P(t_b)\right) - \Phi\left(P(t_r)\right), \tag{6.3}$$

where $I_p(t_r - t_b)$ describes the evolution of the ground state. The inclusion of the transition moment phase in the saddle-point analysis yields the following set of modified saddle-point equations for the dipole moment in the time domain:

$$0 = \int_{t_b}^{t_r} P(\tau)d\tau - \Phi'(P(t_r)) + \Phi'(P(t_b)), \tag{6.4}$$

$$0 = \frac{P^2(t_b)}{2} + I_p + F(t_b)\Phi'(P(t_b)). \tag{6.5}$$

It must be noted that the application of the saddle-point approximation is only suitable for systems in which the transition moment phase shift varies sufficiently slowly over a small energy range. The model argon and diatomic molecular systems both exhibit transition moment phase shifts which permit the use of the saddle-point analysis. Before describing these systems, however, I first discuss how *in situ* measurement is affected by the transition moment phase.

6.2 Adapting *In Situ* Measurement to a Transition Moment Phase

I consider a collinear $\omega - 2\omega$ measurement using sinusoidal fields, as described in Chapter 3, for simplicity. *In situ* measurement was originally described in systems where the transition moment phase is slowly varying (i.e. $\Phi'(k) \approx 0$). Accordingly, the effect of the perturbing field is included solely within the semi-classical action $S(k, t_b, t_r)$ and the perturbation-induced phase shift due to the modified action is as given in eq. (3.11):

$$\sigma_0(k, t_b, t_r, \phi) = \int_{t_b}^{t_r} [k + A(\tau)] \cdot A_p(\tau, \phi)d\tau. \tag{6.6}$$

Here, however, I am interested in the case where the transition moment phase is not slowly varying and cannot be neglected. In this case, the total perturbation-induced phase shift is found by expanding the total phase in eq. (6.3) with $P(t) \to P(t) + A_p(t, \phi)$ to first-order in η and is given as follows:

$$\sigma(k, t_b, t_r, \phi) = \sigma_0(k, t_b, t_r, \phi) + A_p(t_b, \phi)\Phi'(P(t_b)) - A_p(t_r, \phi)\Phi'(P(t_r)). \tag{6.7}$$

Thus, the perturbation-induced phase shift is affected by the transition moment in two ways. First, the transition moment affects the saddle-point solutions directly and, thus, affects the change to the semi-classical action, $\sigma_0(k, t_b, t_r, \phi)$. Second, the measurement is affected by the influence of the perturbing field on the transition moment.

Like in Chapter 3, I work with sinusoidal driving and perturbing fields. Consequently, the perturbation-induced phase shift including the effect of the perturbing field on the transition moment can be factored into rapidly and slowly varying components, $\Sigma(k, t_b, t_r)$ and $\cos(\phi - \theta(k, t_b, t_r))$, respectively, using eqs. (3.10), (3.11), and (6.7) as follows [19]:

$$\begin{aligned}\sigma(k, t_b, t_r, \phi) &= \sigma_c(k, t_b, t_r)\sin(\phi) + \sigma_s(k, t_b, t_r)\cos(\phi) \\ &= \Sigma(k, t_b, t_r)\cos(\phi - \theta(t_b, t_r)),\end{aligned} \tag{6.8}$$

where $\Sigma(k, t_b, t_r)$ and $\theta(t_b, t_r)$ can be found using the same methods as in Chapter 3. Thus, the variation of the intensity of the $2n^{th}$ even harmonic with the relative phase ϕ can be analyzed similarly to a system without a transition moment phase shift:

$$\left|\tilde{D}(2N\omega_0, \phi)\right|^2 \propto \cos^2\left(\phi - \theta(k, t_b, t_r)\right), \tag{6.9}$$

where the effect of the transition moment is contained within $\theta(k, t_b, t_r)$. Since the even harmonic emission times are found through the maximizing phase, $\phi_{max} = \theta(k, t_b, t_r)$, the sensitivity of *in situ* measurement to the transition moment phase can be determined through the sensitivity of $\theta(k, t_b, t_r)$.

6.3 *In Situ* Measurement and the Transition Moment Phase

I now describe the saddle-point analysis and *in situ* measurement in systems exhibiting a transition moment phase shift. I first consider the case of a spectral minimum due to electronic structure within the transition moment, using the Cooper minimum in argon as an example [71]. This is explored in greater detail using my TD-DFT model in Chapter 8. I then consider the measurement of recollision in a diatomic molecule [10, 9], which exhibits a π-phase jump in its transition moment due to two-centre interference. Finally, I consider transition moment phase shifts due to shape resonances [72]. I will demonstrate that in situ measurement is generally sensitive to the transition moment phase, but insensitive to phase shifts arising from ionic structure.

For consistency, all the calculations presented in this chapter are done using a sinusoidal driving field with a wavelength of 1.8 µm and peak intensity of 1×10^{14} W/cm^2 and a perturbing co-polarized second-harmonic field with a relative intensity 10^{-4}.

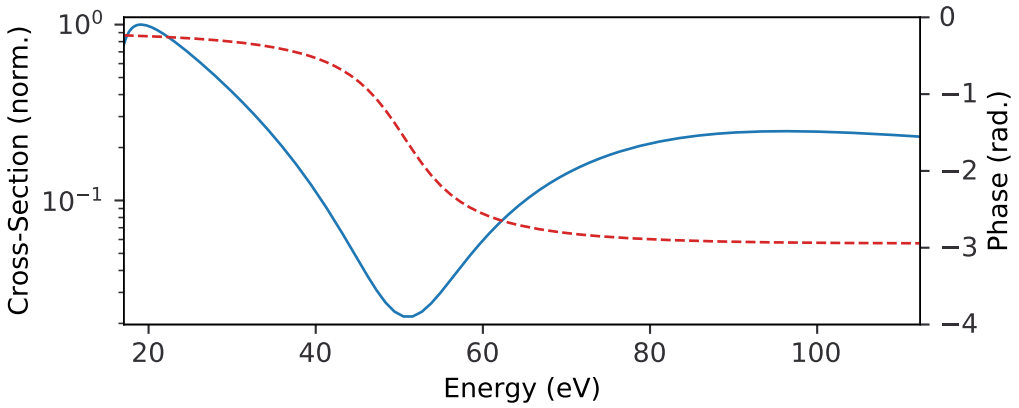

Figure 6.1 – The recombination cross-section (solid blue) and phase (dashed red) for the model argon atom are plotted on the left and right axes, respectively. A spectral minimum and π-phase shift occurs near 52 eV.

6.3.1 Spectral Minimum from Electronic Structure

I consider an atomic system of ionization potential 15.8 eV with a transition moment as depicted in Fig. 6.1, where the absolute cross-section (solid blue) and transition moment phase (dashed red) are shown. A spectral minimum and π-phase shift is observed near 52 eV. This model is chosen due to its similarity to the transition moment in argon [7]. The transition moment phase $\Phi(k)$ at momentum k from Fig. 6.1 is incorporated into the saddle-point analysis of the SFA by using the modified saddle-point equations (6.4) and (6.5).

The saddle-point solutions are found numerically and shown in Fig. 6.2. Fig. 6.2 (a) depicts the trajectory excursion time as a function of the emitted photon energy from the system including the transition moment phase (solid blue) and a reference equivalent system without the transition moment phase (dashed red). The excursion time for the system with the transition moment phase shift deviates from the reference system around 52 eV due to the transition moment phase shift. This difference is depicted in Fig. 6.2 (b) along the left axis (solid red) and is largest (−135 as) around the minimum.

Within eqs. (6.4) and (6.5), the gradient of the transition moment phase acts equivalently to a spatial offset. The return condition in eq. (6.4) is offset by the difference in the transition moment phase gradient at the times of ionization and recombination. Eq. (6.5), the condition for energy conservation during ionization, is shifted in energy equivalently to a dipole interaction with the driving electric field at a position equal to the transition moment phase gradient. Thus, it is expected that the relative positions of ionization and recombination will depend on the gradient of the transition moment phase. Fig. 6.2 (b) shows the difference between the positions of ionization and recombination, Δx, on the right axis (dashed blue). Clearly, the structure of Δx reflects the structure of the change in excursion time. In argon, the Cooper minimum results from the nodal structure of the ground state wavefunction [71], wherein the radial ground state wavefunction exhibits a tightly-bound in-

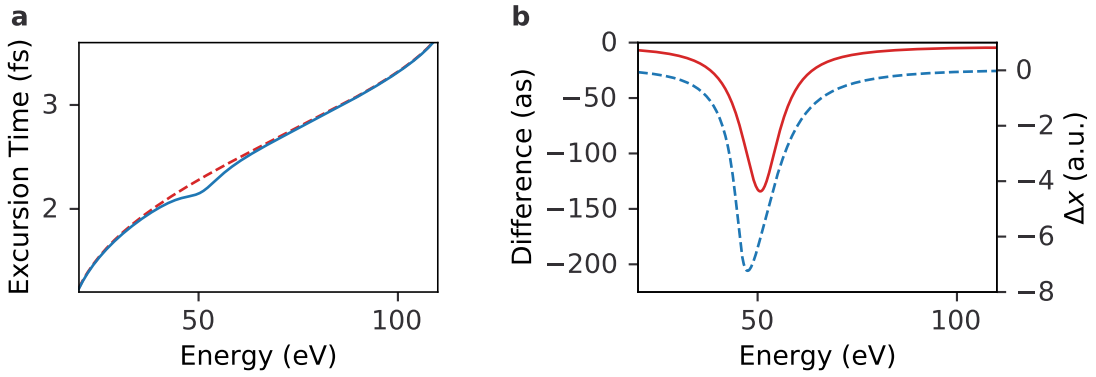

Figure 6.2 – (a) The short-trajectory excursion times as a function of emitted photon energy calculated with (solid blue) and without (dashed red) the transition-moment phase from Fig. 6.1 in eqs. (6.4) and (6.5). (b) The difference in excursion time between the systems with and without the transition moment phase from the excursion times presented in (a) (solid red) are plotted on the left axis. The difference in the positions of ionization and recombination as a function of energy (dashed blue) is plotted on the right axis.

ner lobe and a larger outer lobe with a radial extent of ~ 10 a.u. At the spectral minimum, the dipole emission from these lobes cancels. Passing through the minimum, the lobe which dominates dipole emission changes, resulting in the phase shift and a change in emission position. Thus, the variation in Fig. 6.2 (b) is interpreted as a consequence of the structure of the ground state wavefunction structure.

With the saddle-point system solved, the *in situ* measurement of this model system can be considered. Eq. (6.7) is used to calculate the phase $\theta(k, t_b, t_r)$ which maximizes the even-harmonic signal and eq. (6.9) is used to calculate variation of the even-harmonic intensity with the relative phase between the driving and perturbing fields. The same calculation for an equivalent system without a transition moment phase is used as a reference.

The resultant spectrogram depicting the normalized variation of the even-harmonic intensity with the relative phase between the driving and perturbing fields is shown in Fig. 6.3. The overlaid solid red line depicts the maximizing phase $\theta(k, t_b, t_r)$ calculated from the model argon atom while the dashed blue line shows the same result for a reference atom without a transition moment phase shift. A clear deviation from the reference result around 52 eV is observed in the result including the transition moment phase. Above and below the resonance, the two results agree. The trajectory excursion time from our model argon atom (dot-dash purple) agrees with the maximizing phase. This result indicates that *in situ* measurement is sensitive to the transition moment phase and agrees with recent experimental and theoretical work [40] reporting the *in situ* measurement of recollision in argon (see Chapter 8).

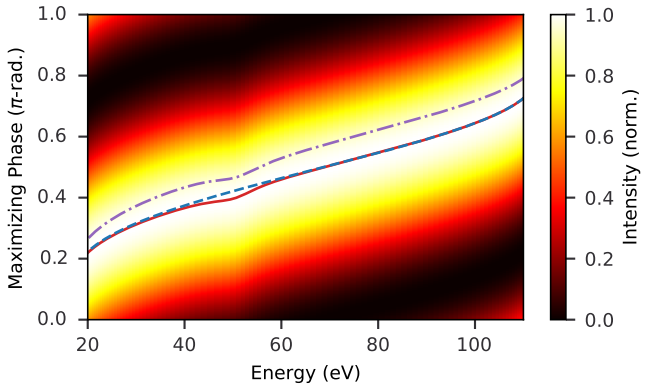

Figure 6.3 – The spectrogram showing variation of the even-harmonic intensity in an *in situ* measurement of the model argon atom with respect to the relative phase between the driving and perturbing fields. The overlaid solid red and dashed blue lines show the maximizing phase for the model argon and reference atoms, respectively. The overlaid purple dash-dotted line depicts the scaled excursion time as shown in Fig. 6.2.

6.3.2 Ionic Structure

I now address the apparent discrepancy between our results above, recent experimental and theoretical work in argon [40], and the study which demonstrated attosecond *in situ* measurement is insensitive to the transition moment phase shift associated with two-centre interference in a diatomic molecular system [9]. This study compared attosecond collinear $\omega-2\omega$ *in situ* measurement with RABBIT [32] and found that, while the RABBIT measurement is sensitive to the transition moment phase from two-centre interference, the effect of the phase shift was completely absent from the *in situ* measurement result. Here, I show that those results are consistent with this work and that the insensitivity of *in situ* measurement to two-centre interference phase shift is due to the quantum path interference nature of said phase shift.

In order to calculate recollision in diatomic molecules with the SFA, I use the formalism presented in [27] due to the agreement of the dipole phase with numerical TDSE simulation. For simplicity, I consider a one-dimensional diatomic molecule with atomic centres located at $x = \pm R/2$, where R is the internuclear separation. The atomic centres of ionization and recombination are labelled as $\alpha, \beta = 1, 2$, respectively, such that the positions of ionization and recombination are $(-1)^{\gamma} R/2$ with $\gamma = \alpha, \beta$. With this, there are four possible recollision trajectories corresponding to ionization from and recombination to each atomic centre. This is depicted in Fig. 6.4. The red (blue) trajectories correspond to those which ionize from and recombine to the same (opposite) atomic centres. Accordingly, the parameters for each trajectory are labelled with the subscript $\alpha\beta$. This analysis is straightforward to extend to more complex systems.

The ground state $\psi(x)$ is described using an even linear combination of atomic orbitals

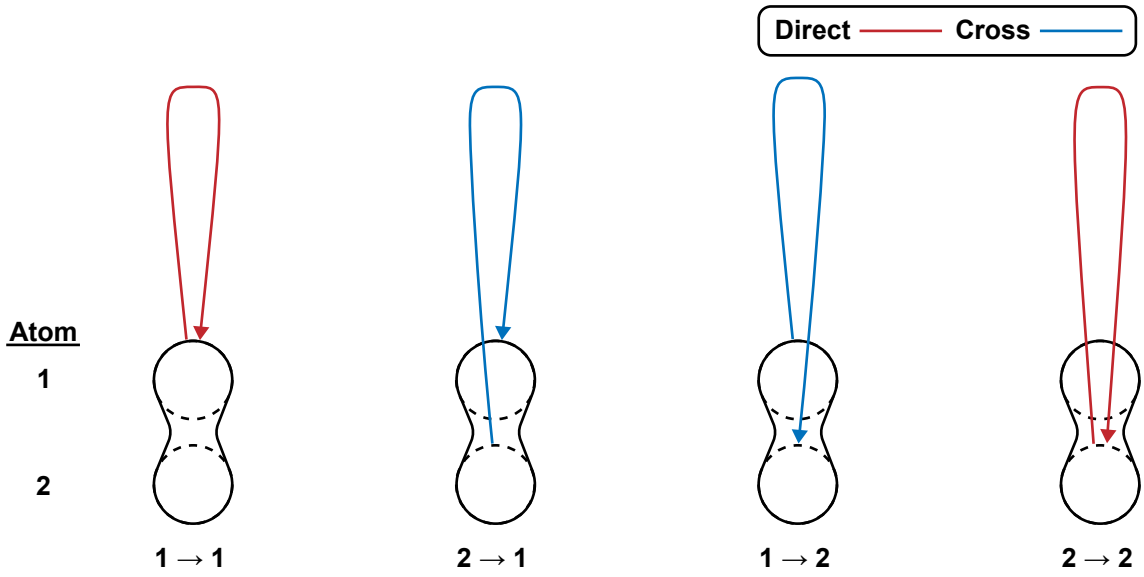

Figure 6.4 – In a diatomic molecule, there are four possible recollision trajectories. With the two atomic centres labelled as 1 and 2, trajectories can either ionize from and recombine to the same atomic centre (i.e. $1 \to 1$ and $2 \to 2$) as depicted in red, or ionize from and recombine to opposite atomic centres (i.e. $1 \to 2$ and $2 \to 1$), as depicted in blue.

centred at each atomic centre. The recombination and ionization matrix elements are, respectively, given as follows:

$$d_{rec}(k) = \mathcal{R}(k)\left(e^{ikR/2} + e^{-ikR/2}\right), \tag{6.10}$$

$$d_{ion}(k,t) = \mathcal{I}_1(k,t)e^{ikR/2} + \mathcal{I}_2(k,t)e^{-ikR/2}, \tag{6.11}$$

where $\mathcal{R}(k)$ and $\mathcal{I}_\alpha(k,t_b)$ denote the recombination and ionization matrix elements for the atomic orbital which makes up the ground state [27]. With these, the recollision dipole spectrum is represented as the sum of four terms, corresponding to each $\alpha\beta$ trajectory:

$$\tilde{D}(\Omega) = \sum_{\alpha,\beta=1}^{2} \int dk \int_{-\infty}^{\infty} dt_r \int_{-\infty}^{t_b} \mathcal{R}(P(t_r))\mathcal{I}_\alpha(P(t_b))e^{-i\left[S(k,t_b,t_r)+I_p(t_r-t_b)-\Omega t_r+\Phi_\alpha(P(t_b)-\Phi_\beta(P(t_r))\right]}, \tag{6.12}$$

where

$$\Phi_\gamma(k) = (-1)^\gamma k\frac{R}{2} \tag{6.13}$$

acts as an effective transition moment phase for the $\alpha\beta$ trajectory. From eq. (6.13), the

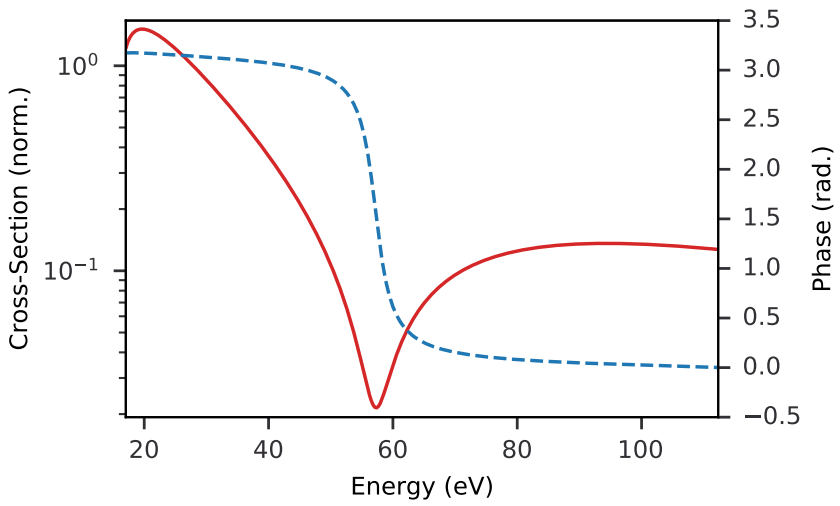

Figure 6.5 – The recombination cross-section and phase for a one-dimensional diatomic molecule with an internuclear separation of 1.8 a.u. and ionization potential of 15.8 eV calculated using eqs. (6.14-6.16) and the first-order approximation given in [27] using a sinusoidal driving field of wavelength 1.8 µm and peak intensity 1×10^{14} W/cm^2.

gradient of the transition moment phase $\Phi'_\gamma(k) = (-1)^\gamma R/2$ is a constant.

As demonstrated in [27], the corrections to the changes to the saddle-point solutions from a simple atomic system due to the transition moment phase in eq. (6.13) are small. I find the first-order Taylor expansion of the saddle-point eqs. (2.32 - 2.34) to first-order with respect to R, as in [27]. This expansion is performed about the saddle-point solutions for a system without a transition moment phase shift, $\bar{k}$, $\bar{t}_b$, and $\bar{t}_r$, which are labelled as the zeroth-order solutions. This results in the following corrections to the saddle-point solutions from the zeroth-order solution for each $\alpha\beta$ trajectory:

$$\Delta k^{(1)}_{\alpha\beta} = 0, \tag{6.14}$$

$$\Delta t^{(1)}_{b,\alpha} = \frac{(-1)^\alpha R}{2(\bar{k} + A(\bar{t}_b))}, \tag{6.15}$$

$$\Delta t^{(1)}_{r,\beta} = \frac{(-1)^\beta R}{2(\bar{k} + A(\bar{t}_r))}, \tag{6.16}$$

The dipole spectrum in eq. (6.12) can be expanded to first-order in R using these saddle-point corrections. The first-order recombination transition moment cross-section and phase calculated with this model using a 1.8 µm driving field of peak intensity 1×10^{14} W/cm^2 are shown in Fig. 6.5. Although it appears similar to the transition moment depicted in Fig. 6.1 for the model argon atom, the origin of the spectral minimum in each case differ. While the Cooper minimum is a result of the structure of the ground state wavefunction, the spectral

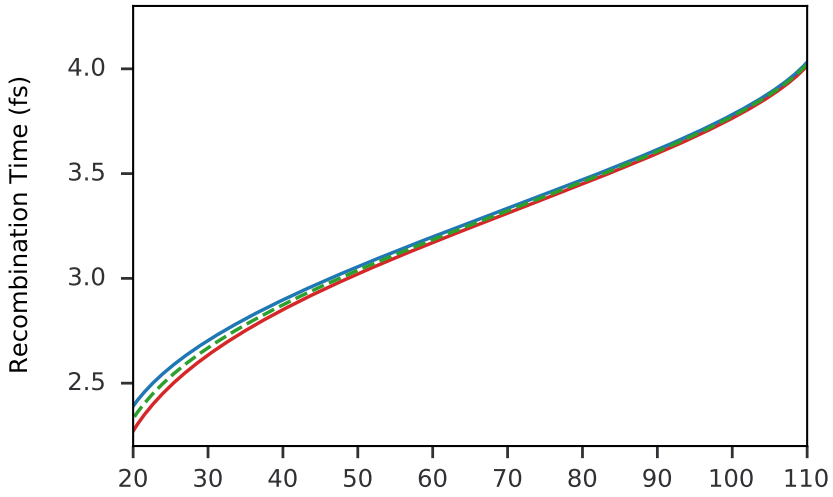

Figure 6.6 – The recombination times for trajectories recombining to the left and right atomic centres in a diatomic molecule of internuclear separation $R = 1.8$ a.u and ionization potential 15.8 eV are shown by the solid red and blue lines, respectively. The recombination times in a reference atom with an equivalent ionization potential is shown by the dashed green line.

minimum here results from the interference of the four possible $\alpha\beta$ trajectories.

From eqs. (6.14-6.16), it is apparent that the individual trajectories do not reflect the spectral structure of the transition moment phase in Fig. 6.5. This is demonstrated in Fig. 6.6, which shows the recombination times for trajectories with $\beta = 1, 2$ (red and blue solid lines, respectively) and the recombination time for the reference atomic system (dashed green). The correction to the recombination time corresponds to the time required for an electron of kinetic momentum $P(\bar{t}_r)$ to travel a distance of $(-1)^\beta R/2$ and varies adiabatically with the recollision electron energy.

I now consider an *in situ* measurement. Since $|\Delta t^{(1)}_{r,\beta}|/\bar{t}_r, |\Delta t^{(1)}_{b,\alpha}|/\bar{t}_b \ll 1$, I expand eq. (6.7) to first-order in $\Delta t^{(1)}_{r,\beta}$ and $\Delta t^{(1)}_{b,\alpha}$ for each $\alpha\beta$ trajectory. The perturbation-induced phase shift for the $\alpha\beta$ trajectory to first-order, $\sigma_{\alpha\beta}(k, t_b, t_r, \phi)$, is given as follows:

$$\begin{aligned}\sigma_{\alpha\beta}(k, t_b, t_r, \phi) = \sigma_0(\bar{k}, \bar{t}_b, \bar{t}_r, \phi) + A_p(\bar{t}_b)\Phi'_\alpha(P(\bar{t}_b)) - A_p(\bar{t}_r)\Phi'_\beta(P(\bar{t}_r)) \\ + \left(E_p(\bar{t}_r, \phi)\Phi'_\beta(P(\bar{t}_r)) + \frac{\partial \sigma_0}{\partial t_r}\bigg|_{\bar{k},\bar{t}_b,\bar{t}_r} + E(\bar{t}_r)A_p(\bar{t}_r, \phi)\Phi''_\beta(P(\bar{t}_r)) \right) \Delta t^{(1)}_{r,\beta} \\ - \left(E_p(\bar{t}_b, \phi)\Phi'_\alpha(P(\bar{t}_b)) + \frac{\partial \sigma_0}{\partial t_b}\bigg|_{\bar{k},\bar{t}_b,\bar{t}_r} + E(\bar{t}_b)A_p(\bar{t}_b, \phi)\Phi''_\alpha(P(\bar{t}_b)) \right) \Delta t^{(1)}_{b,\beta},\end{aligned} \tag{6.17}$$

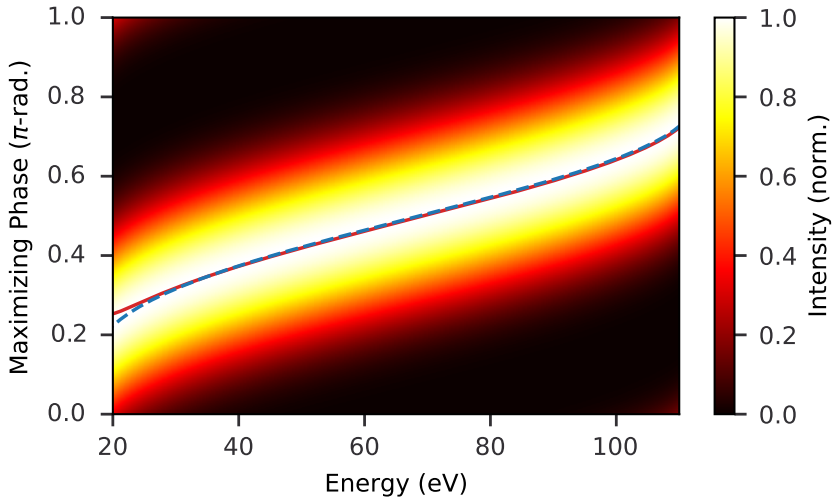

Figure 6.7 – The spectrogram showing the variation of the even-harmonic intensity in an *in situ* measurement in the two-centre system with respect to the relative phase between the driving and perturbing fields. The overlaid solid red and dashed blue lines show the maximizing phase for the diatomic molecule and reference atom, respectively. The driving field intensity and wavelength are 1×10^{14} W/cm^{-2}.

where I have solely retained terms which include the perturbing field. Within this first-order approximation, the influence of the perturbing field on the transition moment exactly cancels the change in $\sigma_0(k, t_b, t_r)$ due to $\Delta t^{(1)}_{b,\alpha}$ and $\Delta t^{(1)}_{r,\beta}$, since

$$\left.\frac{\partial \sigma_0}{\partial t_r}\right|_{\overline{k},\overline{t}_b,\overline{t}_r} \Delta t^{(1)}_{r,\beta} = A_p(\overline{t}_r, \phi)\Phi'_\beta(P(\overline{t}_r)), \tag{6.18}$$

$$\left.\frac{\partial \sigma_0}{\partial t_b}\right|_{\overline{k},\overline{t}_b,\overline{t}_r} \Delta t^{(1)}_{b,\alpha} = -A_p(\overline{t}_b, \phi)\Phi'_\alpha(P(\overline{t}_b)). \tag{6.19}$$

Further, the phase $\Phi_\gamma(k)$ varies linearly with respect to momentum and, therefore, $\Phi''_\gamma(k) = 0$. The total perturbation-induced phase shift is then given as follows:

$$\sigma_{\alpha\beta}(k, t_b, t_r, \phi) = \sigma_0(\overline{k}, \overline{t}_b, \overline{t}_r, \phi) + \frac{E_p(\overline{t}_r, \phi)}{\overline{k} + A(\overline{t}_r)}\frac{R^2}{4} - \frac{E_p(\overline{t}_b, \phi)}{\overline{k} + A(\overline{t}_b)}\frac{R^2}{4}. \tag{6.20}$$

The effective perturbation-induced phase shift is equal to the sum of that in a system without a transition moment phase and a term proportional to square of the distance of the displaced ionization and recombination atomic centres to the origin. Thus, all trajectories in a symmetric diatomic molecule exhibit the same perturbation-induced phase shift. Further, the change in the perturbation-induced phase shift is small, since $\omega_0, |\Delta t^{(1)}_{r,\beta}|/\overline{t}_r, |\Delta t^{(1)}_{b,\alpha}|/\overline{t}_b \ll 1$. Therefore, the results of an *in situ* measurement in a two-centre system and reference atomic

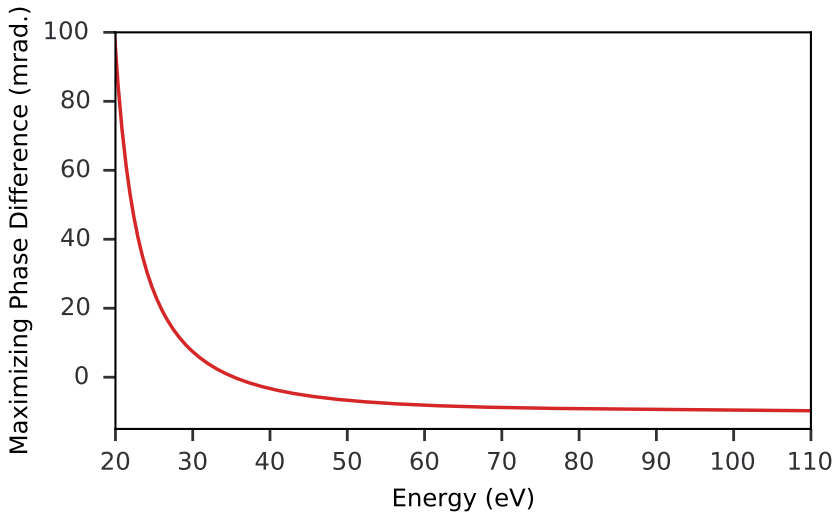

Figure 6.8 – The difference in the maximizing phase between the two-centre and reference atomic systems from the simulated *in situ* measurement in Fig. 6.7.

system will exhibit negligible differences. This is in contrast to the study of the Cooper minimum in argon, wherein the transition moment phase within a single trajectory is not a linear function of momentum and the large variation of the phase shift within a single recollision trajectory necessitates higher-order descriptions of the measurement.

The predicted *in situ* measurement result from this analysis is shown in Fig. 6.7, which depicts a spectrogram of the variation of the even-harmonic intensity with the relative phase between the driving and perturbing fields. The overlaid solid red and dashed blue lines depict the maximizing phase for the two-centre and an equivalent reference atomic system without a transition moment phase shift. The results for the diatomic molecule and reference atomic system are nearly identical, except at low energies, and the structure of the phase jump in Fig. 6.5 is completely absent. The difference in the maximizing phase for the two-centre and reference atomic systems is shown in Fig. 6.8. Like the change in recombination time due to ionic structure, the difference in maximizing phase between the two-centre and reference atom is largest at low energies and decreases monotonically with energy. Around the position of the minimum, this difference is less than 10 mrad and exhibits no features reflective of the spectral minimum.

This analysis is consistent with the findings of [9] and implies the nature of the transition moment phase is critical in determining the sensitivity of *in situ* measurement to recombination dynamics. This suggests that measurements of recollision in complex molecules using both *ex situ* and *in situ* measurement can be used to isolate spectral features of attosecond pulses due to ionic and electronic structure.

6.3.3 Shape Resonances

As observed in SF_6, shape resonances due to ionic structure can also significantly affect attosecond pulse emission [73]. *In situ* measurement, however, seems to be insensitive to these effects [72]. In such processes, the recollision electron is temporarily trapped in a quasi-bound state $|\xi\rangle$ due to the shape of the ionic potential.

This trapping is inherently a single-electron process and, assuming that the electron in the quasi-bound state is highly localized, can be described within the SFA as follows:

$$\tilde{D}(\Omega) = -i \int d\mathbf{k} \int_{-\infty}^{\infty} dt_r \int_{-\infty}^{t_r} dt_{sr} \int_{-\infty}^{t_{sr}} dt_b \; d^*_{0,\xi} d_\xi(k + A(t_{sr})) e^{-i[S(k,t_b,t_{sr}) - E_\xi(t_r - t_{sr}) + I_p(t_{sr} - t_b)]} \times E(t_b) d_0(k + A(t_b)) e^{i\Omega t_r}, \tag{6.21}$$

where t_{sr} is the time the electron is trapped into the quasi-bound state, E_ξ is the energy of the quasi-bound state, and ($\hat{v}$ is the ionic potential)

$$d_{0,sr} = \langle \psi_0 | z | \xi \rangle \,, \tag{6.22}$$

$$d_\xi = \langle \xi | \hat{v} | k + A(t_{sr}) \rangle \,. \tag{6.23}$$

The order of integration in eq. (6.21) can be re-ordered such that

$$\tilde{D}(\Omega) \propto -\frac{i}{\Gamma/2 - i(\Omega - E_{sr} + E_0)} \int_{-\infty}^{\infty} dt_{sr} \int_{-\infty}^{t_{sr}} dt_b d_{sr}(k + A(t_{sr})) e^{-i[S(k,t_b,t_{sr} + I_p(t_{sr} - t_b)]} \times E(t_b) d_0(k + A(t_b)) e^{i\Omega t_{sr}}. \tag{6.24}$$

This expression is equivalent to the conventional SFA dipole spectrum with a modulation in its amplitude and phase from the transition moment coupling the shape resonance to the ground state. Most importantly, the phase of the integrand is equivalent to that of the conventional SFA. Therefore, the SFA does not predict that *in situ* measurement is sensitive to the phase variation arising from the shape resonance in SF_6, in agreement with the findings of [72].

6.4 Conclusions

The sensitivity of attosecond *in situ* measurement to transition moment phase shifts can be explained by considering how the transition moment phase affects recollision trajectories. If the transition moment is real or its phase varies sufficiently slowly, then its effect on

recollision trajectories is negligible and it is the semi-classical action which dictates which trajectories dominate dipole emission. If, however, the transition moment is complex and rapidly varying, its phase can be as important in determining the stationary phase points as the semi-classical action. Since the ground state wavefunction cannot be varied, phase matching favours components of the recollision wave packet with a spectral phase which complements the transition moment phase. These results demonstrate that the effect of the perturbing field on the transition moment, which is typically neglected, must be included in the description of recollision in two-colour fields. This follows from the insensitivity of *in situ* measurement to the phase jump in the two-centre system, which results from a first-order cancellation of the change in the perturbation-induced phase shift due to the modified saddle-point solutions and the effect of the perturbing field on the transition moment.

Although the collinear $\omega - 2\omega$ *in situ* measurement was considered here, the findings are generally true for all forms of *in situ* measurement. This will be demonstrated for the single-image and non-collinear $\omega - 2\omega$ measurements in the subsequent chapters and follows from the perturbation-induced phase shift accounting for the transition moment phase shift in eq. (6.7).

This chapter focused on transition moment phase shifts describable with single-active electron descriptions of recollision. Chapters 7 and 9 will discuss transition moment phase shifts attributable to multielectron interaction in the one-dimensional helium atom and xenon, respectively. The results in Chapter 9 introduce an extension of the SFA which accounts for multielectron interaction and demonstrates the feasibility of using attosecond *in situ* measurement to characterize multielectron dynamics similarly to the results of this chapter.

Summary: The results of this chapter demonstrate that the sensitivity of all-optical measurement to transition moment phase shifts due to electronic structure is consistent with the insensitivity of these measurements to phase shifts arising from two-centre interference. The rest of this thesis will present both *ab initio* and experimental results which validate the results presented in this chapter.

Chapter 7

One-Dimensional TDSE Studies

Outline: This chapter presents results from a series of one-dimensional simulations investigating the sensitivity of attosecond *in situ* measurement to the transition moment phase in various systems.

The work presented in this chapter is based entirely on my own research and is included in one publication of mine [57].

This chapter presents results which help in understanding the sensitivity (and insensitivity) of *in situ* measurement to transition moment phase shifts using a series of one-dimensional TDSE simulations. Three prototypical one-dimensional cases are considered:

1. A simple atom with a flat recombination cross-section, which exhibits no significant transition moment phase shifts. This system will serve as a reference.
2. A two-centre system, which exhibits a spectral minimum and phase shift due to two-centre interference and ionic structure.
3. A two-electron one-dimensional helium atom, which exhibits doubly-excited bound states with energies above the single ionization threshold. The excitation of these states by the recollision electron produces Fano resonances in the attosecond pulse spectrum. The description of this system is outlined in Chapters 4 and 5.

This chapter serves as a *toy-model* summary of the main results of this thesis. I confirm the insensitivity of *in situ* measurement to the transition moment phase shift due to two-centre interference, but find higher-order effects do manifest in measurement under certain conditions. I then demonstrate the sensitivity of *in situ* measurement to multielectron interaction.

7.1 A Simple Atom

I first consider a one-dimensional simple atom in its ground state to serve as a reference. The one-dimensional atom is described using a soft-core Coulomb potential. The Hamiltonian, $\hat{\mathbf{H}}_{at}$ is given as follows:

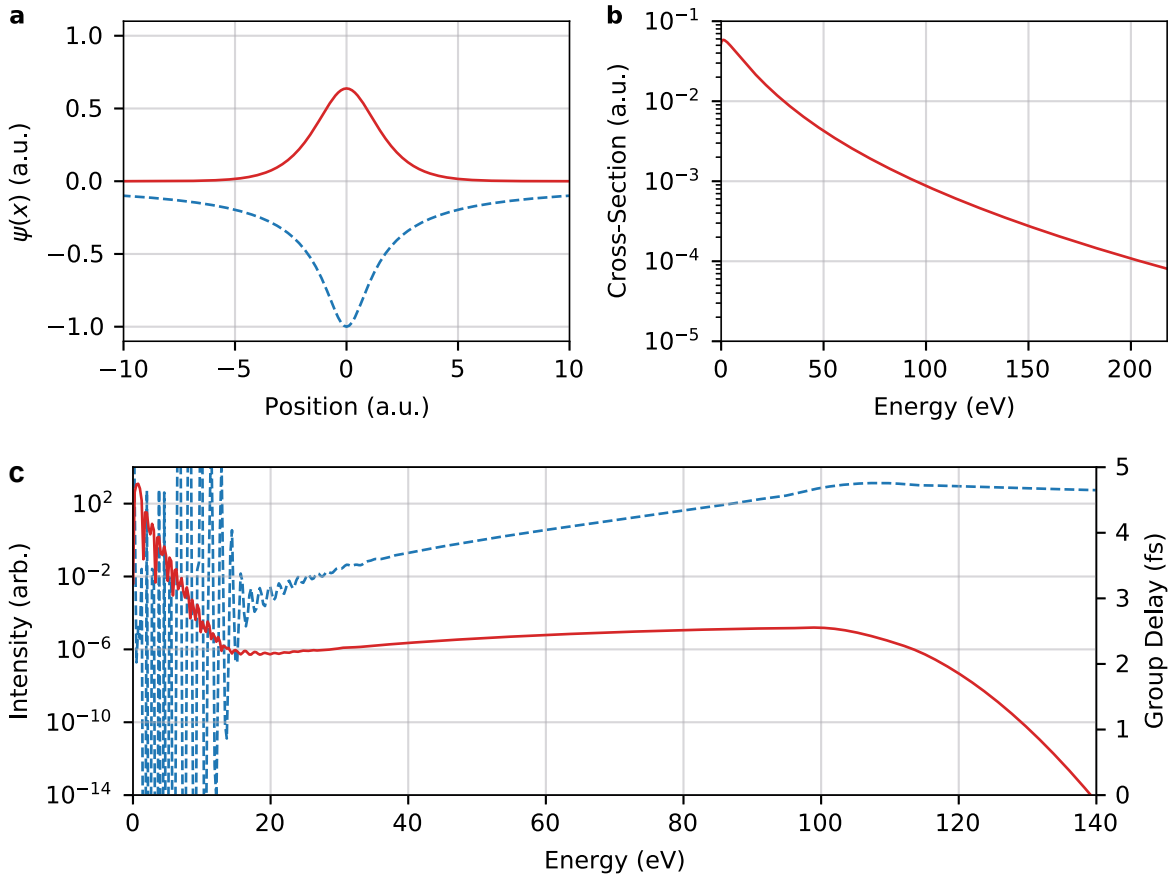

Figure 7.1 – (a) The ground state wavefunction (red) and potential (dashed blue) for a one-dimensional atom with a soft-core Coulomb potential. (b) The recombination cross-section for the simple atom as a function of continuum state energy. (c) The attosecond pulse spectral intensity (solid red) and group delay (dashed blue) generated in the one-dimensional simple atom with the Hamiltonian in eq. 7.1. The driving field is a 1.8 µm single-cycle sine-pulse of peak intensity 1×10^{14} W cm^{-2}.

$$\hat{\mathbf{H}}_{at} = -\frac{1}{2}\frac{\partial^2}{\partial x^2} - \frac{Z}{\sqrt{x^2+\alpha^2}}, \tag{7.1}$$

where $Z = 1$ and $\alpha = 1$. The system is described using a finite-difference approximation for the Laplacian operator using a uniform grid consisting of 1024 grid points with a spacing of $dx = 0.25$ a.u. The ground state wavefunction is found by directly diagonalizing the Hamiltonian and has an ionization potential of 18.24 eV. Fig. 7.1 (a) depicts the ground state wavefunction (solid red) and potential (dashed blue). The wavefunction resembles an s-state in a hydrogenic atom and does not exhibit any nodes. The absolute value of the dipole transition moment between the ground and continuum states is shown in Fig. 7.1 (b) as a function of continuum state energy. The transition moment is a monotonically decaying function of energy and exhibits no phase jumps.

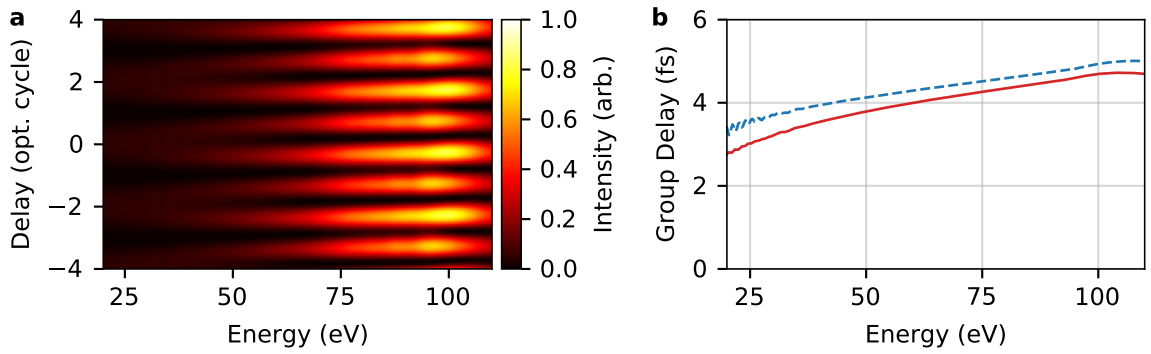

Figure 7.2 – (a) The single-image *in situ* spectrogram depicting the variation of the attosecond pulse spectrum from the one-dimensional atom with the effective delay between the driving and perturbing fields. (b) The group delay calculated from the unperturbed spectrum (dashed blue) and measured from the single-image spectrogram (solid red). The driving field is a single-cycle 1.8 µm sine-pulse of peak intensity 1×10^{14} W/cm^2.

For the time-dependent simulation, I use time step of $dt = 4$ as and time propagation is implemented using the Crank-Nicholson method. The driving field is a single-cycle 1.8 µm pulse with a peak intensity of 1×10^{14} W/cm^2. Transmission-free absorbing boundaries are used and begin at $|x_0| = 0.8 \times E_0/\omega_0^2 = 67$ a.u. The calculated attosecond pulse spectrum is shown in Fig. 7.1 (c) by the solid red line. The spectrum is smooth and relatively flat due to the absorption of the long trajectories. The group delay is shown by the dashed blue curve. Above the ionization threshold, the group delay increases linearly until the cutoff near 100 eV and resembles the recombination time as predicted by the SFA.

The single-image *in situ* measurement is calculated by including a same-colour perturbing field with a relative intensity of 10^{-4} and incident angle of 60 mrad with respect to the driving field. The non-collinear geometry is mapped to an effective temporal delay between the driving and perturbing fields given by eq. (3.29). Both beams are assumed to have uniform intensity profiles. The relative delay between the driving and perturbing fields is scanned over a range of 8 optical cycles of the driving field. The simulated *in situ* spectrogram is shown in Fig. 7.2 (a). The contour plot depicts the variation of the attosecond pulse intensity spectrum with respect to the effective delay between the driving and perturbing fields. Each energy component of the attosecond pulse spectrum modulates with respect to the delay and the phase of these modulations is proportional to the recollision electron wave packet group delay. Fig. 7.2 (b) shows the measured group delay (solid red) alongside the calculated group delay, as depicted in Fig. 7.1, and these results are in agreement.

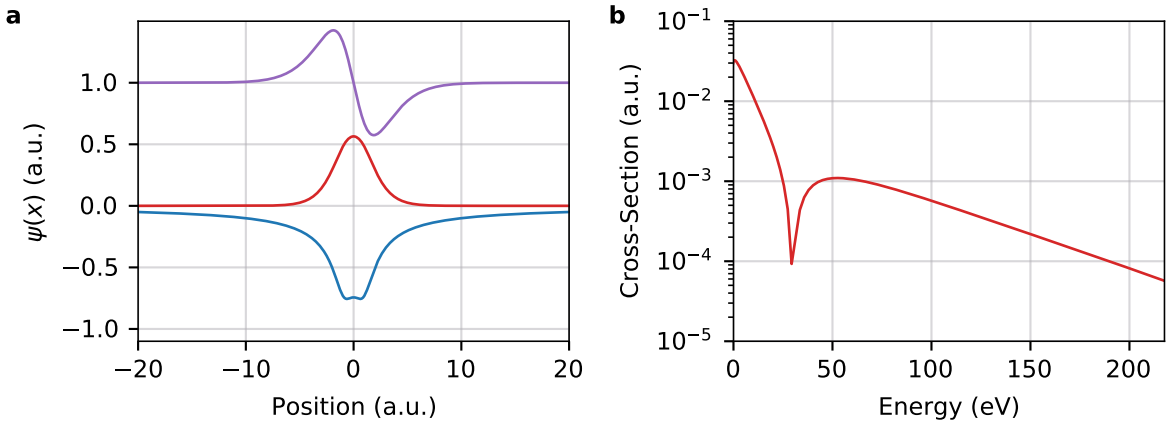

Figure 7.3 – (a) The ground state wavefunction (red), first excited state (purple and shifted for clarity) and potential (blue) for a one-dimensional molecule with a two-centre soft-core Coulomb potential. (b) The transition moment cross-section between the ground and continuum states as a function of continuum state energy. A sharp spectral minimum and phase shift (not shown) arises near 30 eV due to interference from the two molecular atomic centres.

7.2 Diatomic Molecule

I now consider photorecombination effects due to ionic structure and study a one-dimensional diatomic molecular system. From the results of Chapter 6 and [9], it is expected that *in situ* measurement is insensitive to the transition moment phase in two-centre systems. However, the conclusions of Chapter 6 result from a first-order analysis of the effect of the transition moment phase on recollision trajectories. Thus, it is expected that higher-order effects omitted from the analysis in Chapter 6 might manifest in a simulated *in situ* measurement in a two-centre system. Here, the single-image method used is designed for the characterization of isolated attosecond pulses. The continuum structure of the XUV spectra will allow for the observation of these higher-order effects. In contrast, the collinear $\omega - 2\omega$ *in situ* technique studied in [9] is restricted to photon energies which are even-harmonics of the driving field and, thus, is less sensitive narrow spectral features.

For the numerical simulation, I consider a two-centre Hamiltonian, $\hat{\mathbf{H}}_{2c}$, which consists of a pair of soft-core Coulomb potentials displaced from the origin by a distance $R/2$:

$$\hat{\mathbf{H}}_{2c} = -\frac{1}{2}\frac{\partial^2}{\partial x^2} - \frac{Z/2}{\sqrt{(x-R/2)^2+\alpha^2}} - \frac{Z/2}{\sqrt{(x+R/2)^2+\alpha^2}}, \tag{7.2}$$

where $Z = 1$, $\alpha = 1$, and $R = 1.8$ a.u, resulting in an ionization potential of 16.28 eV. The ground state (red), first excited state (purple), and potential (blue) are shown in Fig. 7.3 (a). The double-well structure of the potential results in a broadened ground state wavefunction and is the source of the spectral minimum and phase shift. Fig. 7.3 (b) shows the transition

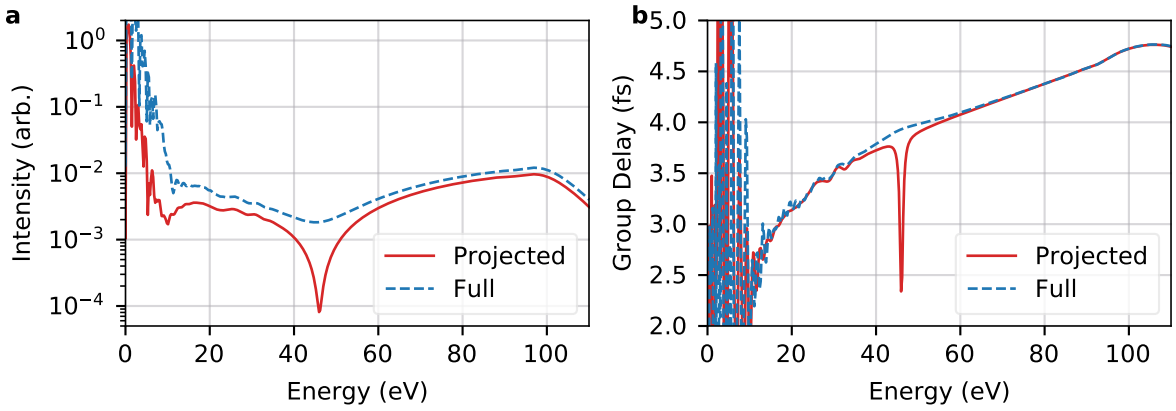

Figure 7.4 – (a) The attosecond pulse spectral intensity calculated in the two-centre system from the full (dashed blue) and projected (solid red) TDSE solutions. (b) The calculated group delay for the spectra in (a) with the same colour scheme. The driving field is a 1.8 µm single-cycle sine-pulse of peak intensity 1×10^{14} W cm^{-2}.

moment cross-section between the ground and continuum states as a function of continuum state energy. A sharp spectral minimum with an accompanying π-phase shift (not shown) is observed near 30 eV.

Motivated by the results of [9], I consider two cases: (1) a full solution of the TDSE (referred to as the full solution) and (2) a TDSE solution where the first excited state $|\phi_1\rangle$ is projected out of the electron wavefunction during time propagation (referred to as the projected solution). Projecting out the first excited state reduces field-induced orbital distortions of the bound state and results in sharper minimum and phase jump [27, 9]. This is achieved by applying the projection operator $\hat{\mathbf{P}}_1$,

$$\hat{\mathbf{P}}_1 = \hat{\mathbf{I}} - |\phi_1\rangle \langle\phi_1| \,, \tag{7.3}$$

and renormalizing the wavefunction after each time step. As in the previous section, I use a transmission-free absorbing boundary [5] in order to select only the short-trajectory components of the recollision dipole spectrum and use a single-cycle driving field of wavelength 1.8 µm with a peak intensity of 1×10^{14} W/cm^2.

The spectral intensity of the attosecond pulses generated from these two simulations is shown in Fig. 7.4 (a). The spectrum from the full solution (dashed blue) shows a broad and shallow spectral minimum centred around 45 eV, while the spectrum from the projected calculation exhibits a sharp spectral minimum. The group delay from these two calculations is shown in Fig. 7.4 (b). For the full solution (dashed blue), the group delay exhibits a broad positive deviation from the expected atto-chirp around the spectral minimum. The group delay from the projected solution exhibits a large negative variation around the spectral minimum.

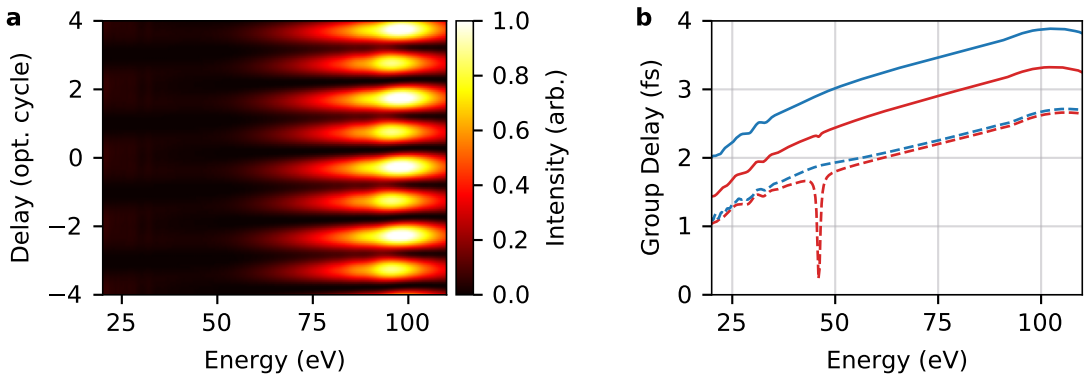

Figure 7.5 – (a) The single-image *in situ* spectrogram from the simulated measurement in the two-centre system depicting the variation of the projected attosecond pulse spectrum with the effective delay between the driving and perturbing fields. (b) The measured (solid) and calculated (dashed) group delay from the full (blue) and projected (red) TDSE solutions. The driving field was a single-cycle 1.8 µm sine-pulse of peak intensity 1×10^{14} W cm^{-2}.

The single-image *in situ* measurement is calculated as in the previous section. The resultant spectrogram from the projected simulation is shown in Fig. 7.5 (a) (the spectrogram from the full solution is not shown). The measured (solid lines) and calculated group delays (dashed lines) from each calculation are shown in Fig. 7.5 (b). The solid blue curve shows the modulation phase from the full TDSE simulated single-image measurement and the dashed blue curve shows the corresponding calculated group delay. While the variation in the group delay of the full solution around the spectral minimum is relatively smooth, it is clearly absent from the measurement result. The measurement is similar to the result obtained for the simple atom in Fig. 7.2.

The solid and dashed red curves show the measured and calculated group delay from the projected solutions, respectively. The measured group delay from projected TDSE solution exhibits a small deviation of -40 as from the reference atomic group delay around the spectral minimum, although this deviation is much smaller than the calculated group delay variation. As stated above, however, this deviation is expected since the insensitivity of *in situ* measurement to two-centre interference follows from a first-order analysis and this measurement technique characterizes isolated attosecond pulses with continuous spectra, permitting the measurement of narrow spectral features. Still, the size of the measured group delay variation is significantly smaller than the actual variation of the group delay. Given that the full TDSE solution measurement exhibited no signs of the transition moment phase shift and that projecting out the first excited state is not physical, these results validate the findings of Chapter 6 and [9] regarding *in situ* measurement and ionic structure in physical systems.

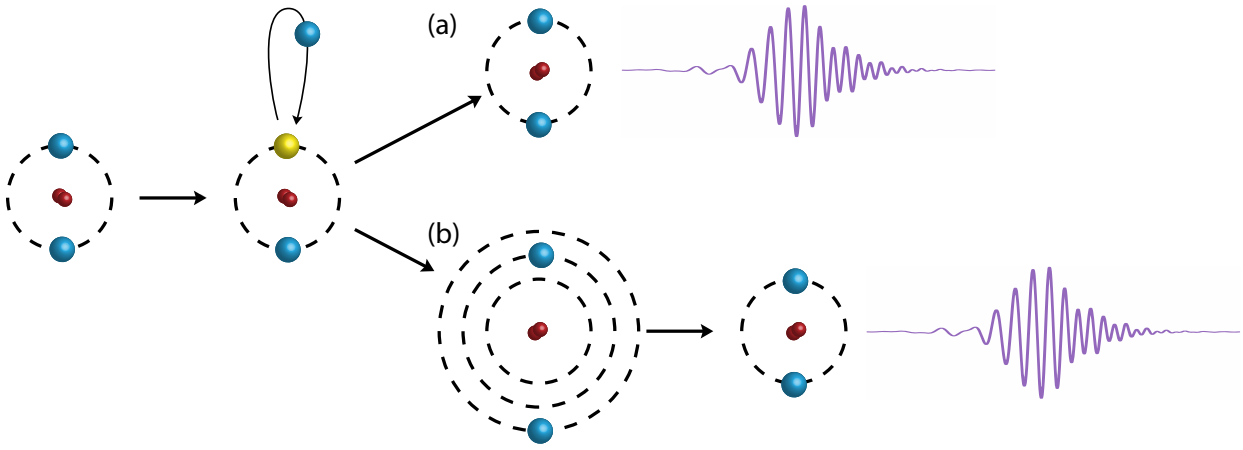

Figure 7.6 – The recollision process in the two-electron helium atom. The atom, initially in its ground state, undergoes single ionization through tunnelling due to a strong infrared field, leaving a hole (yellow) in the ion. In the continuum, the electron is accelerated by the strong field. The electron can then recombine and emit an XUV photon through two different pathways: (a) the electron can recombine directly to the ground state, (b) the electron can interact with the remaining bound electron, enter into a doubly excited state, and then recombine into the ground state. The interference of these two pathways gives rise to the characteristic asymmetric Fano line-shape in the dipole acceleration spectrum.

7.3 One-Dimensional Helium

Finally, I consider recollision in a two-electron system wherein Fano resonances due to recollision-induced double-excitation is observed. Fano resonances are a broad class of resonances that can occur during photoionization due to the excitation of a doubly excited state by multielectron interaction [74]. The interference between transitions from the ground state to a singly ionized continuum state and a degenerate doubly excited state results in an asymmetric absorption profile characteristic of Fano resonances.

The recollision process in this context can be described using a four-step model and is depicted in Fig. 7.6. The atom, initially in its ground state, undergoes tunnel ionization in response to a strong field. This promotes an electron to the continuum (blue circle), leaving a hole (yellow circle) in the ion. The electron in the continuum is then accelerated by the strong field. The electron can then recombine with its parent ion through two different pathways: (a) the electron can recombine directly to the hole from which it left and emit an XUV photon (referred to as the direct channel), or (b) the electron can interact with the remaining bound electron, after which the system enters into a doubly excited state (referred to as the correlated channel). This state then recombines to the ground state and emits an XUV photon.

Fano resonances in high harmonic generation have been theoretically predicted [75] and

observed experimentally [76]. Measurements of the spatial coherence of resonance-enhanced HHG suggest that the observed enhancements are due to the four-step recollision model depicted in Fig. 7.6 [77]. The one-dimensional nature of this helium model, however, overestimates the cross-section for multielectron interaction and the effects studied here may not be easily observed experimentally. Despite this, these simulations serve as a case study in order to demonstrate the sensitivity of *in situ* measurement to multielectron dynamics. The measurement of multielectron dynamics in realistic systems will be discussed in Chapters 8 and 9.

In order to understand recollision-induced Fano resonance excitation, it is useful to first discuss how Fano resonances arise during photoionization. I assume a two-electron system with ground state $|\psi_0\rangle$ and singly-ionized continuum states $|E\rangle$ of energy E. I assume that there exists a bound doubly excited state $|\xi\rangle$ with energy E_ξ which is degenerate with a single-ionized continuum state. The system for continuum state energies near the resonance can be described through the Hamiltonian $\hat{\mathbf{H}}$ as follows [78]:

$$\langle \xi | \hat{\mathbf{H}} | \xi \rangle = E_\xi, \tag{7.4}$$

$$\langle E | \hat{\mathbf{H}} | E' \rangle = E\delta(E - E'), \tag{7.5}$$

$$\langle E | \hat{\mathbf{H}} | \xi \rangle = V, \tag{7.6}$$

where I assume that V is a constant. As Fano found for photoionization [74], the shape of the absorption spectrum, $P(E)$, around such a resonance in helium can be described using these states as

$$P(E) = \frac{|\epsilon + q|^2}{1 + \epsilon^2}, \tag{7.7}$$

where

$$\epsilon = \frac{E - E_r}{\Gamma/2}, \tag{7.8}$$

$$\Gamma = 2\pi V^2, \tag{7.9}$$

$$q = \frac{\langle \xi | \hat{d} | \psi_0 \rangle}{\pi V \langle E | \hat{d} | \psi_0 \rangle}. \tag{7.10}$$

and $\hat{d}$ is the dipole operator. Fano resonances exhibit a characteristic asymmetric profile and this asymmetry is determined through the parameter q, which is related to the ratio of the transitions directly to the continuum and to the continuum through the doubly-excited state.

Recollision-induced Fano resonance excitation can be understood using an extension of the SFA which accounts for the excitation of a doubly-excited state as an additional intermediary step within the three-step model. This model is similar to a model describing photoionization of helium by an XUV pulse in the presence of an infrared field used to study

attosecond streaking [79]. I assume that the atom begins in its ground state $|\psi_0\rangle$ which has an ionization potential I_p. The total dipole moment at time t_r is described as the sum of the direct, $d_d(t_r)$ (as described in Chapter 2), and correlated, $d_c(t_r)$, channels:

$$d_d(t_r) = \int d\mathbf{k} \int dt_b \, \langle\psi_0| \, \hat{\mathbf{r}} \, |\mathbf{k} + \mathbf{A}(t_r)\rangle \, e^{-i[S(\mathbf{k},t_b,t_r)+I_p(t_r-t_b)]} \, \langle \mathbf{k} + \mathbf{A}(t_b)| \, \mathbf{F}(t_b) \cdot \hat{\mathbf{r}} \, |\psi_0\rangle \, , \quad (7.11)$$

$$\begin{aligned} d_c(t_r) = &\int d\mathbf{k} \int dt_{ee} \int dt_b \, \langle\psi_0|\hat{\mathbf{r}}|\xi\rangle \, \langle\xi| \, \hat{\mathbf{U}}_F(t_{ee}, t_r) \, |\xi\rangle \, \langle\xi| \, \hat{\mathbf{H}} \, |\mathbf{k} + \mathbf{A}(t_{ee})\rangle \, |\psi_d\rangle \\ &\times e^{i[S(\mathbf{k},t_b,t_{ee})+I_p(t_{ee}-t_b)]} \, \langle\psi_d| \, \langle \mathbf{k} + \mathbf{A}(t_b)|\mathbf{F}(t_b) \cdot \hat{\mathbf{r}}|\psi_0\rangle \, , \end{aligned} \quad (7.12)$$

where $\mathbf{k}$ is the canonical momentum of the recollision electron, t_b is the time of ionization, t_{ee} is the time of double excitation, $\mathbf{F}(t_b)$ is the electric field at time t_b, $|\mathbf{k}\rangle \, |\psi_d\rangle$ describes the state of the continuum electron of momentum $\mathbf{k}$ and ion after ionization, and $\hat{\mathbf{U}}_F(t, t')$ describes the evolution of the doubly-excited state between times t and t'. The operator $\hat{\mathbf{U}}_F(t, t')$ has the following form [79]:

$$\hat{\mathbf{U}}_F(t, t') = \exp\left[-i \int_t^{t'} d\tau \left(\hat{\mathbf{H}} + |\xi\rangle \, \Delta E_S(\tau) \, \langle\xi|\right)\right] \quad (7.13)$$

and $\Delta E_S(\tau)$ describes the dynamical Stark shift. From eq. (7.12), the correlated recollision process as depicted in Fig. 7.6 is clear. An electron first tunnels into the continuum, is accelerated by the field, and the system then enters into the doubly-excited state through configuration interaction. This doubly-excited state then evolves under the influence of the external field until it recombines to the ground state. The interference of the direct and correlated channels will be shown below to give rise to asymmetric resonance profiles characteristic of Fano resonances in the dipole acceleration spectrum.

The influence of the single-cycle driving and perturbing fields is described using the dynamical Stark shift calculated by approximating an electron in the doubly-excited state as asymptotically free [80]. Such a description has been demonstrated to accurately describe the photoionization of helium in the presence of an infrared field with intensities up to 10^{13} W/cm^2 and a pulse duration of 7 fs [81]. In that work, the infrared field was observed to impart a controllable phase shift proportional to the infrared pulse intensity onto the doubly excited state during its evolution, resulting in a periodic modulation of the asymmetry of the Fano resonance shape. I proceed similarly here. Including the relative phase between the driving and perturbing fields, ϕ, and treating the asymptotically free electron semi-classically, the dynamical Stark shift can be described through the following:

$$\begin{aligned} \Delta E(t, \phi) &= \frac{1}{2} \left(\mathbf{A}(t) + \mathbf{A}_p(t, \phi)\right)^2 \\ &\approx \frac{1}{2} A^2(t) + A(t) A_p(t, \phi) + \mathcal{O}\left(\eta^2\right) \\ &= \Delta E_0(t) + \delta E_p(t, \phi), \end{aligned} \quad (7.14)$$

where

$$\Delta E_0(t) = \frac{1}{2}A^2(t), \tag{7.15}$$

$$\delta E_p(t,\phi) = A(t)A_p(t,\phi). \tag{7.16}$$

From eq. (7.14 - 7.16), the influence of the driving and perturbing fields on the doubly-excited state is composed of two components. The first, $\Delta E_0(t)$, involves only the driving field and contributes to the shape of the resonance as observed through unperturbed recollision. In simulations, varying the driving field intensity was observed to modulate the asymmetry of the Fano resonances within the attosecond pulse spectra similarly to the behaviour observed in [80, 81].

The second component, $\delta E_p(t)$, involves the perturbing field and can be controlled. This control will permit the observation of the evolution of doubly excited states in the presence of strong fields. This is made explicit by including this approximate dynamical Stark shift into the propagator $\hat{\mathbf{U}}_F(t_{ee}, t_r)$:

$$\hat{\mathbf{U}}_F(t_{ee}, t_r) \approx \exp\left[-iE_\xi(t_r - t_{ee}) + \int_{t_{ee}}^{t_r} \Delta E_0(\tau)d\tau + \sigma_\xi(t_{ee}, t_r, \phi)\right], \tag{7.17}$$

where

$$\sigma_\xi(t_{ee}, t_r, \phi) = \int_{t_{ee}}^{t_r} A(\tau)A_p(\tau,\phi)d\tau. \tag{7.18}$$

This along with the change in the semi-classical action due to the perturbing field (as described in eq. (3.13)) yields the total perturbation-induced phase shift:

$$\sigma(k, t_b, t_{ee}, t_r, \phi) = \int_{t_b}^{t_{ee}} [k + A_p(\tau)] \cdot A_p(\tau,\phi)d\tau + \int_{t_{ee}}^{t_r} A(\tau)A_p(\tau,\phi)d\tau. \tag{7.19}$$

Thus, the influence of the perturbing field results in a controllable phase shift, through which the evolution of the doubly excited state can be monitored.

The effect of recollision-induced double excitation on the attosecond pulse spectrum is depicted in Fig. 7.7, which depicts the total attosecond pulse spectrum generated by a single-cycle 800 nm driving field of peak intensity 2.5×10^{14} W/cm^2 on the left axis. For these calculations, I use the one-dimensional helium model as described in Chapters 4 and 5 and propagate over a range of 128 fs. The spectrum exhibits a typical plateau structure until the cutoff at 71 eV. Prominent variations in the spectral intensity are observed between 50 and 55 eV, 60 and 65 eV, and near 68 eV. These variations exhibit the characteristic asymmetric Fano-resonance shape and their energies agree with studies of photoionization dynamics in the one-dimensional helium atom [82]. The group delay (blue) plotted on the

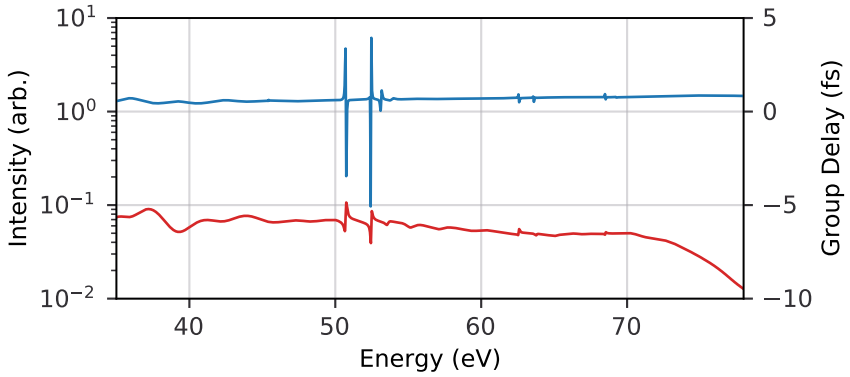

Figure 7.7 – The attosecond pulse spectral intensity (red) and group delay (blue) from the one-dimensional helium atom. Prominent variations in the spectral intensity and group delay are observed between 50 and 55 eV, 60 and 65 eV, and near 68 eV. A single-cycle 800 nm driving field with a peak intensity of 2.75×10^{14} W/cm^2 was used.

right is predominantly linear through the spectrum, however significant variations in the group delay are observed around each Fano resonance. In particular, huge variations are observed around the resonances near 50 eV. The size of these variations is related to the length of the temporal window of the simulation and the omission of decay within the TDSE formalism.

The single-image *in situ* spectrogram for the one-dimensional helium simulation is shown in Fig. 7.8 for energies between 50 and 85 eV, in order to focus on the Fano resonances. The modulation phase for each frequency is shown by the overlaid blue line and is typically related to the recollision electron group delay. The modulation phase varies smoothly below the cutoff, after which it is nearly constant. Around each Fano resonance, however, significant modulations in the measured group delay are observed. The size of the modulations around each resonances are smaller than those observed in the calculated group delay. This is because the perturbing field as a probe spans only eight optical cycles and its influence is proportional to the driving field amplitude. While the evolution of the excited state after the driving and perturbing pulses contributes to the total calculated dipole emission and group delay, the evolution of the system is only measured within the range of time scanned by the perturbing pulse for which the driving field amplitude is appreciable.

7.4 Conclusions

In this chapter, I demonstrated that, while attosecond *in situ* measurement is predominantly insensitive to the transition moment phase shift from two-centre interference in a diatomic molecule, the effects of two-centre interference can manifest when the first excited state is projected out of the time-dependent wavefunction. This was motivated by the results of [9], which reported that *in situ* measurement was insensitive to two-centre interference

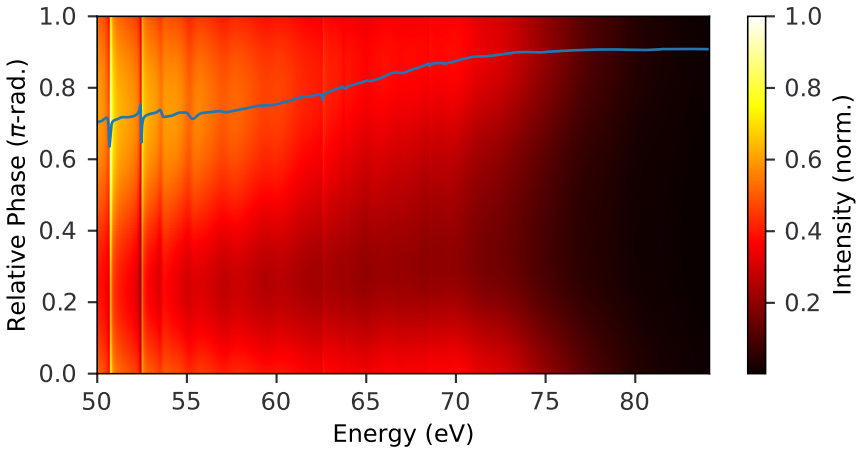

Figure 7.8 – The single-image *in situ* spectrogram from the simulated measurement in one-dimensional helium. The blue overlaid line shows the phase of the modulation with the relative phase between the driving and perturbing fields for each spectral component of the pulse. Although the modulation phase is roughly linear until the cutoff near 71 eV, variations are observed around each Fano resonance. The driving field is a single-cycle 800 nm pulse with peak intensity 2.5×10^{14} W/cm^2 and the perturbing field has a relative intensity of 10^{-4}.

using simulations of HHG-based *in situ* measurement while projecting out the first excited state. The sensitivity observed here was possible due to the use of a measurement technique designed for the measurement of isolated attosecond pulses, permitting a continuous measurement across the attosecond pulse spectrum. Although the projection of the first excited state is unphysical, the results confirm that the effect of two-centre interference on the recollision electron wave packet is small, as discussed in Chapter 6, but not zero. With regards to possible experiments, however, these results confirm that attosecond *in situ* measurement are insensitive to realistic phase shifts due to two-centre interference in physical systems.

Further, using the simplest multielectron model that can be solved exactly using numerical methods, I have shown how multielectron effects influence attosecond pulse generation and confirmed that *in situ* measurement is sensitive to these dynamics. The one-dimensional helium model serves as a prototype for the study of these dynamics in physical systems [8, 83], which are the subjects of the next two chapters.

Summary: In this chapter, the sensitivity of attosecond *in situ* measurement to ionic structure and multielectron interaction were investigated in prototypical one-dimensional systems. The measurement of transition moment phase shifts due to electronic structure and multielectron interaction in physically realistic systems is the subject of the next two chapters.

Chapter 8

The Cooper Minimum in Argon

Outline: The importance of multi-electron effects in shaping the Cooper minimum is presented. Then, the *in situ* measurement of the transition moment phase shift around the Cooper minimum in argon is demonstrated both theoretically and experimentally.

The theoretical work presented in this chapter is based entirely on my own research. The experimental data presented was collected by C. Zhang. I developed the program used for analysis and developed the interpretation of the experimental data. All work presented here is from one publication of mine [40].

8.1 Origin of the Cooper Minimum in Argon

Cooper minima are ubiquitous in photoionization spectra from atoms and molecules [71]. The dipole transition matrix element coupling continuum states to a ground state wavefunction exhibiting a radial node passes through zero, leading to a spectral minimum and corresponding phase jump in photoionization spectra. The rapid phase variation across a Cooper minimum gives rise to significant photoionization time delays which have been measured using attosecond *ex situ* methods [84]. As the inverse process of photoionization [24], photorecombination also exhibits Cooper minima, most notably in high harmonic generation (HHG) [85, 86]. The spectral phase of attosecond pulses generated by recollision in such media are significantly shaped by phase shifts around Cooper minima [7].

In order to understand the origin of the Cooper minimum, it is useful to first consider a single-active electron (SAE) description of the transition moment. I consider an initial state, $\left|\psi_{3p_{m_0}}\right\rangle$, where the subscript denotes the quantum numbers n, l, and m, respectively, interacting with an electric field polarized along $\hat{\mathbf{z}}$. The transition moment coupling the initial state to a continuum state $|\Psi_{\mathbf{k},l}\rangle$ along a direction $\hat{\mathbf{z}}$ is given as follows:

$$d_{\mathbf{k},l}\left(\Omega\right) = \langle \Psi_i | \mathbf{r} \cdot \hat{\mathbf{z}} | \psi_{\mathbf{k},l} \rangle \, . \tag{8.1}$$

As in Chapter 5, I describe $\langle \mathbf{x}|\psi_{3p_m}\rangle$ and the continuum state as the product of a radial component, $R_{nl}(r)$, and an angular component described through spherical harmonics, $Y_{l,m}(\theta,\phi)$, such that

$$\langle \mathbf{x}|\psi_{3p_{m_0}}\rangle = \psi_{3p_{m_0}}(r,\theta,\phi) = R_{nl}(r)Y_{l,m_0}(\theta,\phi). \tag{8.2}$$

Since the argon ground state is spherically symmetric, I consider a spherically symmetric effective potential, $v_{tot}(r)$, describing the interaction of the $3p_{m_0}$ electron with the ion. Accordingly, the continuum wavefunction $\psi_{\mathbf{k},l}(\mathbf{r})$ of momentum $\mathbf{k}$ and angular momentum l must satisfy the Schrödinger equation:

$$\left\{-\frac{\Delta}{2} + v_{tot}(r) - \frac{k^2}{2}\right\}\psi_{\mathbf{k},l}(\mathbf{r}) = 0. \tag{8.3}$$

The scattering wavefunction found from eq. (8.3) can be expressed as follows:

$$\psi_{\mathbf{k}}(\mathbf{r}) = \frac{1}{\sqrt{k}}\sum_{l=0}^{\infty}\sum_{m=-l}^{l} i^l e^{-i(\sigma_l+\delta_l)} R_{k,l}(r)Y_{l,m}(\Omega_{\mathbf{r}})Y^*_{l,m}(\Omega_{\mathbf{k}}), \tag{8.4}$$

where Ω_j is the solid-angle in j-space. The phase components, σ_l and δ_l, are the Coulomb and short range scattering phase shifts, respectively. Within this approximation, the transition moment in eq. (8.1) is the following:

$$\langle \psi_{3p_{m_0}}|\hat{\mathbf{z}}|\psi_{\mathbf{k}}\rangle = \frac{1}{\sqrt{k}}\sum_{l=0}^{\infty}\sum_{m=-l}^{l} i^l e^{i(\sigma_l+\delta_l)} \langle R_{31}|r|R_{\mathbf{k},l}\rangle \langle Y_{1,m_0}|\cos\theta|Y_{l,m}\rangle Y^*_{l,m}(\Omega_{\mathbf{k}}). \tag{8.5}$$

Since

$$\cos(\theta) = \sqrt{\frac{4\pi}{3}}Y_{1,0}(\theta,\phi), \tag{8.6}$$

the angular component of eq. (8.5) yields contributions solely from $l = 0, 2$:

$$\begin{aligned}\langle Y_{l_0,m_0}|\cos(\theta)|Y_{l,m}\rangle &= \sqrt{\frac{(2l_0+1)(3)(2l+1)}{4\pi}}\begin{pmatrix} l_0 & 1 & l \\ 0 & 0 & 0\end{pmatrix}\begin{pmatrix} l_0 & 1 & l \\ m_0 & 0 & m\end{pmatrix} \\ &= \begin{cases}\sqrt{\frac{l_0^2-m_0^2}{(2l_0+1)(2l_0-1)}} & l = 0 \\ \sqrt{\frac{(l_0+1)^2-m_0^2}{(2l_0+3)(2l_0+1)}} & l = 2\end{cases}.\end{aligned} \tag{8.7}$$

With this, the transition moment for the $3p_0$ orbital is

$$\langle \psi_{3p_0}|\hat{\mathbf{z}}|\psi_{\mathbf{k}}\rangle = \frac{1}{\sqrt{3\pi k}}\left(e^{i(\sigma_0+\delta_0)}\frac{\langle R_{31}|r|R_{\mathbf{k},0}\rangle}{2} - e^{i(\delta_2+\sigma_2)}\langle R_{31}|r|R_{\mathbf{k},2}\rangle\right). \tag{8.8}$$

The radial integrals in eq. (8.8) can be calculated using the orbital radial wavefunctions

nl^g	ϵ_{DFT} (eV)	ϵ_{exp} (eV)	$\Delta\epsilon$ (%)
$1s^2$	-3159.46	-3205.9	1.46
$2s^2$	-311.96	-326.3	4.49
$2p^6$	-247.37	-250.6 (-248.4)	1.30 (42)
$3s^2$	-29.37	-29.3	0.24
$3p^6$	-15.80	-15.7 (-15.9)	0.63 (0.63)

Table 8.1 – The energies for the electron orbitals in argon calculated using density-functional theory and experiment [87] labelled by the principle and orbital angular momentum quantum numbers, n and l, with their occupancy number g. The percent difference between the calculation and experiment are shown on the right. The density-functional theory calculation is performed using the LB94 exchange-correlation functional.

found from *ab initio* calculations. In order to describe the argon atom, I use DFT with the LB94 approximation for the exchange-correlation potential, as described in Chapters 4 and 5. The calculated Kohn-Sham orbital energies are shown in Table 8.1 alongside the experimentally measured electron orbital energies [87]. Despite the omission of relativistic effects, which are significant in describing deeply bound core electrons, the energies of the valence-shell Kohn-Sham orbitals agree with experiment, with the difference in the calculated and experimental orbital energies for the $n = 3$ shell ranging between 0.20 and 0.63 %.

The $3p_0$ orbital is depicted in Fig. 8.1. Figures 8.1 (a) and (b) depict a contour and radial plot of the $3p_0$ orbital wavefunction, respectively. The $3p_0$ radial wavefunction exhibits a node at $r = 0.8$ a.u. and this imprints a spectral minimum and corresponding π-phase shift onto the $\langle R_{31}|r|R_{\mathbf{k}2}\rangle$ transition moment known as the Cooper minimum. This is depicted by the red curve in Fig. 8.1 (c), which shows the cross-section $|\langle R_{31}|r|R_{\mathbf{k},2}\rangle|$ as a function of continuum state energy. Typically, the $nl \rightarrow \epsilon(l-1)$ transition moment, describing the s-wave channel here, does not exhibit spectral minima [88]. The transition moment cross-section $|\langle R_{31}|r|R_{\mathbf{k}0}\rangle|$ is depicted in Fig. 8.1 (c) by the blue curve. Although it does not exhibit a spectral minimum, its behaviour is significant in shaping the transition moment phase shift across the Cooper minimum [7].

As described with the SFA in Chapter 6 , the spectral minimum in the transition moment is imprinted onto attosecond pulses generated in argon. The spectral intensity of an attosecond pulse generated in argon calculated using TD-DFT model described in Chapters 4 and 5 is depicted in Fig. 8.2 on the left axis by the solid red curve. The driving field is a single-cycle 1.8 µm pulse with a peak intensity of 1×10^{14} W/cm^2 and absorbing boundaries [5] are used in order to select only short trajectory contributions to the dipole spectrum. The spectrum exhibits a sharp spectral minimum centred near 52 eV. The dashed blue curve depicts the group delay of the spectrum and is predominantly linear throughout the spectrum until the cutoff near 105 eV. The group delay, however, exhibits a negative variation around the Cooper minimum due to the transition moment phase shift. Although Cooper minima are typically described as single-electron phenomena, multielectron interactions are

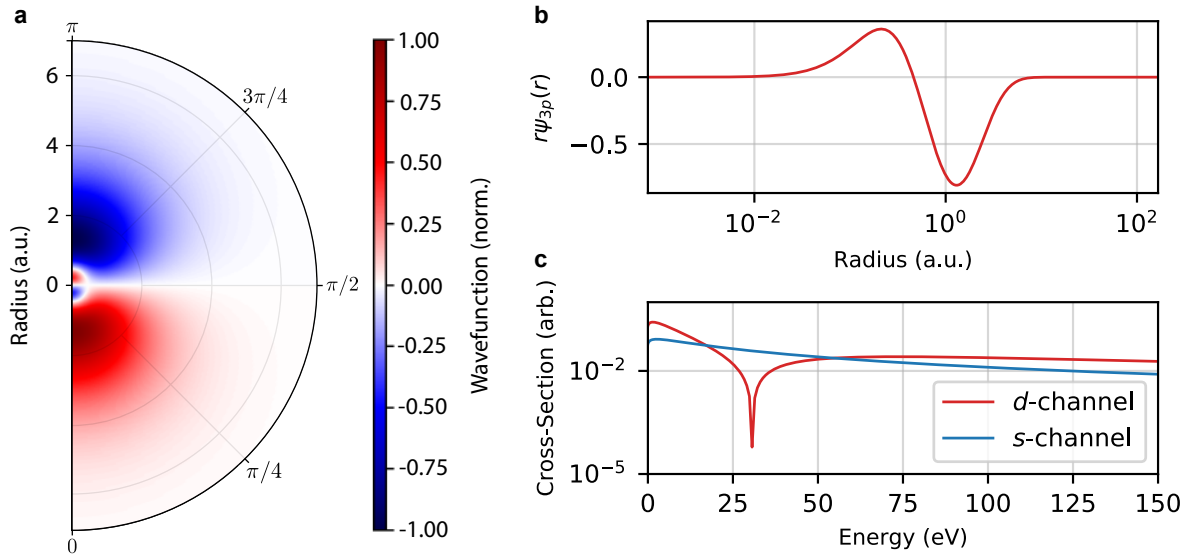

Figure 8.1 – (a) Contour and (b) radial plot of the $3p_0$ Kohn-Sham orbital wavefunction calculated using DFT with the LB94 functional [54]. (c) The transition moment cross-section between the d-wave (red) and s-wave (blue) continuum states and the ground state as a function of continuum state energy.

significant in shaping the observed shape and phase of the minimum. The importance of multielectron dynamics in shaping the Cooper minimum is the subject of the next section.

8.1.1 Multielectron Shaping of the Cooper Minimum

Although the single-active electron description of the Cooper minimum in argon is commonly used [24], recent work has demonstrated the importance of multi-channel and multi-electron effects in the shaping of the Cooper minimum [89]. Even SAE potentials derived from multielectron *ab initio* calculations (e.g. the Muller potential [90]), for which the ground state accounts for multielectron effects, predict the Cooper minimum in photorecombination to be at a lower energy than experimentally observed and shallower in depth [24].

The attosecond pulse spectra generated in argon due to a single-cycle 1.8 µm pulse of peak intensity 1×10^{14} W/cm^2 including various levels of multielectron interaction are shown in Fig. 8.3. The level of multielectron interaction is controlled by freezing the multielectron potential (scaled $\times 1000$, red) and through the maximum multipolar expansion order, $L_H = 0$ (scaled $\times 100$, blue), 1 (scaled $\times 10$, purple), and 2 (green) of the Hartree potential, as described in Chapter 5.

The spectra including frozen and monopole multielectron interaction (i.e. $L_H = 0$) exhibit a the Cooper minimum which is shallower, wider, and at a lower energy ($\sim$ 41 eV) than observed in experiment [40] and is similar in shape to the spectrum generated using single-active electron approximations [90, 24]. The position of the spectral minimum does

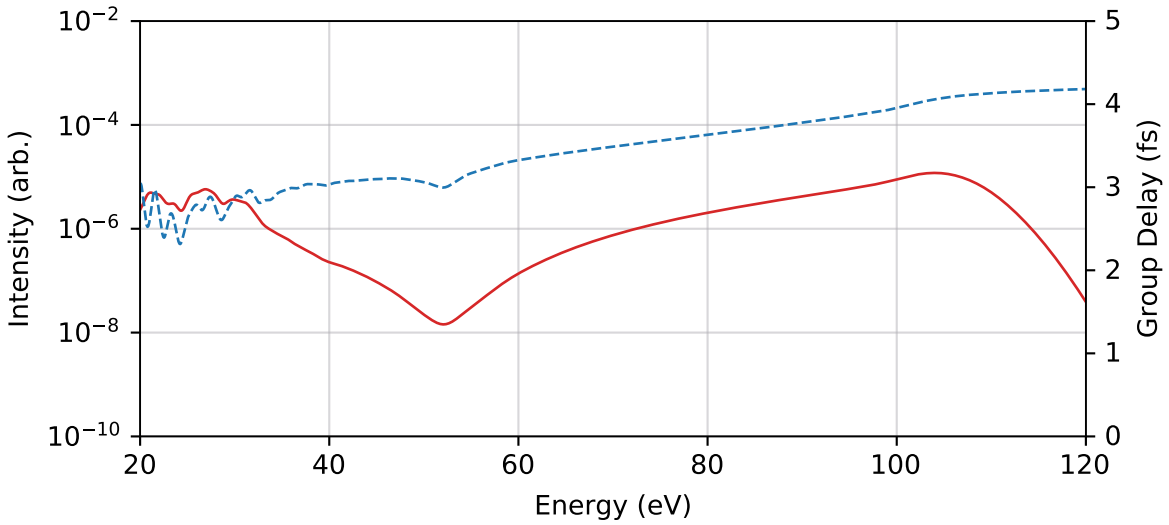

Figure 8.2 – Attosecond pulse spectrum from argon calculated using the TD-DFT model described in Chapter 5. The driving field is a single-cycle 1.8 µm pulse of peak intensity 1×10^{14} W/cm^2 and the maximum Hartree potential multipolar expansion level of $L_H = 2$.

not change significantly for these cases.

In contrast, the spectral minimum from the $L_h = 1$ and 2 simulations are considerably deeper and narrower compared with the frozen and $L_h = 0$ simulations. Further, the positions of the spectral minima in the $L_H = 1, 2$ spectra are at considerably higher energies, occurring at 51.75 and 52.07 eV, respectively. Thus, it is evident that multielectron effects are significant in shaping the observed Cooper minimum. This can be further investigated by considering the dipole emission from each individual orbital.

Although the Kohn-Sham orbitals are eigenstates of an auxilliary non-interacting system which yields the same electron density as the true system (in principle), insight into the effects of multielectron interaction on the shape of the Cooper minimum can be estimated by considering the individual Kohn-Sham orbital dipole emission. This analysis is supported by the agreement of Kohn-Sham orbital and experimental energies in Table 8.1. Fig. 8.4 depicts the dipole acceleration calculated from the (a) $3s_0$, (b) $3p_0$, and (c) $3p_{\pm1}$ Kohn-Sham orbitals. For each orbital, the intensity spectra calculated for a frozen multielectron potential (scaled $\times$1000, red) and for maximum multipolar expansion orders of $L_H = 0$ (scaled $\times$100, blue), 1 (scaled $\times$10, purple), and 2 (green) are shown.

The dipole acceleration spectrum from the $3s^2$ orbital is weak for the frozen and $L_H = 0$ multielectron interactions due to the low ionization rate when compared with the ionization rate for of the $3p$ orbitals. For $L_H = 1, 2$, however, the spectral intensity is significantly enhanced. For these spectra, the cutoff frequency near 105 eV coincides with the cutoff observed in the $3p_0$ and $3p_{\pm1}$ orbital spectra. Thus, this indicates that the enhancement is

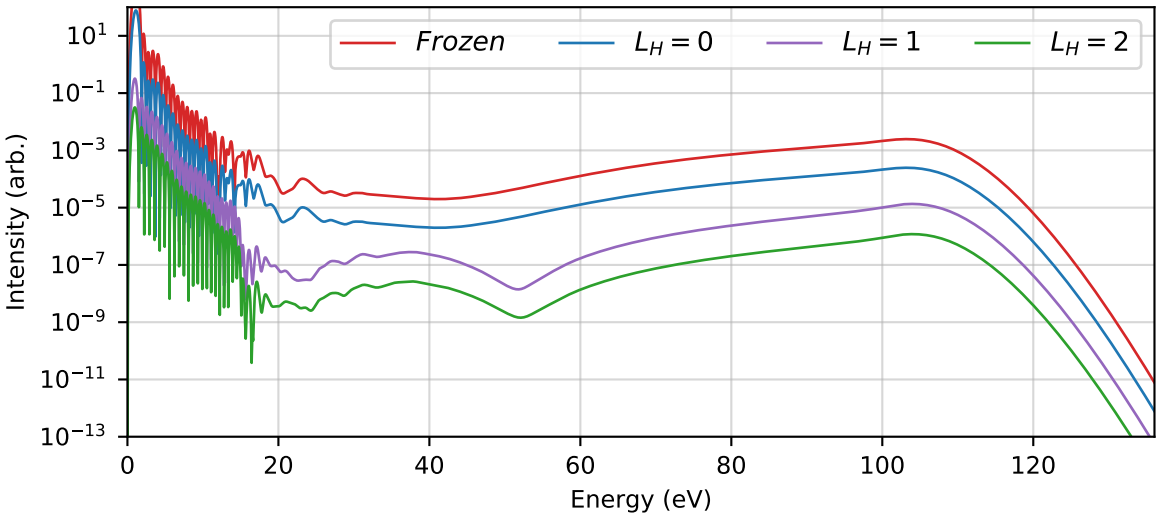

Figure 8.3 – The attosecond pulse spectra generated in argon by a single-cycle 1.8 µm driving field of peak intensity 1×10^{14} W cm^{-2} calculated with various levels of multielectron interaction. The attosecond pulse spectrum calculated with a frozen ionic potential is shown in red, while the spectra for a maximum Hartree multipole expansion of $L_H = 0, 1, 2$ and shown in blue, purple, and green, respectively. Each spectrum is scaled for clarity.

due to an interaction with the recollision electron and not ionization from and recombination to the $3s^2$ state.

The emission from the $3p$ sub-shell also changes significantly with L_H. The dipole acceleration spectrum from the $3p_0$ orbital, shown in (b), exhibits a broad and smooth spectral minimum. The position of the spectral minimum changes with L_H, however, occurring near 41 for the frozen and $L_H = 0$ spectra and near 45 eV for the $L_H = 1, 2$ spectra. Further, the minima in the $L_H = 1, 2$ spectra are narrower and deeper than the minima from the frozen and $L_H = 0$ spectra.

The spectra from the $3p_{\pm1}$ orbital exhibits the greatest change with L_H. For the frozen and $L_H = 0$ interactions, the spectrum exhibits a pronounced spectral minimum near 45 eV. The difference between the shapes of the spectral minima from the $3p_0$ and $3p_{\pm1}$ orbitals at this level of interaction can be ascribed to the behaviour of the continuum s-wave. For the $3p_{\pm1}$ orbital, the magnetic quantum number $m = \pm1$ is conserved due to the use of a linearly polarized driving field. Thus, from eq. (8.8), only the d-wave contributes to the dipole emission from the $3p_{\pm1}$ orbital and the smoothing of the minimum observed in the $3p_0$ emission due to the s-wave is absent. For $L_H = 1, 2$, the emission from the $3p_{\pm1}$ is significantly enhanced, particularly for energies below 60 eV. This is in agreement with observations in [89], wherein the omission of inter-channel interactions (i.e. interactions between the recollision and other electrons) significantly underestimated high harmonic emission between 30 and 50 eV.

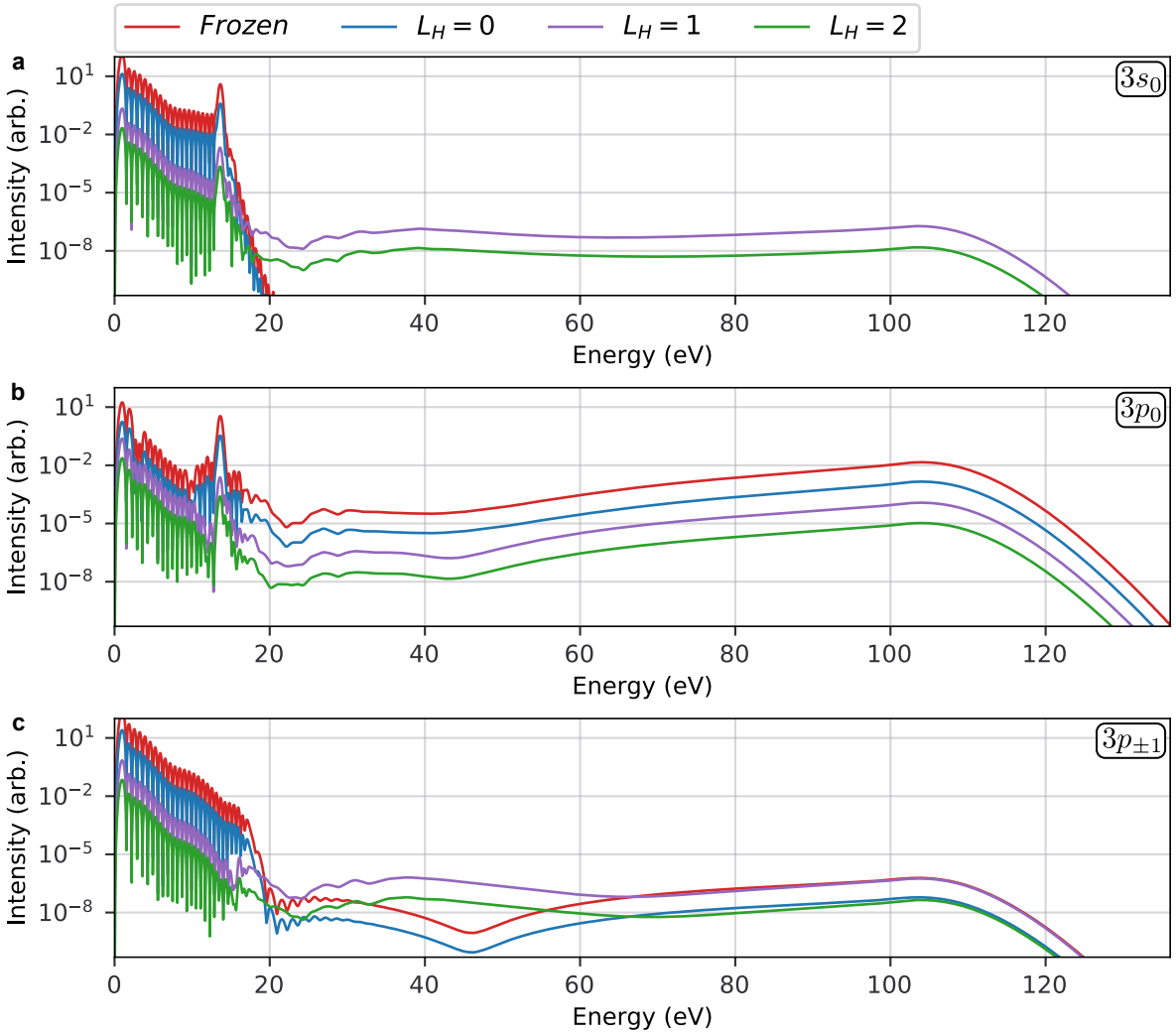

Figure 8.4 – The attosecond pulse spectra from individual orbitals in argon by a single-cycle 1.8 µm driving field of peak intensity 1×10^{14} W cm^{-2} with various levels of multielectron interaction. The emission from the (a) $3s^2$, (b) $3p_0$, and (c) $3p_{\pm1}$ Kohn-Sham orbitals are shown. The spectra calculated with a frozen ionic potential are shown in red and the spectra with maximum multipole expansion order of $L_H = 0, 1, 2$ are shown in blue, purple, and green, respectively.

While the Cooper minimum is typically thought of as a single electron effect, these results and those of [89] demonstrate that multielectron interaction is necessary in accurately describing the spectral characteristics of the minimum. The dependence of the Cooper minimum on the $3p_{\pm1}$ orbital suggests these interactions can be studied during recollision through the use of *in situ* measurement which uses a perturbing field polarized perpendicularly to the driving field [26]. This was not done here due to the restriction of the TD-DFT model to linearly polarized fields. In order to demonstrate the efficacy of this approach, however,

it is first necessary to demonstrate the sensitivity of *in situ* measurement to the transition moment phase around the Cooper minimum. This is the subject of the next section.

8.2 *In Situ* Measurement of the Photorecombination Time Delay Around the Cooper Minimum

The group delay variation around the Cooper minimum during recombination has been measured using attosecond *ex situ* measurement [7]. Here, the entirely optical measurement of the group delay variation around the Cooper minimum is demonstrated using *ab initio* simulated and experimental measurements.

Two variations of *in situ* measurement are used. For the simulated and experimental measurements, the collinear and non-collinear $\omega - 2\omega$ *in situ* methods are used, respectively. This is done for two reasons. First, the non-collinear measurement requires the calculation of the dipole moment across the driving field beam front and a time-delay scan, whereas the collinear measurement only requires a time-delay scan. Thus, simulating the collinear measurement is much faster than simulating the non-collinear measurement. Second, demonstrating the sensitivity of two variations of *in situ* measurement to the transition moment phase confirms the generality of the all-optical approach.

8.2.1 Simulated *In Situ* Measurement in Argon

A collinear $\omega - 2\omega$ measurement (described in Chapter 3) is simulated using an 800 nm driving pulse with a peak intensity of 2.75×10^{14} W/cm^2, corresponding to a semi-classical cutoff near 70 eV. The pulse is a flat-top pulse with a single-cycle ramp and pulse duration of 20 fs. The relative intensity of the second harmonic to the fundamental field is 10^{-4}. An absorbing boundary turned on at the radius $r_{abc} = 0.8 \times E_0/\omega_0^2$ was used in order to ensure the calculated high harmonic spectra included only short-trajectory contributions.

The spectrogram from the simulated *in situ* measurement is shown in Fig. 8.5. The contour plot shows the normalized even harmonic spectrum plotted with respect to the relative phase between the driving and perturbing pulses. The overlaid red line shows the maximizing relative phase for each even harmonic. The mapping of the relative phase to the high harmonic emission time is shown on the right axis. The result deviates from the expectedly linear chirp near the ionization threshold (i.e. below ~ 25 eV) and around the Cooper minimum, where a prominent decrease in emission time is observed. The behaviour near the ionization threshold can be attributed to Coulomb time delays [88] and the deviation near the cutoff can be attributed to the coalescence of long and short trajectories near the cutoff [91].

The overlaid solid blue line shows the expected result for recollision from a simple atom with a flat recombination phase calculated using the SFA [2] (shifted by $\pi/2$ for clarity). The

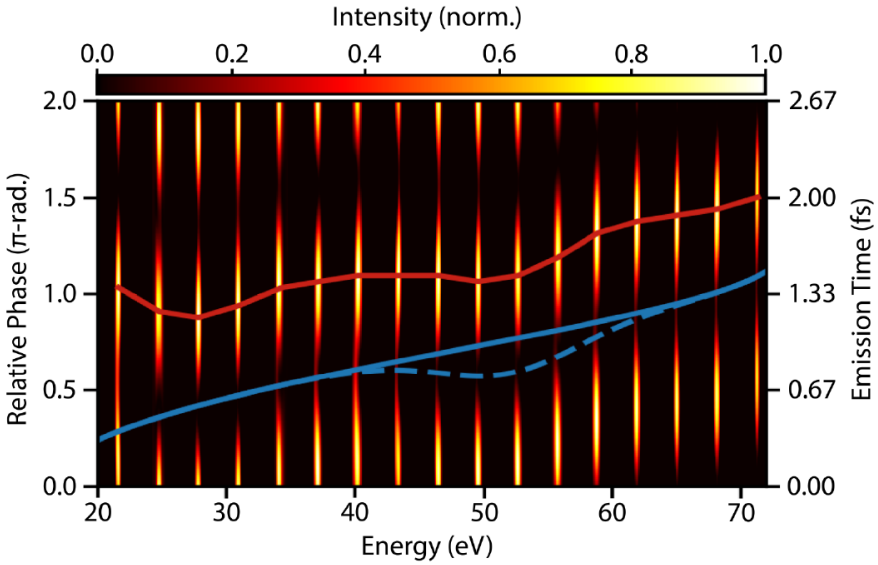

Figure 8.5 – The normalized even-harmonic spectrogram from the TD-DFT simulation of an $\omega - 2\omega$ *in situ* measurement in argon. The overlaid red line shows the relative phase which maximizes each even harmonic signal from the simulation. The blue overlaid solid (dashed) line shows the expected result for the maximizing relative phase from the semi-classical model without (with) the recombination phase around the Cooper minimum. The blue lines are shifted by $\pi/2$ for clarity.

linearity indicates that the variation observed in the TD-DFT result around the Cooper minimum is attributable to recombination effects. This is verified this by including a Lorentzian π-phase jump around $K_0^2/2 = 36$ eV with a bandwidth of $\sigma = 10$ eV in the recombination moment and SFA analysis as an approximation to the phase jump around the Cooper minimum:

$$\Phi(k) = \tan^{-1}\left(\frac{k^2 - K_0^2}{\sigma^2}\right). \tag{8.9}$$

The result of a simulated measurement calculated using the SFA which includes this transition moment phase is shown by the dashed blue line and agrees with the TD-DFT results.

The photorecombination delay is isolated by subtracting the expected semi-classical result from the measured result. This is depicted in Fig. 8.6 in red and compared with the photorecombination delay in blue [88]. Both the reconstructed photorecombination time delay from the simulated measurement and photoionization delay exhibit delays of ~ -150 as and have similar shapes around the Cooper minimum.

Thus, these *ab initio* results confirm the results of Chapter 6 and demonstrate that attosecond *in situ* measurement is sensitive to transition moment phase shifts due to electronic structure. This is confirmed experimentally in the next section using the non-collinear $\omega - 2\omega$

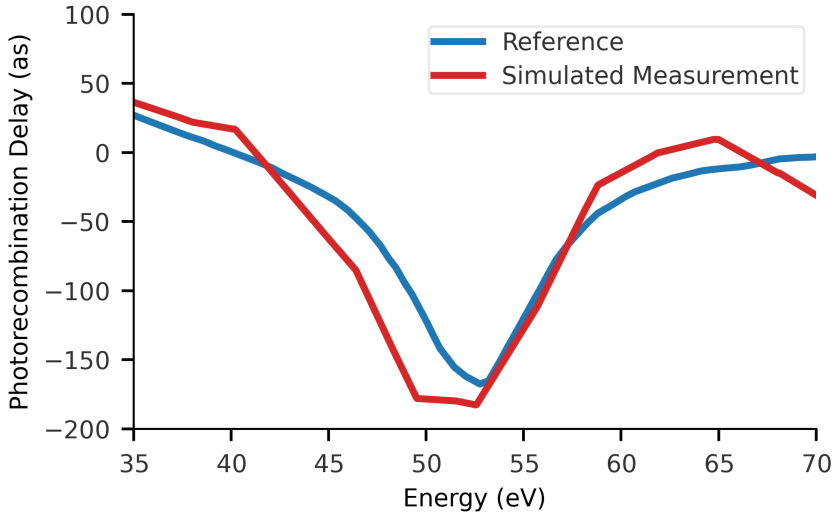

Figure 8.6 – A comparison of the photorecombination time delay reconstructed from the simulated spectrogram in Fig. 8.8 and calculated photorecombination time delay from argon around the Cooper minimum.

in situ measurement described in Chapter 3.

8.2.2 Experimental *In Situ* Measurement of the Cooper Minimum in Argon

For the experimental measurement of the recollision group delay in argon, the non-collinear *in situ* method is used. This method is ideally suitable for characterizing isolated attosecond pulses [39], as described in Chapter 3. For the sake of completeness, the experimental diagram is shown again in Fig. 8.7. As shown in (a), a 12 fs, polarization gated driving pulse of wavelength 1.8 µm (red) is focused into an argon gas jet. The pulse reaches an estimated peak intensity of 1×10^{14} W/cm^2 within the jet. Recollision is perturbed with a second-harmonic of the driving pulse (blue) with a relative intensity of 10^{-4} incident at an angle of 30 mrad with respect to the driving field, delayed by a time τ, as depicted by the blue pulse. In the gas jet (shown in b), the perturbing field modulates the recollision trajectories (red to blue), resulting in a frequency-dependent modulation of the near-field attosecond pulse wavefronts (red to blue). These modulations deflect the far-field attosecond pulse by a delay- and energy-dependent angle $\theta_\Omega(\tau)$. Fig. 8.7 (c) shows the measured angular deflection of the energies 60 (bottom) and 80 eV (top) as a function of time delay. The difference in the modulation phase is proportional to the difference in the group delay for these two energies. Such an analysis is repeated for each spectral component of the measured pulse.

We determine the group delay of the recollision electron using the relative delay of each spectral component with respect to that of a fixed energy. The unperturbed attosecond pulse spectrum is shown in Fig. 8.8 (a) in red, where the Cooper minimum is observed near 55 eV.

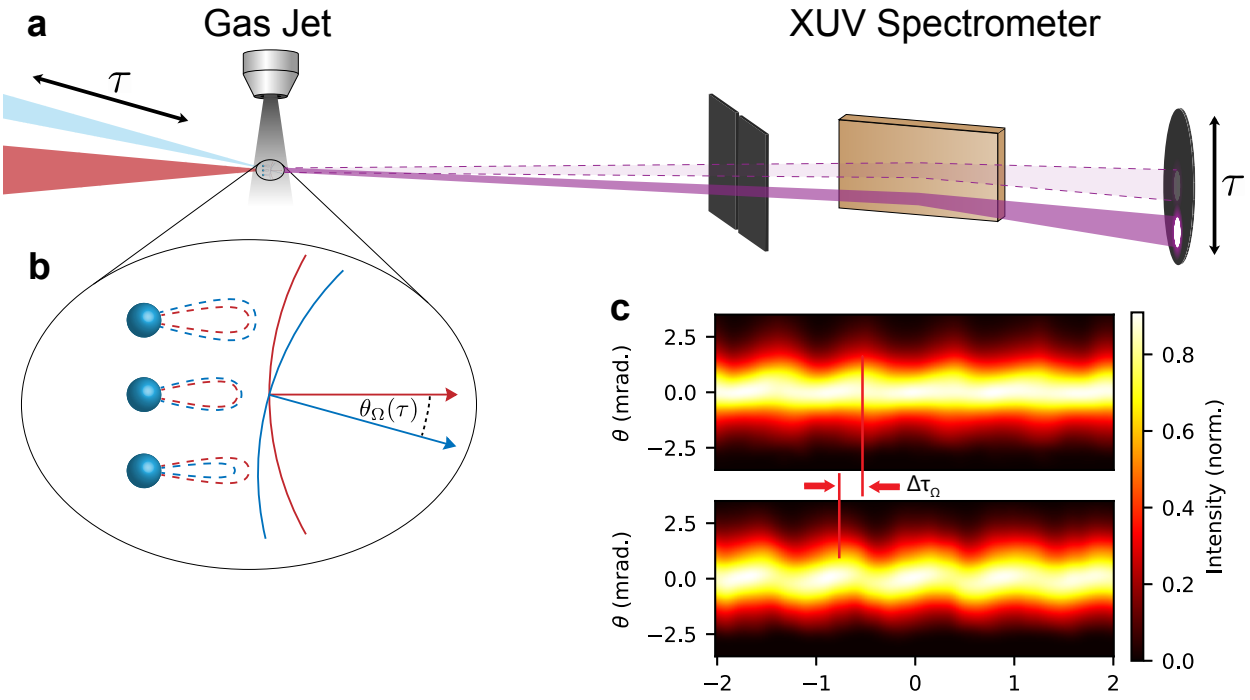

Figure 8.7 – (a) The polarization-gated driving pulse (red) and perturbing pulse delayed by time τ (blue) are focused into an argon gas jet. The perturbing pulse has a relative peak intensity of 10^{-4} and incident angle of $\theta_p = 30$ mrad with respect to the driving field. (b) The perturbation induces a delay dependent modulation of the electron trajectories and XUV wavefronts (red to blue) across the driving field beam front. This results in a deflection of the XUV beam in the far-field by a delay-dependent angle $\theta_\Omega(\tau)$ which is recorded in the XUV spectrometer. (c) The deflection of the XUV emission is recorded over a range of delays (in units of the perturbing field period T_p) and spectrally resolved. The resultant spectrograms for XUV energies of 60 (top) and 80 (bottom) are shown. The phase difference in the deflection modulation phase is proportional to the difference in group delay, $\Delta\tau_\Omega$ between the two energies.

The attosecond pulse spectrum from a TD-DFT simulation of the experimental conditions is shown by the dashed line (scaled ×10 for clarity). The position of the Cooper minimum in the TD-DFT simulation is lower than the experimental result, but the position of the Cooper minimum in HHG is known to be sensitive to phase-matching conditions [92].

The measured group delay is shown in Fig. 8.8 (b), where the experimental data is shown as a solid red line and the simulated result is shown by a dashed line. Both the experimental and theoretical group delay curves are predominantly linear up until the cutoff energy near 90 eV. Both, however, exhibit a variation in the group delay near the Cooper minimum and the experimental and theoretical results agree. The difference between the experimentally measured result and the expected semi-classical group delay in the absence of recombination effects is the photorecombination time delay. This is shown in Fig. 8.8 (c) in red with a

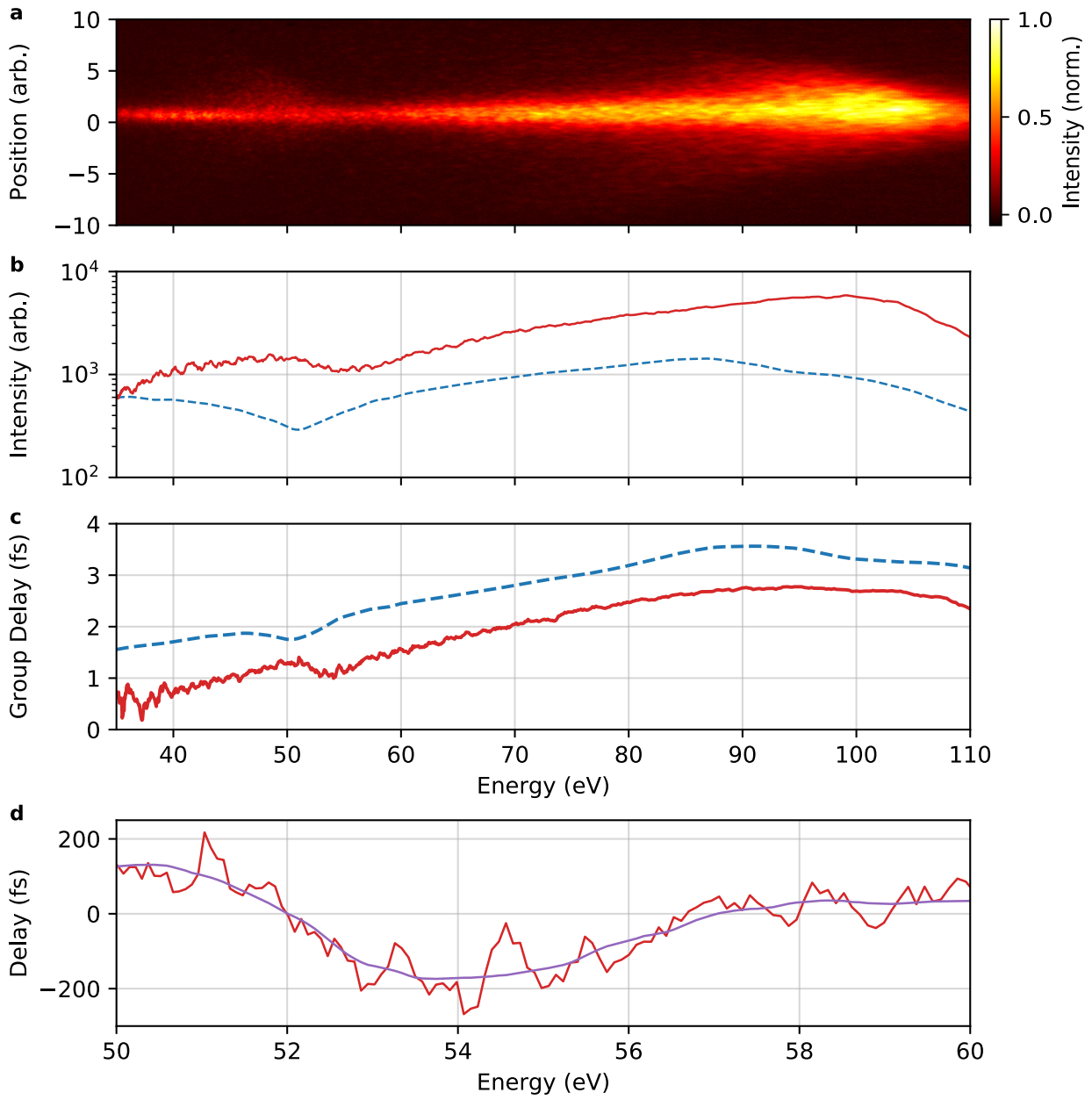

Figure 8.8 – (a) Full measured intensity spectrum, (b) integrated intensity spectra from experiment (solid red) and TD-DFT simulation of experimental conditions (dashed blue), (c) group delay from measurement (solid red) and TD-DFT simulation (dashed blue), (d) raw (red) and smoothed (purple) difference between measured group delay and group delay from hydrogenic atom.

smoothed curve in magenta. The maximum delay difference around the Cooper minimum near 54 eV is 160 as. The measured result agrees with the simulated collinear *in situ* measurement and studies of photorecombination time delays in argon [7].

8.3 Conclusions

In conclusion, the findings of Chapter 6 demonstrated the importance of transition moment phase shifts arising from electronic structure on recollision trajectories using the SFA. This was confirmed by the *in situ* measurements of the transition moment phase variation around the Cooper minimum in argon presented in this chapter. Both *ab initio* simulated and experimental measurements were presented using two different variations of *in situ* measurement, demonstrating the generality of the sensitivity of *in situ* measurement to transition moment phase shifts. As predicted in Chapter 6, this confirmation of the sensitivity of *in situ* measurement to phase shifts due to electronic structure demonstrate how the transition moment affects recollision trajectories and dynamics. This sensitivity calls methods which decouple propagation and recombination dynamics, such as quantitative rescattering theory [24], into question. In particular, *in situ* measurement is predicted to be sensitive to the transition moment phase shift only if said phase shift is fully accounted for within the saddle-point and, thus, the semi-classical trajectory analysis of recollision and the electron wave packet.

Further, the observed importance of the $3p_{\pm1}$ orbitals in the shaping of the Cooper minimum suggests a route to the exploration of electron correlation around the Cooper minimum using *in situ* techniques which employ orthogonally polarized perturbing and driving fields [26] and higher-order spectroscopies [93] to manipulate the polarization of the ion.

Summary: In this chapter, I demonstrated the importance of multielectron effects in shaping the Cooper minimum in argon and confirmed the sensitivity of attosecond *in situ* measurement to phase shifts due to electronic structure both theoretically and experimentally. The measurement of multielectron dynamics and electronic structure in xenon is the subject of the next chapter.

Chapter 9

The Giant Dipole Resonance in Xenon

Context: This chapter presents a study of recollision in xenon. Xenon exhibits transition moment phase shifts due to both electronic structure and multielectron interaction [88]. I first describe how these effects manifest during recollision in xenon and discuss the recollision-induced excitation of the giant dipole resonance [8]. I then present results from time-dependent density functional theory simulations of recollision in xenon which depict how the spectral characteristics of attosecond pulse emission are affected by electronic structure and multi-electron interaction. I then discuss the all-optical measurement of the correlated recollision dynamics responsible for the excitation of the giant dipole resonance using an extension of the strong field approximation which accounts for electron correlation [94].

The contents of this chapter are based entirely on my own research and are currently being tested experimentally. A publication detailing these findings is in preparation [95].

The final system studied in this thesis is the xenon atom. In previous chapters, the sensitivity of attosecond *in situ* measurement to transition moment phase shifts arising from electronic structure and multielectron interaction was demonstrated in distinct systems. The xenon atom exhibits both these features. The transition moment phase shift due to electronic structure arises due to the structure of the $5p$ orbital, the orbital most active in xenon during recollision. The $5p$ orbital radial wavefunction has three nodes and this leads to a Cooper minimum in the transition moment [88] similarly to the transition moment of the $3p$ orbital in argon. Recollision-induced multielectron interaction arises in xenon due to the Coulomb interaction between the recollision electron as it approaches its parent ion and the inner $4d$ sub-shell electrons. This interaction results in the excitation of a plasmonic oscillation within the inner $n = 4$ shell and is known as the *giant dipole resonance* (GDR). GDR in electronic systems are characteristic of many-body systems and ubiquitous in nature, extending from isolated atoms and molecules to solid-state systems [96]. Since recollision appears to be a universal response of matter to strong fields [1, 12, 11], the study of the GDR in xenon using all-optical recollision-based measurement serves as an exemplary measurement for future studies of multielectron interaction in a wide array of systems.

nl^g	ϵ_{DFT} (eV)	ϵ_{exp} (eV)	$\Delta\epsilon$ (%)
$1s^2$	-33065.57	-34561	4.42
$2s^2$	-5032.28	-5453	8.02
$2p^6$	-4741.13	-5107 (-4786)	7.44 (0.94)
$3s^2$	-1039.77	-1148.7	9.96
$3p^6$	-915.15	-1002.1 (-940.6)	9.08 (2.74)
$3d^{10}$	-682.70	-689.0 (-676.4)	0.92 (0.92)
$4s^2$	-189.18	-213.2	11.94
$4p^6$	-145.25	-146.7 (-145.5)	1.00 (0.18)
$4d^{10}$	-69.98	-69.5 (-67.5)	0.68 (3.60)
$5s^2$	-22.65	-23.3	2.83
$5p^6$	-12.49	-13.4 (-12.1)	7.02 (3.17)

Table 9.1 – The energies for the electron orbitals in xenon calculated using density-functional theory and experiment [87] labelled by the principle and orbital angular momentum quantum numbers, n and l, with their occupancy number g. The percent difference between the calculated and experimental are shown on the right. The density-functional theory calculation is performed using the LB94 exchange-correlation functional [54].

Measurements of the transition moment phase shift around the GDR in xenon have been accomplished using *ex situ* measurement-based studies of photoionization time delays [97]. Above the $4d$ ionization threshold (~ 70 eV), these measurements demonstrated the importance of two resonances: the GDR and a narrow relativistic spin-flip transition at 75 eV. Here, this spin-flip transition is not describable with the TD-DFT model due to the omission of relativistic effects. The excitation of the GDR, however, is well-described by the TD-DFT model.

This chapter begins with §9.1, which qualitatively describing the effects the Cooper minimum in the $5p_0 \rightarrow \epsilon d$ channel and recollision-induced ionic excitation have on attosecond pulse generation in xenon. These effects are then demonstrated in §9.2 with *ab initio* simulations using the TD-DFT model described in Chapters 4 and 5. In §9.3 and §9.4, the sensitivity of *in situ* measurement to these dynamics is then described using an extension of the SFA which includes electron correlation to first-order [94]. Finally, the results of a single-image *in situ* measurement in xenon atom calculated with the TD-DFT model are presented in §9.4.1 and they demonstrate the sensitivity of all-optical techniques to both multielectron interaction and electronic structure.

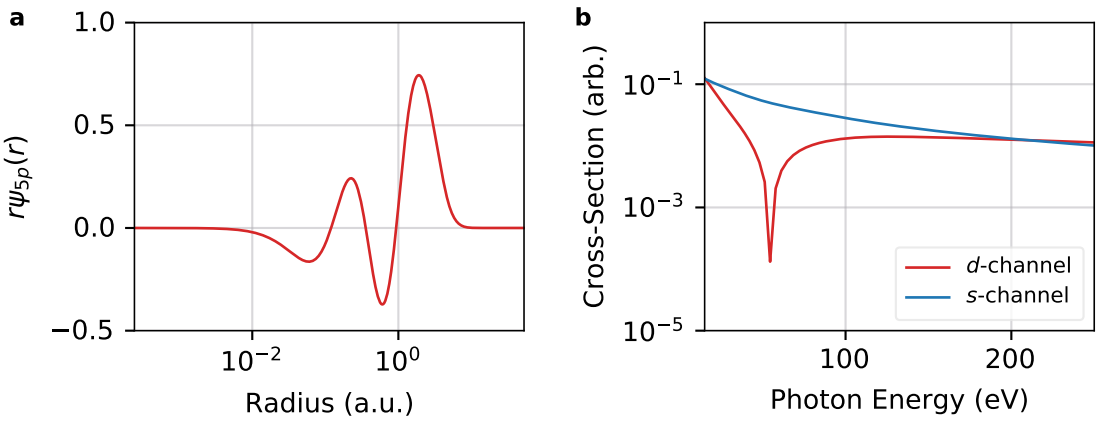

Figure 9.1 – (a) The $5p$ orbital radial wavefunction in xenon calculated using DFT. (b) The transition moment cross-section between the s- (blue) and d-wave (red) continua as a function of emitted photon energy.

9.1 Electronic Structure of Xenon

I first describe how the Cooper minimum and GDR in xenon occur during recollision qualitatively. In order to understand the transition moment phase in xenon, it is first necessary to describe the xenon ground state and how it is calculated. The ground state is calculated using the DFT model presented in Chapter 5 using the LB94 exchange-correlation functional [54]. The electron configuration, $1s^2 2s^2 2p^6 2p^6 3s^2 3p^6 3d^{10} 4s^2 4p^6 4d^{10} 5s^2 5p^6$, is defined *a priori* within the numerical program and the one-dimensional radial non-relativistic time-independent Kohn-Sham equation for the ground state. Table 9.1 lists the energies calculated using this model for each Kohn-Sham orbital alongside the experimentally measured energies and their percent difference. Due to the omission of relativistic effects, the calculated energies of the deeply bound core electrons exhibit large differences from the experimental values (with a maximum percent difference of 11.94%). The energies of the outer-lying electrons are in better agreement with the experimental measurements.

The orbital which dominates recollision dynamics in xenon is the $5p_0$ orbital. Like in argon, the radial wavefunction of the $5p$ orbital exhibits three radial nodes which lead to a Cooper minimum near 55 eV in its photoionization spectrum. This is shown in Fig. 9.1, where (a) shows the $5p$ orbital radial wavefunction and (b) shows the recombination cross-section coupling the $5p$ orbital wavefunction and the s- (blue) and d-wave (red) continuum states as a function of photon energy. A sharp minimum is observed in the d-wave cross-section, corresponding to a Cooper minimum. Around this minimum, a maximum photoionization time delay of 50 as has been predicted using TD-DFT models [88]. Both the origin of the Cooper minimum and its effect on recollision dynamics are similar to that in the argon atom and the reader is referred to the discussion of Cooper minima presented in Chapter 8 for the sake of brevity.

The GDR in xenon was first discovered through photoionization studies [98], where it was observed that xenon exhibits a broad shape resonance [99] with a *giant* cross-section within the $4d$ sub-shell extending from 70 to 150 eV. Although attempts at using single active electron approximations to explain the GDR were made [100], it has been conclusively demonstrated multielectron interaction is necessary for accurately describing the width and strength of this resonance [8, 101]. The GDR can be described as a plasmonic resonance, involving a collective oscillation of the $n = 4$ shell.

As discussed above, however, the $5p_0$ orbital dominates recollision dynamics in xenon. Since tunnel ionization is exponentially sensitive to the binding energy of an electron [102], the inner-shell $4d$ electrons ($I_p \approx 70$ eV) are expected to play a negligible role in recollision compared to $5p$ electrons ($I_p \approx 12.8$ eV). Thus, single-active electron approximations to recollision do not predict the GDR to be observable in recollision processes. Shiner *et al.*, however, observed this resonance within HHG and developed an inelastic scattering model beyond single-active electron approaches based on the SFA in order describe their observations [8]. They argued that a correlated recollision channel exists in xenon wherein the recollision electron interacts with a bound electron before recombination and excites the ion. This model was extended to include energy and momentum transfer from the recollision electron to the ion [94]. This interpretation has been validated theoretically with *ab initio* models using the time-dependent configuration interaction singles framework [101].

The inelastic scattering recollision model in xenon is depicted in Fig. 9.2. In xenon, there are two pathways for a recollision electron to recombine into its ground state. The direct channel (i.e. the conventional three-step model of recollision) is shown in (a): an electron (1) ionizes from the $5p_0$ orbital; (2) is accelerated by the field in the continuum (trajectory depicted as the red arrow); and (3) recombines with the parent ion into the hole (yellow) from which it left. The correlated channel is depicted in (b): (1) the electron ionizes from a $5p$ orbital; (2) is accelerated by the field; (3) interacts with a bound $4d$ electron through the Coulomb interaction (green field) as it approaches the ion, transferring momentum and energy to the ion, exciting the inner $4d$ electron to the $5p$ hole; and (4) recombines into the now vacant $4d$ hole. The promotion of the $4d$ electron to the $5p$ hole modifies the multielectron potential, inducing a collective oscillation (i.e. the GDR) within the $4d$ sub-shell.

In the next section, I present results from TD-DFT simulations of recollision in xenon which demonstrate the importance of both electronic structure and the recollision-induced excitation of the GDR in attosecond pulse generation in xenon.

9.2 Time-Dependent Density Functional Theory Simulations of Recollision in Xenon

I model recollision in xenon using the TD-DFT model presented in Chapters 4 and 5. Fig. 9.3 depicts the calculated attosecond pulse spectral intensity (red, left axis) and group

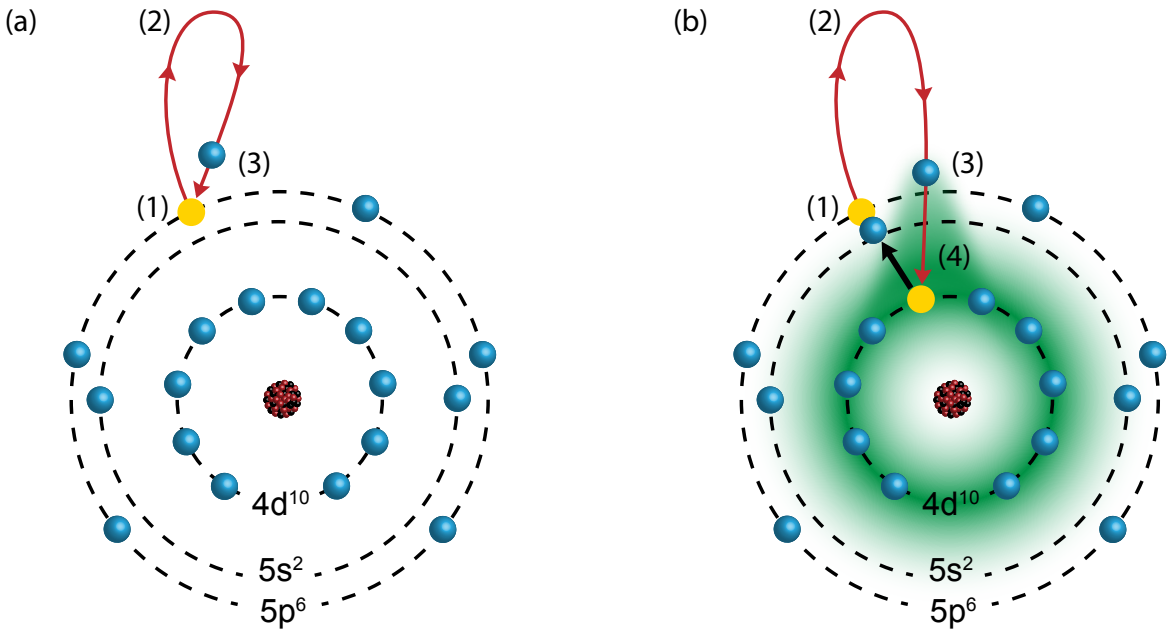

Figure 9.2 – In xenon, there are two recollision channels: (a) the direct recollision channel and (b) the correlated channel. In both channels, (1) an electron enters the continuum from the $5p$ sub-shell and (2) propagates in the continuum under the influence of the laser field. In the direct channel, (3) the recollision electron then recombines directly into the $5p$ hole (yellow). In the correlated channel, the recollision electron (3) interacts with a bound $4d$ sub-shell electron through the Coulomb interaction (depicted in green), promoting the $4d$ electron into the $5p$ hole, and then (4) recombines into the newly vacant $4d$ hole. This excitation of the $4d$ electron induces a collective oscillation within the $n = 4$ shell.

delay (blue, right axis) generated by a single-cycle 1.8 µm driving field with a peak intensity of 1.3×10^{14} W/cm^2 in xenon. For this simulation, only the $n = 4$ and $n = 5$ shells are propagated in time (i.e. orbitals with $n \leq 3$ are frozen in time). Absorbing boundaries [5] beginning at $R_{abc} = 1.125 \times F_0/\omega_0^2$ are used in order to ensure the observed dipole emission includes predominantly short trajectory contributions. The spectral intensity exhibits a minimum near 55 eV, corresponding to the Cooper minimum described above. Around this minimum, a small deviation within the group delay of 50 as from the expected linear slope of the *atto-chirp* is observed.

Between 70 and 130 eV, the spectral intensity is significantly enhanced due to the GDR. Near the cutoff, modulations in both the spectral intensity and measured group delay due to the interference between long and short trajectories leading are observed. Between 70 and 85 eV, narrow and structured modulations within the spectral intensity and group delay are observed. These modulations arise from the phase of the matrix element describing the Coulomb interaction between the recollision electron and the ion and depend on the momentum transferred to the ion [94]. This will be discussed in the next section.

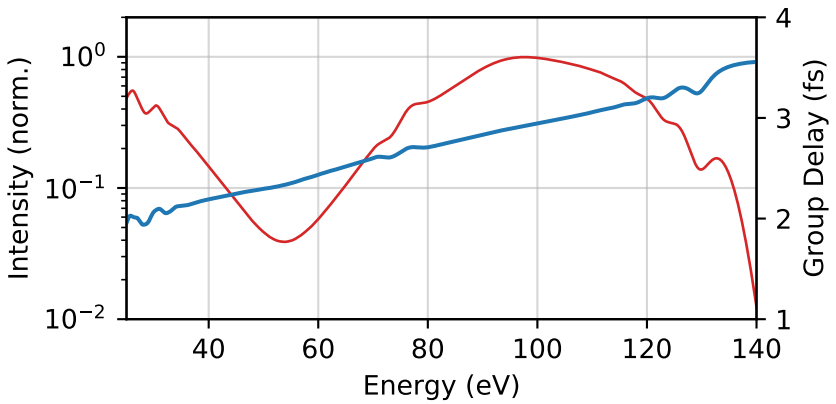

Figure 9.3 – The attosecond pulse spectral intensity (red, left axis) and group delay (blue, right axis) calculated from xenon using a single-cycle 1.8 µm driving field with a peak intensity of 1.3×10^{14} W/cm^2.

As in Chapter 8, I now consider the dipole emission from each Kohn-Sham orbital. The spectral intensity (red, left axis) and group delay (blue, right axis) of the absolute value of the dipole spectra from each distinct Kohn-Sham orbital within the $n = 4$ and 5 shells are depicted in Fig. 9.4. The group delay for all orbitals exhibits a predominantly linear variation with energy, implying recollision is the predominant mechanism in generating the dipole emission. Each spectrum exhibits several resonances which are not reflected in the total spectrum in Fig. 9.3. These resonances correspond to virtual transitions between the set of Kohn-Sham orbitals. For each transition from orbital a to orbital b, there is an equal transition with the opposite sign from orbital b to orbital a. Thus, these virtual transitions are not present within the total observed dipole moment.

The dipole emission from the $n = 5$ shell orbitals resembles the dipole emission predicted by the conventional three-step model and SFA. In particular, the dipole emission from the $5p_0$ orbital exhibits a flat plateau structure until the cutoff near 140 eV. The group delay increases linearly, except for a variation near 55 eV, corresponding to a virtual transition between the $5p_0$ and $4d$ states. The dipole spectra from the $n = 5$ shell is depicted in Fig. 9.5 (b) by the solid red line. The solid orange and dashed blue lines depict the dipole emission from the $5s$ and $5p$ sub-shells, respectively. As expected, the dipole emission is dominated by the $5p$ sub-shell.

The dipole emission from the $n = 4$ shell, however, contains significant contributions from all orbitals within the shell. From Fig. 9.4, the dipole emission from the $4p$ sub-shell is comparable to the emission from the $4d$ sub-shell. Further, the contribution from the $4s$ orbital, although weaker, is much stronger than the emission from the $5s$ orbital. This is accentuated in Fig. 9.5, where the total emission from the $n = 4$ shell (red) and the $4s$ (orange), $4p$ (green), and $4d$ (blue) sub-shells are depicted. Unlike the $n = 5$ shell, where the $5p$ sub-shell dominates the dipole emission, the dipole emission from the $4d$ and $4p$ sub-

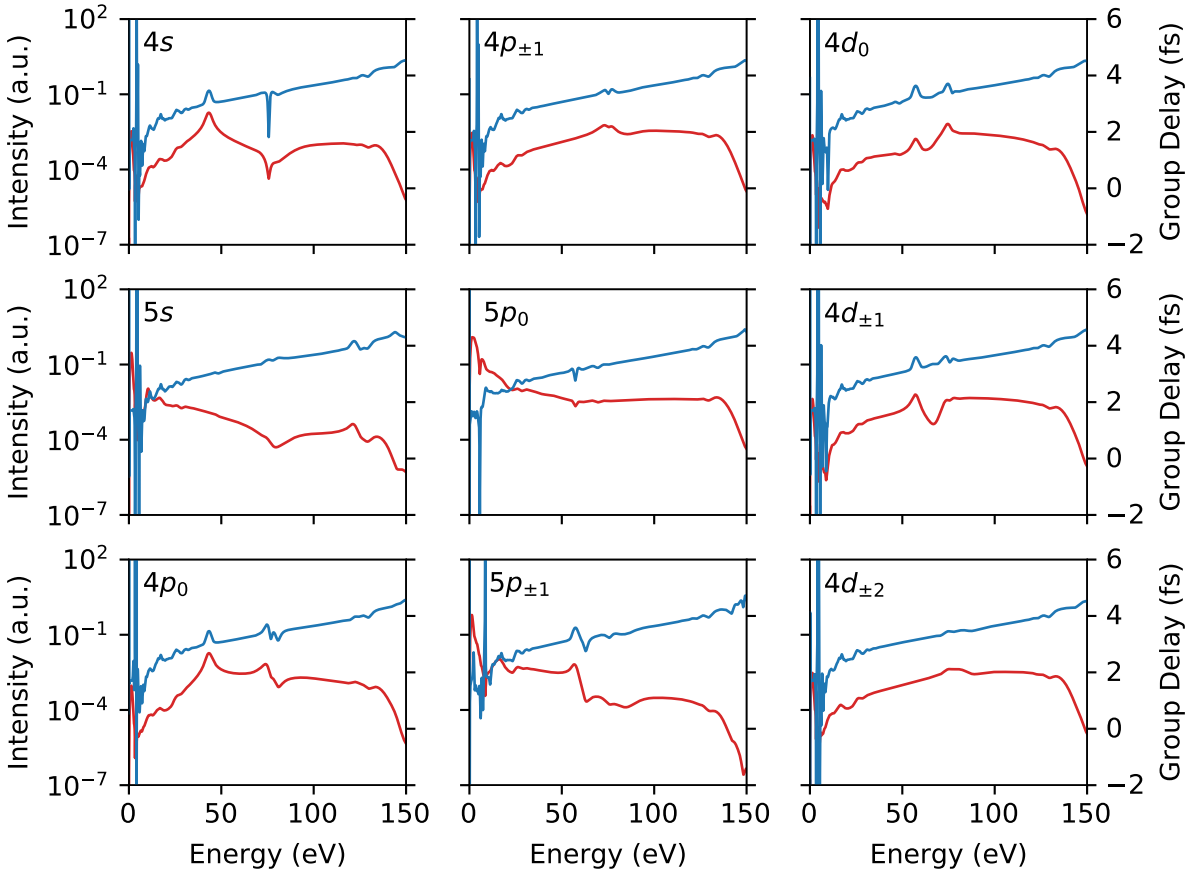

Figure 9.4 – The attosecond pulse spectral intensity (red, left axis) and group delay (blue, right axis) from individual Kohn-Sham orbitals in xenon calculated using a single-cycle 1.8 µm driving field with a peak intensity of 1.3×10^{14} W/cm^2.

shells significantly contributes to the total dipole emission, with the $4d$ emission being only $\sim 2\times$ the $4p$ emission. Further, between the energies of 59 and 75 eV, the dipole emission is dominated by the $4p$ emission.

These results demonstrate the importance of multielectron dynamics throughout the entire inner $n = 4$ shell in shaping attosecond pulse spectra generated in xenon. The dynamics induced by the promotion of the $4d$ electron to the $5p_0$ hole by the recollision electron result in a dynamic modification of the multielectron interaction potential, coupling the entire $n = 4$ shell. This model will be used to investigate the all-optical measurement of these correlated dynamics. First, however, the extension of the SFA including correlation [94] will be discussed in order to interpret the aforementioned measurement.

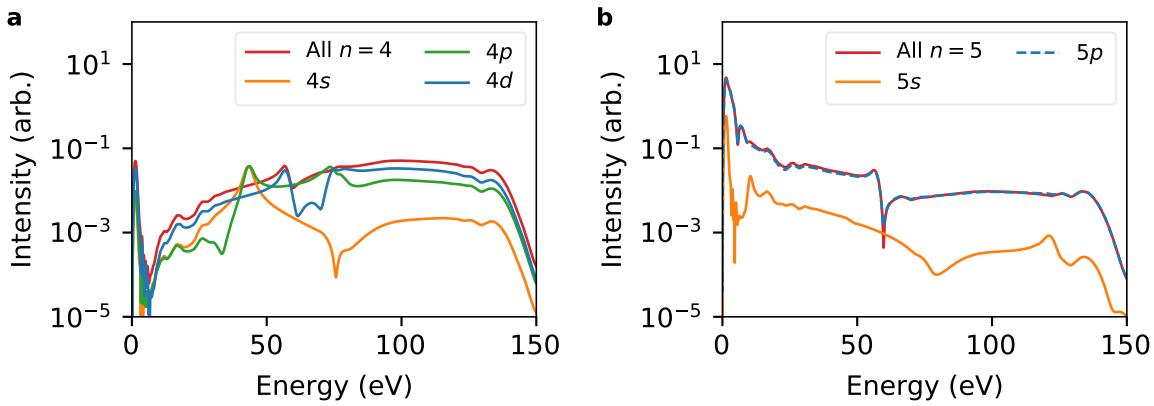

Figure 9.5 – The attosecond pulse spectral intensity from the (a) $n = 4$ and (b) $n = 5$ shells in xenon. The individual orbital contributions are shown alongside the total shell emission. a single-cycle 1.8 µm driving field with a peak intensity of 1.3×10^{14} W/cm^2.

9.3 The Correlated Strong Field Approximation

I now describe the excitation of the GDR during recollision using an extension of the SFA which includes the Coulomb interaction between the recollision electron and the ion as an intermediary step before recombination [94]. I refer to this model as the correlated strong field approximation (C-SFA). The dipole spectrum from the C-SFA at frequency Ω, $\tilde{\mathbf{D}}(\Omega)$, is calculated within the eikonal-Volkov approximation and is given as follows:

$$\begin{aligned}\tilde{\mathbf{D}}_c(\Omega) = \int d\mathbf{k} \int d\mathbf{q} \int_{-\infty}^{\infty} dt_r \int_{-\infty}^{t_r} dt_{ee} \int_{-\infty}^{t_{ee}} dt_b \mathbf{d}_c^*(\mathbf{P}(t_r)) a_{ee}(\mathbf{P}(t_{ee}), \mathbf{q}) \\ \times \mathbf{E}(t_b) \cdot \mathbf{d}_0(\mathbf{P}(t_b) - \mathbf{q}) e^{-i\left[I_{p,c}(t_r - t_{ee}) + I_{p,d}(t_{ee} - t_b) + S(\mathbf{k}-\mathbf{q}, t_b, t_{ee}) + S(\mathbf{k}, t_{ee}, t_r) - \Omega t_r\right]},\end{aligned} \tag{9.1}$$

$$\mathbf{d}_0(\mathbf{k}) = \langle \mathbf{k}| \langle \Psi_d | \hat{\mathbf{r}} | \psi_0 \rangle , \tag{9.2}$$

$$a_{ee}(\mathbf{k}, \mathbf{q}) = \langle \mathbf{k}| \langle \Psi_c | \hat{v}_{ee} | \Psi_d \rangle |\mathbf{k} - \mathbf{q}\rangle , \tag{9.3}$$

$$\mathbf{d}_c(\mathbf{k}) = \langle \mathbf{k}| \langle \Psi_c | \hat{\mathbf{r}} | \psi_0 \rangle . \tag{9.4}$$

Here, $\mathbf{P}(t) = \mathbf{k} + \mathbf{A}(t) - \mathbf{A}(t_r)$ is the kinetic momentum of the recollision electron at time t, $\mathbf{k}$ is the momentum the electron recombines with, $\mathbf{q}$ is the momentum transferred to the ion during the multi-electron interaction, t_r is the time of recombination, t_{ee} is the time of multi-electron interaction, t_b is the time of ionization, $\hat{v}_{ee}$ describes the multi-electron interaction, $|\Psi_d\rangle |\mathbf{k} - \mathbf{q}\rangle$ describes the state of the ion and recollision electron after ionization (i.e. before the ion excitation), $|\Psi_c\rangle |\mathbf{k}\rangle$ describes the state of the ion and recollision electron after the multi-electron interaction, $I_{p,d}$ is the ionization potential of the direct channel, and $I_{p,c}$ is the ionization potential of correlated state. The semi-classical action is calculated using eq. (2.18).

As in the conventional SFA, this integral can be solved using the saddle-point approximation. In order to properly account for the multielectron interaction, however, the phase of $a_{ee}(\mathbf{P}(t_{ee}), \mathbf{q})$ must be included in the integrand phase. In doing so, the following set of saddle-point equations for $\mathbf{k}$, $\mathbf{q}$, t_b, t_{ee}, and t_r is found:

$$0 = \frac{[\mathbf{P}(t_b) - \mathbf{q}]^2}{2} + I_{p,d}, \tag{9.5}$$

$$0 = \frac{[\mathbf{P}(t_b) - \mathbf{q}]^2}{2} - \frac{\mathbf{P}^2(t_b)}{2} + I_{p,d} - I_{p,c}, \tag{9.6}$$

$$0 = \frac{[\mathbf{P}(t_b)]^2}{2} + I_{p,c} - \Omega, \tag{9.7}$$

$$0 = \int_{t_b}^{t_{ee}} [\mathbf{P}(\tau) - \mathbf{q}]\, d\tau + \Phi_c'(\mathbf{q}), \tag{9.8}$$

$$0 = \int_{t_b}^{t_r} [\mathbf{P}(\tau)]\, d\tau - \mathbf{q}(t_{ee} - t_b), \tag{9.9}$$

where

$$\Phi_c(\mathbf{q}) = \arg\left[a_{ee}(\mathbf{P}(t_{ee}), \mathbf{q})\right] \tag{9.10}$$

is assumed to depend solely on the momentum transferred to the ion from the recollision electron [94]. The meaning of each of these equations can be mapped to recollision dynamics as in the conventional three-step model. Eqs. (9.5 - 9.7) describe energy conservation during the tunnelling, multielectron interaction, and recombination steps, respectively. Eqs. (9.8) and (9.9) describe the displacement conditions for the multielectron interaction and recombination steps, respectively.

If $\Phi_c(\mathbf{q})$ is a constant (i.e. $\Phi_c'(\mathbf{q}) = 0$), then the phase of the emitted attosecond pulse is equal to that of the direct recollision channel. In this case, the times of multi-electron interaction and recombination are both equal to the recombination time in the direct channel and the electron must return to the ion for both recombination and the multielectron interaction. The dynamics of the correlated channel are indistinguishable from those of the direct channel in this case. The dynamics within the correlated channel and emitted attosecond pulse will differ if the phase of the multi-electron interaction varies with $\mathbf{q}$ [94].

From here, vector notation is omitted, as all components are assumed to be parallel to $\hat{\mathbf{z}}$. For the case where $\Phi'(q) \neq 0$, the saddle-point equations are expanded as a series with respect to $\Phi_c'(\mathbf{q})$ about the system with $\Phi_c'(\mathbf{q}) = 0$. I label the solutions to eqs. (9.5 - 9.9) when $\Phi_c'(q) = 0$ as $\overline{k}$, $\overline{q}$, $\overline{t}_b$, $\overline{t}_{ee}$, and $\overline{t}_r$ and refer to them as the zeroth-order solutions. Note that, $\overline{k} - \overline{q}$ is equal to the recombination momentum from the direct channel. The saddle-point solutions are expanded to first-order in $\Phi_c'(q)$ about the zeroth-order solutions such that, for the saddle-point variable μ,

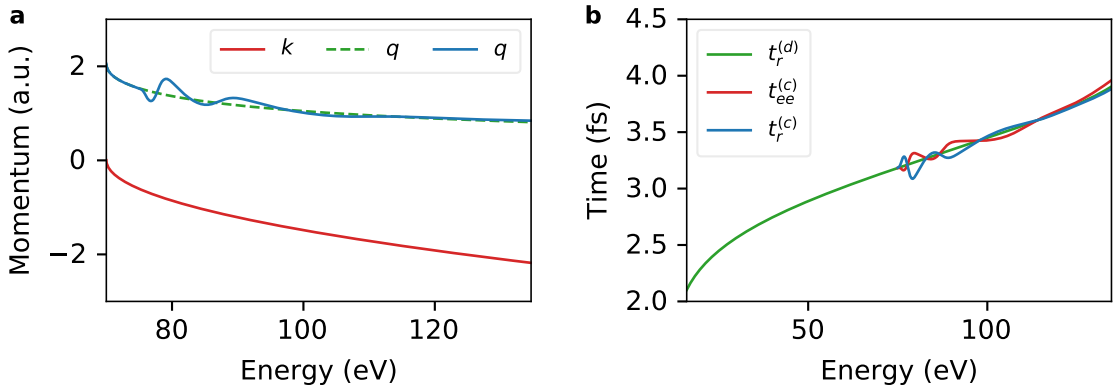

Figure 9.6 – (a) The momentum of recombination k (red) and transferred momentum q (blue) within the correlated recollision channel in xenon. The transferred momentum for the case where $\Phi_c'(q) = 0$ is shown by the dashed green line. (b) The times of recombination $t_r^{(d)}$ in the direct channel (green) and the times of multielectron interaction $t_{ee}^{(c)}$ (red) and recombination $t_r^{(c)}$ (blue) in the correlated channel in xenon found using eqs. (9.5-9.14). A sinusoidal 1.8 µm driving field with a peak intensity of 1.3×10^{14} W/cm^2, a direct-channel ionization potential of 12.8 eV, and a correlated state binding potential of 70 eV were used for this calculation.

$$\mu^{(1)} = \overline{\mu} + \Delta\mu. \tag{9.11}$$

This results in the following set of corrections to the zeroth-order saddle-point solutions:

$$\Delta q = \frac{\overline{q}}{(\overline{k} - \overline{q})\overline{k}} F(t_r)\Phi'(\overline{q}), \tag{9.12}$$

$$\Delta t_{ee} = \frac{1}{\overline{k} - \overline{q}}\Phi'(\overline{q}), \tag{9.13}$$

$$\Delta t_r = \frac{\overline{q}}{(\overline{k} - \overline{q})\overline{k}}\Phi'(\overline{q}), \tag{9.14}$$

and $\Delta k = \Delta t_b = 0$.

Fig. 9.6 depicts the saddle-point solutions from the C-SFA calculated using a sinusoidal 1.8 µm driving field with a peak intensity of 1.3×10^{14} W/cm^2, the multielectron interaction matrix element phase from [94], and direct and correlated channel binding energies of 12.8 and 70 eV, respectively. Only short-trajectory solutions are shown. Fig. 9.6 (a) depicts the momentum of recombination (red) and transferred momentum (blue), with the transferred momentum from the C-SFA with $\Phi_c'(q) = 0$ (dashed green) as a reference. Due to the phase of the multielectron interaction matrix element, several modulations within the transferred momentum are observed around 80 eV. These modulations are reflected in the times of mul-

tielectron interaction (red) and recombination (blue) from the correlated channel depicted in Fig. 9.6 (b). When $\Phi_c'(q) = 0$, both the time of multielectron interaction and recombination are equal to the recombination time from the corresponding direct channel, shown in green.

The saddle-point solutions all reflect the shape of the phase of $a_{ee}(q)$, implying that the recollision electron wave packet is affected by the multielectron interaction. This modification of the wave packet from that of the conventional SFA is supported by *ab initio* simulations of HHG in xenon [101]. The sensitivity of the saddle-point solutions to the multielectron interaction phase implies that attosecond *in situ* measurement is sensitive to these dynamics. This will be demonstrated below.

9.4 *In Situ* Measurement in Xenon

I consider a single-image *in situ* measurement in xenon, as described in Chapter 3. it is necessary to incorporate the momentum transfer dynamics into the phase shift induced by a perturbing infrared field. From the integrand phase in eq. 9.1, the perturbation-induced phase shift in the correlated channel is given as follows:

$$\sigma(k, q, t_b, t_{ee}, t_r, \phi) = \int_{t_b}^{t_{ee}} [P(\tau) - q] \cdot A_p(\tau, \phi) d\tau + \int_{t_{ee}}^{t_r} P(\tau) \cdot A_p(\tau, \phi) d\tau. \tag{9.15}$$

where $A(t)$ and $A_p(t, \phi)$ are the driving and perturbing field vector potentials at time t. The relative phase between the driving and perturbing fields is $\phi = k_0 y \sin(\theta)$, where y is the vertical position in the near-field, k_0 is the perturbing field wave-vector, and θ is the angle between the driving and perturbing fields. The difference between eq. (9.15) and the perturbation-induced phase shift in a simple atom without a correlated channel can be made clear by substituting the saddle-point variables with their zeroth-order solutions and their first-order corrections:

$$\begin{aligned}
\sigma(k, q, t_b, t_{ee}, t_r, \phi) &\approx \int_{\bar{t}_b}^{\bar{t}_{ee}+\Delta t_{ee}} \left[\overline{P}(\tau) - \overline{q} - \Delta q\right] \cdot A_p(\tau, \phi) d\tau + \int_{\bar{t}_{ee}+\Delta t_{ee}}^{\bar{t}_r+\Delta t_r} P(\tau) \cdot A_p(\tau, \phi) d\tau \\
&= \int_{\bar{t}_b}^{\bar{t}_r} \left[\overline{P}(\tau) - \overline{q}\right] \cdot A_p(\tau, \phi) d\tau + \int_{\bar{t}_r}^{\bar{t}_r+\Delta t_r} \overline{P}(\tau) \cdot A_p(\tau, \phi) d\tau \\
&\quad - \int_{\bar{t}_r}^{\bar{t}_r+\Delta t_{ee}} \overline{q} \cdot A_p(\tau, \phi) d\tau - \int_{\bar{t}_b}^{\bar{t}_{ee}+\Delta t_{ee}} \Delta q \cdot A_p(\tau, \phi) d\tau.
\end{aligned} \tag{9.16}$$

Since $\overline{P}(t) - \overline{q}$ is equal to the kinetic momentum of the recollision electron in the direct channel at time t, the first integral in eq. (9.16) is equal to the perturbation-induced phase shift from the modified action in the direct channel given by eq. (3.13) :

$$\sigma_0(\overline{k}-\overline{q},\bar{t}_b,\bar{t}_r,\phi)=\int_{\bar{t}_b}^{\bar{t}_r}\left[\overline{P}(\tau)-\overline{q}\right]\cdot A_p(\tau,\phi)d\tau \tag{9.17}$$

With this,

$$\begin{aligned}\sigma(k,q,t_b,t_{ee},t_r,\phi)\approx\sigma_0(\overline{k}-\overline{q},\bar{t}_b,\bar{t}_r,\phi)+\int_{\bar{t}_r}^{\bar{t}_r+\Delta t_r}\overline{P}(\tau)\cdot A_p(\tau,\phi)d\tau\\ -\int_{\bar{t}_r}^{\bar{t}_r+\Delta t_{ee}}\overline{q}\cdot A_p(\tau,\phi)d\tau-\int_{\bar{t}_b}^{\bar{t}_{ee}+\Delta t_{ee}}\Delta q\cdot A_p(\tau,\phi)d\tau.\end{aligned} \tag{9.18}$$

Expanding eq. (9.18) to first-order with respect to the saddle-point corrections in eqs. (9.12 - 9.14) yields the following (note that $\bar{t}_{ee}=\bar{t}_r$):

$$\begin{aligned}\sigma(k,q,t_b,t_{ee},t_r,\phi)&\approx\sigma_0(\overline{k}-\overline{q},\bar{t}_b,\bar{t}_r,\phi)+\Delta t_r\overline{k}-\Delta t_{ee}\overline{q}\cdot A_p(\bar{t}_r,\phi)-\int_{\bar{t}_b}^{\bar{t}_r}\Delta q\cdot A_p(\tau,\phi)d\tau\\ &=\sigma_0(\overline{k}-\overline{q},\bar{t}_b,\bar{t}_r,\phi)+\left(\frac{\overline{q}}{(\overline{k}-\overline{q})\overline{k}}\Phi_c'(\overline{q})\right)\overline{k}-\left(\frac{1}{\overline{k}-\overline{q}}\Phi_c'(\overline{q})\right)\overline{q}\\ &\quad-\int_{\bar{t}_b}^{\bar{t}_r}\Delta q\cdot A_p(\tau,\phi)d\tau\\ &=\sigma_0(\overline{k}-\overline{q},\bar{t}_b,\bar{t}_r,\phi)-\int_{\bar{t}_b}^{\bar{t}_r}\Delta q\cdot A_p(\tau,\phi)d\tau\\ &=\sigma_0\left(\overline{k}-\overline{q}-\Delta q,\bar{t}_b,\bar{t}_r\phi\right)+\mathcal{O}\left(\Phi_c'^2(\overline{q})\right).\end{aligned} \tag{9.19}$$

Thus, the first-order correction to the perturbation-induced phase shift, $\Delta\sigma(\Delta\sigma,\bar{t}_b,\bar{t}_r,\phi)$, is proportional to the change in transferred momentum caused by the phase of the multielectron interaction:

$$\Delta\sigma^{(1)}(\Delta q,\bar{t}_b,\bar{t}_r,\phi)=-\int_{\bar{t}_b}^{\bar{t}_r}\Delta q\cdot A_p(\tau,\phi)d\tau. \tag{9.20}$$

In the subsequent discussion, I focus on this first-order correction to the perturbation-induced phase shift, although higher-order corrections due to the modified saddle-point solutions can be made. For the sake of completeness, the second-order correction is given as follows:

$$\Delta\sigma^{(2)}(\overline{k},\overline{q},\bar{t}_r)=\left(-\frac{\overline{q}A_p'(\bar{t}_r,\phi)}{2\overline{k}^2-2\overline{k}\overline{q}}+\frac{\overline{q}A_p(\bar{t}_r,\phi)F(\bar{t}_r)}{\overline{k}(\overline{k}-\overline{q})^2}\right)\Phi_c'^2\left(\overline{q}\right). \tag{9.21}$$

From this, it is evident that an *in situ* measurement of the correlated channel will yield a measurement of the change in the transferred momentum due to the multielectron interaction matrix element phase. This is depicted in Fig. 9.7, where the maximizing relative

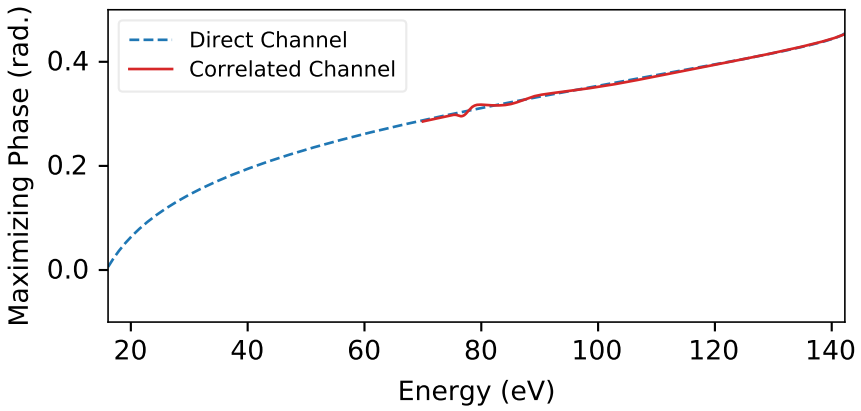

Figure 9.7 – The relative phase between the perturbing and driving fields in a single-image *in situ* measurement which maximizes the intensity of each frequency component of the direct (dashed blue) and correlated (solid red) channels. A sinusoidal 1.8 µm driving field of peak intensity 1.3×10^{14} W/cm^2 was used and the same-colour perturbing field has an intensity of 10^{-4} relative to the driving field.

phase of the direct (dashed blue) and correlated (solid red) channels is shown as a function of energy. The momentum transfer exhibited in Fig. 9.6 (a) is clearly reflected in the measurement. From eq. 9.12, this change in the transferred momentum can be mapped to the matrix element phase up to a constant.

9.4.1 Simulated *In Situ* Measurement in Xenon

I confirm this by simulating a single-image *in situ* measurement in xenon using the TD-DFT model. Fig. 9.8 (a) shows the simulated single-image *in situ* measurement spectrogram which shows the variation of the attosecond pulse spectrum with the effective time delay between the driving and perturbing fields. For these simulations, a single-cycle 1.8 µm driving field with a peak intensity of 1.3×10^{14} W/cm^2 was used and the same-frequency perturbing field had an intensity of 10^{-4} relative to that of the driving field. The total effective delay scanned spans eight optical cycles. A uniform intensity profile was assumed for both the driving and perturbing fields.

The phase of each spectral component's modulation with the effective time delay is shown in Figs. 9.8 (b), which shows the measurement results from the xenon TD-DFT simulation (solid red), a TDSE solution of a hydrogenic atom with its nuclear charge scaled such that $I_p = 12.8$ eV (dashed blue), and the C-SFA (solid green). Absorbing boundaries [5] were used for the hydrogenic and TD-DFT simulations, beginning at $R_{abc} = 0.8 \times E_0/\omega_0^2$ and $1.125 \times E_0/\omega_0^2$, respectively. A larger boundary was used for the TD-DFT simulation in order to observe a stronger enhancement due to the GDR.

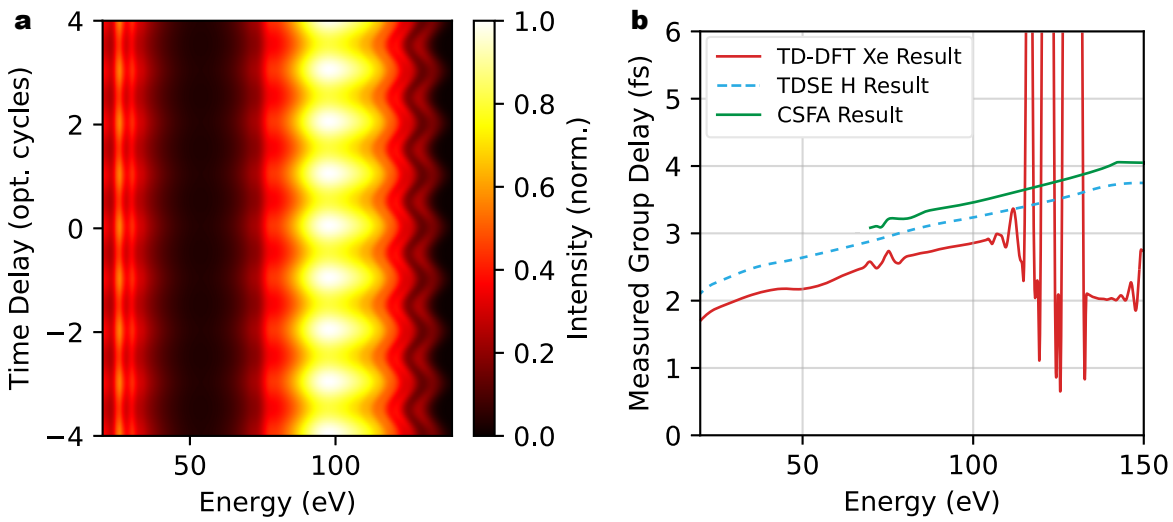

Figure 9.8 – (a) The single-image *in situ* spectrogram from xenon depicting the variation of the attosecond pulse spectral intensity with the effective time delay between the driving and perturbing fields. (b) The group delay measured from the single-image *in situ* measurement. The measurement result from the time-dependent density functional theory simulation in (a) is shown in red, the result from an equivalent hydrogenic atom is shown in dashed blue, and the result from a simulated measurement calculated with the correlated strong field approximation is shown in green. The driving field is a single-cycle 1.8 µm pulse with a peak intensity of 1.3×10^{14} W/cm^2. The perturbing field has an intensity of 10^{-4} relative to the driving field.

The measured group delay from the hydrogenic atom varies predominantly linear with respect to energy, as predicted by the SFA, and serves as a reference for the other results. Below 65 eV, the measured group delay from the xenon TD-DFT simulation predominantly increases linearly with energy, except for a small variation near 55 eV due to the Cooper minimum in the $5p_0 \rightarrow \epsilon d$ channel. Above 100 eV, the large variations observed in the group delay are due to the interference between the long and short trajectories.

Between 65 and 80 eV, the measured group delay from the TD-DFT simulation exhibits modulations due to the multielectron interaction. As described above, these modulations are associated with the phase of the matrix element describing the momentum transfer between the recollision electron and the ion through the Coulomb interaction. These variations are both observed in the calculated group delay, depicted in Fig. 9.3 and the C-SFA measurement result agrees with the TD-DFT result. The differences between the C-SFA and TD-DFT results are attributed to the use of first-order approximations in the C-SFA and other dynamics included in the C-SFA (e.g. ground state depletion, orbital distortion, etc...).

9.5 Conclusions

In this chapter, I demonstrated the importance of multielectron interaction in attosecond pulse emission from xenon using TD-DFT. The Coulomb interaction and resultant momentum transfer between the recollision electron and $4d$ sub-shell electrons was observed to excite the entire $n = 4$ shell and significantly affect the phase of attosecond pulse emission. The effect of these dynamics on the recollision electron wave packet was then described using an extension of the SFA which accounts for electron correlation and this was used to describe how these effects would manifest in an *in situ* measurement. This was then confirmed by a single-image *in situ* measurement simulated using TD-DFT, which clearly reflected the phase of the matrix element describing the Coulomb interaction between the recollision electron and the ion and the Cooper minimum near 55 eV.

The multielectron interaction observed here introduces two new parameters describing the recollision process (i.e. the transferred momentum and time of multielectron interaction). Consequently, higher-dimensional HHG-based spectroscopy [93] will be necessary to isolate and characterize the temporal and momentum dynamics of this multielectron interaction fully. Further, within this thesis, only forms of *in situ* measurement which used perturbing and driving fields with a parallel polarization were used. Due to the parallel polarization of the perturbing field, the perturbation-induced phase shift is sensitive to the change in transferred momentum due to the phase of the Coulomb interaction matrix element. In contrast, methods of *in situ* measurement which use a perpendicularly polarized field [26] will be insensitive to the change in transferred momentum and will provide a measurement related solely to the change in the times of recombination and multielectron interaction. This suggests the combination of perpendicular and parallel polarized *in situ* measurement can be used to isolate the momentum transfer dynamics unambiguously.

Summary: The *in situ* measurement of transition moment phase shifts due to electronic structure and multielectron interaction were demonstrated using time-dependent density functional theory simulations of recollision in xenon. The measurement of the Cooper minimum and phase shifts due to the energy and momentum transfer between the recollision electron and ion demonstrate that attosecond *in situ* measurement is ideally suited for the measurement of these effects.

Part IV

Conclusion

Chapter 10

Conclusions

In this thesis, I have demonstrated the feasibility of all-optical approaches in attosecond science to measure transition moment phase shifts due to electronic structure and multi-electron interaction. This was done by extending the strong field approximation to systems which exhibit a rapidly varying transition moment phase and describing *in situ* measurement within this framework. This analytical model was then confirmed using *ab initio* simulation and experiment. The sensitivity of all-optical measurement to such phase shifts was found to depend on the nature of the transition moment. In particular, all-optical approaches are insensitive to phase shifts due to ionic structure due to a first-order cancellation of the influence of the perturbing field on the recollision electron wave packet and the transition moment. The results from the studies of the Cooper minimum in argon and multielectron interaction in one-dimensional helium and xenon, however, demonstrate that all-optical approaches are sensitive to transition moment phase shifts due to electronic structure and dynamics.

Previous to this work, all-optical approaches were not thought possible. The three steps of the classical recollision model were thought of as independent and it was assumed that the recombination step was independent of the driving laser field. The sensitivity of all-optical methods to the transition moment phase, however, demonstrates that neither of these assumptions are generally true. The all-optical measurement of the group delay variation around the Cooper minimum in argon (done within the SFA in Chapter 6 and with *ab initio* theory and experiment in Chapter 8) demonstrate that the determination of the components of the recollision electron wave packet which dominate dipole emission is sensitive to the transition moment phase and that this sensitivity affects recollision trajectories. Further, the insensitivity of all-optical measurement to the transition moment phase in a diatomic molecule follows from the sensitivity of both the recollision electron wave packet to the transition moment and the influence of the perturbing field on the transition moment. Thus, the sensitivity of all-optical approaches to the transition moment phase has implications beyond measurement and will change how recollision processes and the effect of the transition moment are understood. In particular, the effect of the transition moment on the recollision electron wave packet requires that transition moment phase shifts be included in the saddle-point analysis typically employed in the SFA. While this complicates the simulation of recollision dynamics in complex systems, this greater complexity will allow for a

deeper understanding of electron dynamics in complex atomic and molecular systems.

Studies of the transition moment in attosecond science have typically been accomplished using photoionization-based measurement. These results illustrate an alternative route to these measurements which is advantageous in many ways. First, all-optical measurements can be performed with attosecond pulses of much lower energy than photoionization-based methods, as the measurement is observed entirely optically. This will become more important as attosecond science progresses towards the study of systems at higher energies because single-photon ionization cross-sections rapidly decrease with energy. Second, all-optical measurements are accomplished by manipulating infrared radiation and do not require a time-delayed XUV beam-line. This will permit more complex and higher-dimensional spectroscopies to be (comparatively) easily performed using techniques from conventional optics. Third, while both photoionization-based and all-optical measurement require an apparatus to generate and resolve the spectra of attosecond pulses, all-optical approaches do not require an additional photoelectron spectrometer. The simpler experimental design will allow any laboratory capable of generating high harmonic radiation to study transition moment phase shifts. Finally, all-optical measurements are insensitive to pulse propagation effects (e.g. dispersion in spectral filters) as the measurement is performed during the recollision process. Thus, these techniques experimentally unambiguously isolate electron dynamics and structure.

Over the past thirty years, attosecond science has grown into a mature science and has applications ranging from atomic to solid-state physics [11]. The extension of conventional atomic high harmonic spectroscopic methods to solid-state media has proven to be tremendously successful [103]. Many of the transition moment phase shifts studied here manifest in solid-state recollision processes [104, 105, 106, 107]. Compared with gas-phase HHG, solid-state HHG represents a new frontier for attosecond science. In particular, the prospect of studying HHG using all-optical measurements in strongly-correlated solid-state systems [108] is especially exciting given the focused sensitivity of *in situ* measurement to electronic structure and multielectron interaction. This focused sensitivity will allow for the measurement of correlated electron dynamics on their natural timescales in recollision processes, which will provide a rigorous experimental foundation for the development of theoretical methods describing dynamic electron correlation [109].

Appendix A

Code Access

The code for the one-dimensional helium and time-dependent density functional theory simulations can be obtained using the following hyperlinks:

— One-Dimensional Helium Code [https://github.com/graham-g-brown/2DTDSE/tree/main]
— TD-DFT Code [https://github.com/graham-g-brown/ggbTDDFT/tree/main]

In order to run the code, the following is needed:

— A computer running Linux
— An NVIDIA graphical processing unit of compute capability 3.5 or greater
— An installation of the NVIDIA-CUDA toolkit
— An installation of Python with the Numpy, Scipy, and MatplotLib libraries
— Time and patience.

Appendix B

The Classical Three-Step Model

The three-step recollision model is comprised of the following steps:

1. In the presence of a strong field, an electron is removed from an atom or molecule and enters the continuum near the ionic core with zero initial velocity at time t_b. This can occur any time within the strong field optical cycle.
2. The electron is accelerated by the strong field.
3. As the strong field oscillates, the electron is driven back towards and collides with its parent ion at time t_r. It enters into its initial state, emitting its excess energy as a photon.

I let the driving field be described by a sinusoidal vector potential $A(t)$ (vector notation is omitted):

$$A(t) = A_0 \sin(\omega_0 t). \tag{B.1}$$

The requirement that the electron be born with zero velocity requires the recollision electron canonical momentum k to satisfy the following:

$$0 = k + A(t_b) \implies k = -A(t_b). \tag{B.2}$$

With this, the kinetic momentum p of the electron in the continuum is

$$p(t) = A(t) - A(t_b). \tag{B.3}$$

Its kinetic energy K at time t_r is then

$$K(t_r) = \frac{(A(t_r) - A(t_b))^2}{2}. \tag{B.4}$$

The requirement that the electron return to its parent ion is then expressed by

$$0 = \int_{t_b}^{t_r} p(\tau) d\tau. \tag{B.5}$$

This equation can be solved numerically for times t_b and t_r which satisfy the displacement condition. Fig. B.1 (a) depicts solutions for t_b and t_r found by solving eq. (B.5) with eq.

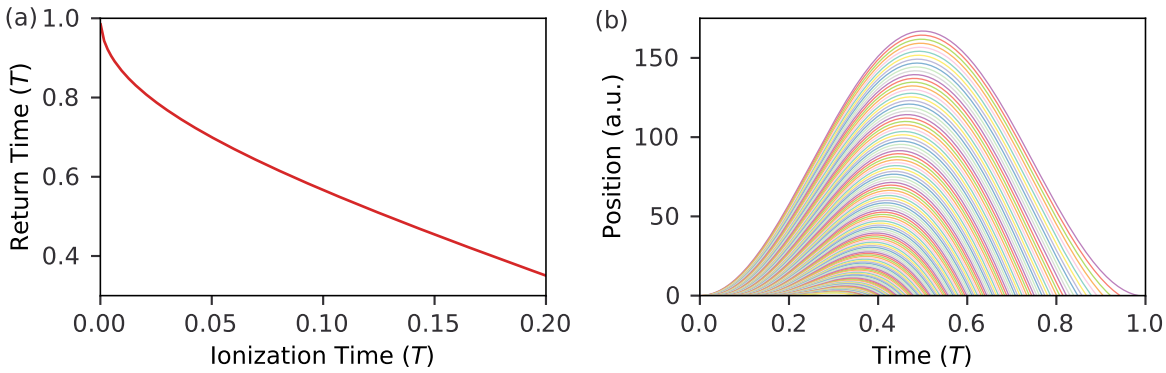

Figure B.1 – (a) The time of return t_r plotted against the ionization time t_b in units of the driving field period. (b) The recollision electron trajectories found by solving for t_b and t_r using eq. (B.5).

(B.1). Fig. B.1 (b) depicts the recollision electron trajectories $x(t)$ found with the solutions for t_b and t_r calculated according to

$$x(t) = \int_{t_b}^{t} p(\tau) d\tau. \tag{B.6}$$

With the solutions for t_b and t_r, the frequency Ω of the photon emitted upon recombination is

$$\Omega = K(t_r) + I_p. \tag{B.7}$$

With $I_p = 0$, the saddle-point equations for the time domain dipole moment in eqs. (2.43) and (2.43) reduce to the conditions for a zero initial velocity and return from the classical model in eqs. (B.2) and (B.6).

Bibliography

[1] P. B. Corkum. Plasma perspective on strong field multiphoton ionization. *Phys. Rev. Lett.*, **71**:1994–1997, Sep 1993. (Page 2, 3, 11, 12, 59, 98)

[2] M. Lewenstein, Ph. Balcou, M. Yu. Ivanov, Anne L'Huillier, and P. B. Corkum. Theory of high-harmonic generation by low-frequency laser fields. *Phys. Rev. A*, **49**:2117–2132, Mar 1994. (Page 2, 3, 4, 5, 13, 16, 59, 60, 92)

[3] K. C. Kulander, K. J. Schafer, and J. L. Krause. *Dynamics of Short-Pulse Excitation, Ionization and Harmonic Conversion*, pages 95–110. Springer US, Boston, MA, 1993. (Page 3)

[4] P. Salières, B. Carré, L. Le Déroff, F. Grasbon, G. G. Paulus, H. Walther, R. Kopold, W. Becker, D. B. Milošević, A. Sanpera, and M. Lewenstein. Feynman's Path-Integral Approach for Intense-Laser-Atom Interactions. *Science*, **292**(5518):902–905, 2001. (Page 3)

[5] David E. Manolopoulos. Derivation and reflection properties of a transmission-free absorbing potential. *The Journal of Chemical Physics*, **117**(21):9552–9559, 2002. (Page 3, 47, 54, 77, 87, 102, 110)

[6] K. Varjú II, Y. Mairesse, B. Carré, M. B. Gaarde, P. Johnsson, S. Kazamias, R. López-Martens, J. Mauritsson, K. J. Schafer, PH. Balcou, A. L'Huillier, and P. Salières. Frequency chirp of harmonic and attosecond pulses. *Journal of Modern Optics*, **52**(2-3):379–394, 2005. (Page 4)

[7] S. B. Schoun, R. Chirla, J. Wheeler, C. Roedig, P. Agostini, L. F. DiMauro, K. J. Schafer, and M. B. Gaarde. Attosecond Pulse Shaping around a Cooper Minimum. *Phys. Rev. Lett.*, **112**:153001, Apr 2014. (Page 4, 16, 17, 63, 85, 87, 92, 96)

[8] A. D. Shiner, B. E. Schmidt, C. Trallero-Herrero, H. J. Wörner, S. Patchkovskii, P. B. Corkum, J.-C. Kieffer, F. Légaré, and D. M. Villeneuve. Probing collective multi-electron dynamics in xenon with high-harmonic spectroscopy. *Nature Physics*, **7**(6):464–467, Jun 2011. (Page 4, 16, 40, 84, 98, 101)

[9] M. Spanner, J. B. Bertrand, and D. M. Villeneuve. In situ attosecond pulse characterization techniques to measure the electromagnetic phase. *Phys. Rev. A*, **94**:023825, Aug 2016. (Page 4, 5, 19, 34, 35, 54, 60, 62, 65, 70, 76, 77, 78, 83)

[10] C. Vozzi, F. Calegari, E. Benedetti, J.-P. Caumes, G. Sansone, S. Stagira, M. Nisoli, R. Torres, E. Heesel, N. Kajumba, J. P. Marangos, C. Altucci, and R. Velotta. Controlling Two-Center Interference in Molecular High Harmonic Generation. *Phys. Rev. Lett.*, **95**:153902, Oct 2005. (Page 4, 60, 62)

[11] G. Vampa, C. R. McDonald, G. Orlando, P. B. Corkum, and T. Brabec. Semiclassical analysis of high harmonic generation in bulk crystals. *Phys. Rev. B*, **91**:064302, Feb 2015. (Page 4, 98, 115)

[12] Tran Trung Luu, Zhong Yin, Arohi Jain, Thomas Gaumnitz, Yoann Pertot, Jun Ma, and Hans Jakob Wörner. Extreme–ultraviolet high–harmonic generation in liquids. *Nature Communications*, **9**(1):3723, Sep 2018. (Page 4, 98)

[13] Eleftherios Goulielmakis, Zhi-Heng Loh, Adrian Wirth, Robin Santra, Nina Rohringer, Vladislav S. Yakovlev, Sergey Zherebtsov, Thomas Pfeifer, Abdallah M. Azzeer, Matthias F. Kling, Stephen R. Leone, and Ferenc Krausz. Real-time observation of valence electron motion. *Nature*, **466**(7307):739–743, Aug 2010. (Page 4)

[14] A. Kaldun, A. Blättermann, V. Stooß, S. Donsa, H. Wei, R. Pazourek, S. Nagele, C. Ott, C. D. Lin, J. Burgdörfer, and T. Pfeifer. Observing the ultrafast buildup of a Fano resonance in the time domain. *Science*, **354**(6313):738–741, 2016. (Page 4)

[15] E. L. Falc ao Filho, V. M. Gkortsas, Ariel Gordon, and Franz X. Kärtner. Analytic scaling analysis of high harmonic generation conversion efficiency. *Opt. Express*, **17**(13):11217–11229, Jun 2009. (Page 4)

[16] Xiaoming Ren, Jie Li, Yanchun Yin, Kun Zhao, Andrew Chew, Yang Wang, Shuyuan Hu, Yan Cheng, Eric Cunningham, Yi Wu, Michael Chini, and Zenghu Chang. Attosecond light sources in the water window. *Journal of Optics*, **20**(2):023001, jan 2018. (Page 4)

[17] Anthony Starace. *Photoionization of Atoms*, pages 379–390. Springer New York, New York, NY, 2006. (Page 5)

[18] A. D. Shiner, C. Trallero-Herrero, N. Kajumba, H.-C. Bandulet, D. Comtois, F. Légaré, M. Giguère, J-C. Kieffer, P. B. Corkum, and D. M. Villeneuve. Wavelength Scaling of High Harmonic Generation Efficiency. *Phys. Rev. Lett.*, **103**:073902, Aug 2009. (Page 5)

[19] N. Dudovich, O. Smirnova, J. Levesque, Y. Mairesse, M. Yu. Ivanov, D. M. Villeneuve, and P. B. Corkum. Measuring and controlling the birth of attosecond XUV pulses. *Nature Physics*, **2**(11):781–786, Nov 2006. (Page 5, 25, 26, 29, 32, 60, 62)

[20] Olga Smirnova, Michael Spanner, and Misha Ivanov. Anatomy of strong field ionization II: to dress or not to dress? *Journal of Modern Optics*, **54**(7):1019–1038, 2007. (Page 8)

[21] Arjun Nayak, Mathieu Dumergue, Sergei Kühn, Sudipta Mondal, Tamás Csizmadia, N.G. Harshitha, Miklós Füle, Mousumi Upadhyay Kahaly, Balázs Farkas, Balázs Major, Viktor Szaszkó-Bogár, Péter Födi, Szilárd Majorosi, Nikolaos Tsatrafyllis, Emmanuel Skantzakis, Lana Neoricic, Mojtaba Shirozhan, Giulio Vampa, Katalin Varjú, Paraskevas Tzallas, Giuseppe Sansone, Dimitris Charalambidis, and Subhendu Kahaly. Saddle point approaches in strong field physics and generation of attosecond pulses. *Physics Reports*, **833**:1–52, 2019. (Page 10)

[22] Jan Rothhardt, Manuel Krebs, Steffen Hädrich, Stefan Demmler, Jens Limpert, and Andreas Tünnermann. Absorption-limited and phase-matched high harmonic generation in the tight focusing regime. **16**(3):033022, mar 2014. (Page 13)

[23] Emilio Pisanty, Marcelo F Ciappina, and Maciej Lewenstein. The imaginary part of the high-harmonic cutoff. *Journal of Physics: Photonics*, **2**(3):034013, jul 2020. (Page 16)

[24] Anh-Thu Le, R. R. Lucchese, S. Tonzani, T. Morishita, and C. D. Lin. Quantitative rescattering theory for high-order harmonic generation from molecules. *Phys. Rev. A*, **80**:013401, Jul 2009. (Page 16, 17, 59, 61, 85, 88, 97)

[25] Olga Smirnova and Misha Ivanov. *Multielectron High Harmonic Generation: Simple Man on a Complex Plane*, chapter 7, pages 201–256. John Wiley & Sons, Ltd, 2014. (Page 17)

[26] Dror Shafir, Hadas Soifer, Barry D. Bruner, Michal Dagan, Yann Mairesse, Serguei Patchkovskii, Misha Yu. Ivanov, Olga Smirnova, and Nirit Dudovich. Resolving the time when an electron exits a tunnelling barrier. *Nature*, **485**(7398):343–346, May 2012. (Page 17, 25, 91, 97, 112)

[27] Marie Labeye, Fran çois Risoud, Camille Lévêque, Jérémie Caillat, Alfred Maquet, Tahir Shaaran, Pascal Salières, and Richard Taïeb. Dynamical distortions of structural signatures in molecular high-order harmonic spectroscopy. *Phys. Rev. A*, **99**:013412, Jan 2019. (Page 17, 65, 66, 67, 77)

[28] D Faccialà, S Pabst, B D Bruner, A G Ciriolo, M Devetta, M Negro, P Prasannan Geetha, A Pusala, H Soifer, N Dudovich, S Stagira, and C Vozzi. High-order harmonic generation spectroscopy by recolliding electron caustics. *Journal of Physics B: Atomic, Molecular and Optical Physics*, **51**(13):134002, jun 2018. (Page 17)

[29] Dong Hyuk Ko, Graham G. Brown, Chunmei Zhang, and P. B. Corkum. Near-field imaging of dipole emission modulated by an optical grating, 2020. (Page 19, 25, 32)

[30] I. Orfanos, I. Makos, I. Liontos, E. Skantzakis, B. Förg, D. Charalambidis, and P. Tzallas. Attosecond pulse metrology. *APL Photonics*, **4**(8):080901, 2019. (Page 19, 23)

[31] Kyung Taec Kim, D. M. Villeneuve, and P. B. Corkum. Manipulating quantum paths for novel attosecond measurement methods. *Nature Photonics*, **8**(3):187–194, Mar 2014. (Page 19, 25)

[32] P. M. Paul, E. S. Toma, P. Breger, G. Mullot, F. Augé, Ph. Balcou, H. G. Muller, and P. Agostini. Observation of a Train of Attosecond Pulses from High Harmonic Generation. *Science*, **292**(5522):1689–1692, 2001. (Page 20, 26, 65)

[33] Valérie Véniard, Richard Taïeb, and Alfred Maquet. Phase dependence of (N+1)-color (N>1) ir-uv photoionization of atoms with higher harmonics. *Phys. Rev. A*, **54**:721–728, Jul 1996. (Page 21)

[34] V. Gruson, L. Barreau, Á. Jiménez-Galan, F. Risoud, J. Caillat, A. Maquet, B. Carré, F. Lepetit, J.-F. Hergott, T. Ruchon, L. Argenti, R. Taïeb, F. Martín, and P. Salières. Attosecond dynamics through a Fano resonance: Monitoring the birth of a photoelectron. *Science*, **354**(6313):734–738, 2016. (Page 22)

[35] T. J. Hammond, Graham G. Brown, Kyung Taec Kim, D. M. Villeneuve, and P. B. Corkum. Attosecond pulses measured from the attosecond lighthouse. *Nature Photonics*, **10**(3):171–175, Mar 2016. (Page 22, 24)

[36] D.J. Kane and R. Trebino. Characterization of arbitrary femtosecond pulses using frequency-resolved optical gating. *IEEE Journal of Quantum Electronics*, **29**(2):571–579, 1993. (Page 22, 23)

[37] J. Itatani, F. Quéré, G. L. Yudin, M. Yu. Ivanov, F. Krausz, and P. B. Corkum. Attosecond Streak Camera. *Phys. Rev. Lett.*, **88**:173903, Apr 2002. (Page 22)

[38] M. Hentschel, R. Kienberger, Ch. Spielmann, G. A. Reider, N. Milosevic, T. Brabec, P. Corkum, U. Heinzmann, M. Drescher, and F. Krausz. Attosecond metrology. *Nature*, **414**(6863):509–513, Nov 2001. (Page 22)

[39] Kyung Taec Kim, Chunmei Zhang, Andrew D. Shiner, Sean E. Kirkwood, Eugene Frumker, Genevieve Gariepy, Andrei Naumov, D. M. Villeneuve, and P. B. Corkum. Manipulation of quantum paths for space–time characterization of attosecond pulses. *Nature Physics*, **9**(3):159–163, Mar 2013. (Page 25, 26, 30, 32, 94)

[40] Chunmei Zhang, Graham G. Brown, , Dong Hyuk Ko, and Paul B. Corkum. Optical Measurement of Photorecombination Time Delays, 2021. (Page 30, 45, 64, 65, 85, 88)

[41] Chunmei Zhang, Graham G. Brown, Kyung Taec Kim, D. M. Villeneuve, and P. B. Corkum. Full characterization of an attosecond pulse generated using an infrared driver. *Scientific Reports*, **6**(1):26771, May 2016. (Page 30, 32)

[42] *Ab Initio Theory of Electronic Structure*, pages 3–43. (Page 38)

[43] Cleanthes Anthony Nicolaides. Attosecond-Resolved Electron Dynamics in Many-Electron Atoms: Quantitative Theory and Comparison with Measurements. *Applied Sciences*, **8**(4), 2018. (Page 39)

[44] Charlotte Fischer. *Atomic Structure: Multiconfiguration Hartree-Fock Theories*, pages 307–323. Springer New York, New York, NY, 2006. (Page 39)

[45] Loren Greenman, Phay J. Ho, Stefan Pabst, Eugene Kamarchik, David A. Mazziotti, and Robin Santra. Implementation of the time-dependent configuration-interaction singles method for atomic strong-field processes. *Phys. Rev. A*, **82**:023406, Aug 2010. (Page 39)

[46] John M. Dawson. Particle simulation of plasmas. *Rev. Mod. Phys.*, **55**:403–447, Apr 1983. (Page 39)

[47] M. S. Pindzola, D. C. Griffin, and C. Bottcher. Validity of time-dependent Hartree-Fock theory for the multiphoton ionization of atoms. *Phys. Rev. Lett.*, **66**:2305–2307, May 1991. (Page 39)

[48] Neepa T. Maitra. Perspective: Fundamental aspects of time-dependent density functional theory. *The Journal of Chemical Physics*, **144**(22):220901, 2016. (Page 39, 40, 44)

[49] Kieron Burke. Perspective on density functional theory. *The Journal of Chemical Physics*, **136**(15):150901, 2012. (Page 40, 42, 53)

[50] Robert G. Parr. Density Functional Theory of Atoms and Molecules. In Kenichi Fukui and Bernard Pullman, editors, *Horizons of Quantum Chemistry*, pages 5–15, Dordrecht, 1980. Springer Netherlands. (Page 40)

[51] Karlheinz Schwarz and Peter Blaha. *DFT Calculations for Real Solids*, chapter 8, pages 227–259. American Cancer Society, 2017. (Page 40)

[52] A. S. de Wijn, M. Lein, and S. Kümmel. Strong-field ionization in time-dependent density functional theory. *Europhysics Letters*, **84**(4):43001, Nov 2008. (Page 40)

[53] P. Hohenberg and W. Kohn. Inhomogeneous Electron Gas. *Phys. Rev.*, **136**:B864–B871, Nov 1964. (Page 40)

[54] R. van Leeuwen and E. J. Baerends. Exchange-correlation potential with correct asymptotic behavior. *Phys. Rev. A*, **49**:2421–2431, Apr 1994. (Page 42, 53, 88, 99, 100)

[55] Erich Runge and E. K. U. Gross. Density-Functional Theory for Time-Dependent Systems. *Phys. Rev. Lett.*, **52**:997–1000, Mar 1984. (Page 43)

[56] Makenzie R. Provorse and Christine M. Isborn. Electron dynamics with real-time time-dependent density functional theory. *International Journal of Quantum Chemistry*, **116**(10):739–749, 2016. (Page 43)

[57] G. G. Brown, D. H. Ko, C. Zhang, and P. B. Corkum. Measuring and controlling resonance-enhanced recollision with infrared fields. *Phys. Rev. X (submitted)*, 2021. (Page 45, 73)

[58] Graham G. Brown, Dong Hyuk Ko, Chunmei Zhang, and P. B. Corkum. Characterizing multielectron dynamics during recollision, 2020. (Page 45)

[59] M.D Feit, J.A Fleck, and A Steiger. Solution of the Schrödinger equation by a spectral method. *Journal of Computational Physics*, **47**(3):412–433, 1982. (Page 46)

[60] NVIDIA, Péter Vingelmann, and Frank H.P. Fitzek. CUDA, release: 10.2.89, 2020. (Page 47)

[61] Jingyan Wang, Shih-I Chu, and Cecil Laughlin. Multiphoton detachment of H^-. II. Intensity-dependent photodetachment rates and threshold behavior—complex-scaling generalized pseudospectral method. *Phys. Rev. A*, **50**:3208–3215, Oct 1994. (Page 48)

[62] G. I. El-Baghdady, M. El-Azab, and W. S. El-Beshbeshy. Legendre-gauss-lobatto pseudo-spectral method for one-dimensional advection-diffusion equation. 2015. (Page 49)

[63] John David Jackson. *Classical Electrodynamics; 2nd ed.* Wiley, New York, NY, 1975. (Page 49)

[64] E. P. Wigner. *On the Matrices Which Reduce the Kronecker Products of Representations of S. R. Groups*, pages 608–654. Springer Berlin Heidelberg, Berlin, Heidelberg, 1993. (Page 49)

[65] G. Kresse and J. Furthmüller. Efficient iterative schemes for ab initio total-energy calculations using a plane-wave basis set. *Phys. Rev. B*, **54**:11169–11186, Oct 1996. (Page 53)

[66] Serguei Patchkovskii and H.G. Muller. Simple, accurate, and efficient implementation of 1-electron atomic time-dependent Schrödinger equation in spherical coordinates. *Computer Physics Communications*, **199**:153–169, 2016. (Page 54)

[67] *Computational strong-field quantum dynamics Intense light-matter interactions*. De Gruyter, Germany, 2017. CLASSICAL AND QUANTUM MECHANICS, GENERAL PHYSICS. (Page 57)

[68] Franklin F. Kuo and James F. Kaiser. *System analysis by digital computer*. Wiley, New York, 1966. (Page 57)

[69] G. G. Brown, D. H. Ko, C. Zhang, and P. B. Corkum. Attosecond measurement via high harmonic generation by low frequency fields. *Phys. Rev. A (submitted)*, 2021. (Page 59)

[70] Anh-Thu Le, Toru Morishita, and C. D. Lin. Extraction of the species-dependent dipole amplitude and phase from high-order harmonic spectra in rare-gas atoms. *Phys. Rev. A*, **78**:023814, Aug 2008. (Page 59)

[71] John W. Cooper. Photoionization from Outer Atomic Subshells. A Model Study. *Phys. Rev.*, **128**:681–693, Oct 1962. (Page 60, 62, 63, 85)

[72] Gal Orenstein, Oren Pedatzur, Ayelet J. Uzan, Barry D. Bruner, Yann Mairesse, and Nirit Dudovich. Isolating strong-field dynamics in molecular systems. *Phys. Rev. A*, **95**:051401, May 2017. (Page 60, 62, 71)

[73] A. Ferré, A. E. Boguslavskiy, M. Dagan, V. Blanchet, B. D. Bruner, F. Burgy, A. Camper, D. Descamps, B. Fabre, N. Fedorov, J. Gaudin, G. Geoffroy, J. Mikosch, S. Patchkovskii, S. Petit, T. Ruchon, H. Soifer, D. Staedter, I. Wilkinson, A. Stolow, N. Dudovich, and Y. Mairesse. Multi-channel electronic and vibrational dynamics in polyatomic resonant high-order harmonic generation. *Nature Communications*, **6**(1):5952, Jan 2015. (Page 71)

[74] U. Fano. Effects of Configuration Interaction on Intensities and Phase Shifts. *Phys. Rev.*, **124**:1866–1878, Dec 1961. (Page 79, 80)

[75] Xiaoxu Guan, Xiao-Min Tong, and Shih-I Chu. Effect of electron correlation on high-order-harmonic generation of helium atoms in intense laser fields: Time-dependent generalized pseudospectral approach in hyperspherical coordinates. *Phys. Rev. A*, **73**:023403, Feb 2006. (Page 79)

[76] Jan Rothhardt, Steffen Hädrich, Stefan Demmler, Manuel Krebs, Stephan Fritzsche, Jens Limpert, and Andreas Tünnermann. Enhanced high harmonic generation by Fano resonances. In *Research in Optical Sciences*, page HW3C.6. Optical Society of America, 2014. (Page 80)

[77] R. A. Ganeev, Z. Abdelrahman, F. Frank, T. Witting, W. A. Okell, D. Fabris, C. Hutchison, J. P. Marangos, and J. W. G. Tisch. Spatial coherence measurements of non-resonant and resonant high harmonics generated in laser ablation plumes, journal = Applied Physics Letters. **104**(2):021122, 2014. (Page 80)

[78] W.-C. Chu and C. D. Lin. Theory of ultrafast autoionization dynamics of Fano resonances. *Phys. Rev. A*, **82**:053415, Nov 2010. (Page 80)

[79] Marlene Wickenhauser, Joachim Burgdörfer, Ferenc Krausz, and Markus Drescher. Time Resolved Fano Resonances. *Phys. Rev. Lett.*, **94**:023002, Jan 2005. (Page 81)

[80] Christian Ott, Andreas Kaldun, Philipp Raith, Kristina Meyer, Martin Laux, Jörg Evers, Christoph H. Keitel, Chris H. Greene, and Thomas Pfeifer. Lorentz Meets Fano in Spectral Line Shapes: A Universal Phase and Its Laser Control. *Science*, **340**(6133):716–720, 2013. (Page 81, 82)

[81] L. Argenti, Á. Jiménez-Galán, C. Marante, C. Ott, T. Pfeifer, and F. Martín. Dressing effects in the attosecond transient absorption spectra of doubly excited states in helium. *Phys. Rev. A*, **91**:061403, Jun 2015. (Page 81, 82)

[82] Jing Zhao and Manfred Lein. Probing Fano resonances with ultrashort pulses. *New Journal of Physics*, **14**(6):065003, jun 2012. (Page 82)

[83] M. Ruggenthaler, S. V. Popruzhenko, and D. Bauer. Recollision-induced plasmon excitation in strong laser fields. *Phys. Rev. A*, **78**:033413, Sep 2008. (Page 84)

[84] Renate Pazourek, Stefan Nagele, and Joachim Burgdörfer. Time-resolved photoemission on the attosecond scale: opportunities and challenges. *Faraday Discuss.*, **163**:353–376, 2013. (Page 85)

[85] J. Higuet, H. Ruf, N. Thiré, R. Cireasa, E. Constant, E. Cormier, D. Descamps, E. Mével, S. Petit, B. Pons, Y. Mairesse, and B. Fabre. High-order harmonic spectroscopy of the Cooper minimum in argon: Experimental and theoretical study. *Phys. Rev. A*, **83**:053401, May 2011. (Page 85)

[86] M. C. H. Wong, A.-T. Le, A. F. Alharbi, A. E. Boguslavskiy, R. R. Lucchese, J.-P. Brichta, C. D. Lin, and V. R. Bhardwaj. High Harmonic Spectroscopy of the Cooper Minimum in Molecules. *Phys. Rev. Lett.*, **110**:033006, Jan 2013. (Page 85)

[87] J. Kirz, D. Attwood, B. Henke, M. Howells, K. Kennedy, K. Kim, J. B. Kortright, R.C.C. Perera, P. Pianetta, J.C. Riordan, J.H. Scofield, G.L. Stradling, A.C. Thompson, J.H. Underwood, D. Vaughan, G.P. Williams, and H. Winick. *X-ray Data Booklet*. Lawrence Berkeley National Laboratory. LBNL Report #: PUB-490, 2009. (Page 87, 99)

[88] Liang-Wen Pi and Alexandra S. Landsman. Attosecond Time Delay in Photoionization of Noble-Gas and Halogen Atoms. *Applied Sciences*, 8(3):322, Feb 2018. (Page 87, 92, 93, 98, 100)

[89] Stefan Pabst, Loren Greenman, David A. Mazziotti, and Robin Santra. Impact of multichannel and multipole effects on the Cooper minimum in the high-order-harmonic spectrum of argon. *Phys. Rev. A*, **85**:023411, Feb 2012. (Page 88, 90, 91)

[90] H. G. Muller. Numerical simulation of high-order above-threshold-ionization enhancement in argon. *Phys. Rev. A*, **60**:1341–1350, Aug 1999. (Page 88)

[91] J M Dahlström, A L'Huillier, and J Mauritsson. Quantum mechanical approach to probing the birth of attosecond pulses using a two-colour field. *Journal of Physics B: Atomic, Molecular and Optical Physics*, **44**(9):095602, apr 2011. (Page 92)

[92] J. P. Farrell, L. S. Spector, B. K. McFarland, P. H. Bucksbaum, M. Gühr, M. B. Gaarde, and K. J. Schafer. Influence of phase matching on the Cooper minimum in Ar high-order harmonic spectra. *Phys. Rev. A*, **83**:023420, Feb 2011. (Page 95)

[93] Valeria Serbinenko and Olga Smirnova. Multidimensional high harmonic spectroscopy: a semi-classical perspective on measuring multielectron rearrangement upon ionization. *Journal of Physics B: Atomic, Molecular and Optical Physics*, **46**(17):171001, aug 2013. (Page 97, 112)

[94] Serguei Patchkovskii, Olga Smirnova, and Michael Spanner. Attosecond control of electron correlations in one-photon ionization and recombination. *Journal of Physics B: Atomic, Molecular and Optical Physics*, **45**(13):131002, jun 2012. (Page 98, 99, 101, 102, 104, 105, 106, 107)

[95] G. G. Brown, D. H. Ko, C. Zhang, and P. B. Corkum. Characterizing many-body dynamics by perturbing electron-ion collisions with infrared fields. *(in preparation)*, 2021. (Page 98)

[96] J. P. Connerade. *Giant resonances in atoms, molecules, and solids*. Plenum Press, New York, 1987. (Page 98)

[97] Shiyang Zhong, Jimmy Vinbladh, David Busto, Richard J. Squibb, Marcus Isinger, Lana Neoričić, Hugo Laurell, Robin Weissenbilder, Cord L. Arnold, Raimund Feifel, Jan Marcus Dahlstr¨ om, Göran Wendin, Mathieu Gisselbrecht, Eva Lindroth, and Anne L'Huillier. Attosecond electron–spin dynamics in Xe 4d photoionization. *Nature Communications*, **11**(1):5042, Oct 2020. (Page 99)

[98] Anthony F. Starace. Photoionization of Argon and Xenon Including Final-State Correlation. *Phys. Rev. A*, **2**:118–121, Jul 1970. (Page 101)

[99] G. Snell, U. Hergenhahn, N. Müller, M. Drescher, J. Viefhaus, U. Becker, and U. Heinzmann. Study of xenon $4d$, $5p$, and $5s$ photoionization in the shape-resonance region using spin-resolved electron spectroscopy. *Phys. Rev. A*, **63**:032712, Feb 2001. (Page 101)

[100] Jingtao Zhang and D.-S. Guo. Spectral Minimum and Giant Enhancement in Photoelectron Spectra from Xenon Atoms Driven by Intense Midinfrared Laser Fields. *Phys. Rev. Lett.*, **110**:063002, Feb 2013. (Page 101)

[101] Stefan Pabst and Robin Santra. Strong-Field Many-Body Physics and the Giant Enhancement in the High-Harmonic Spectrum of Xenon. *Phys. Rev. Lett.*, **111**:233005, Dec 2013. (Page 101, 108)

[102] Gennady L. Yudin and Misha Yu. Ivanov. Nonadiabatic tunnel ionization: Looking inside a laser cycle. *Phys. Rev. A*, **64**:013409, Jun 2001. (Page 101)

[103] G. Vampa, T. J. Hammond, N. Thiré, B. E. Schmidt, F. Légaré, C. R. McDonald, T. Brabec, D. D. Klug, and P. B. Corkum. All-Optical Reconstruction of Crystal Band Structure. *Phys. Rev. Lett.*, **115**:193603, Nov 2015. (Page 115)

[104] S. L. Molodtsov, S. V. Halilov, V. D. P. Servedio, W. Schneider, S. Danzenbächer, J. J. Hinarejos, Manuel Richter, and C. Laubschat. Cooper Minima in the Photoemission Spectra of Solids. *Phys. Rev. Lett.*, **85**:4184–4187, Nov 2000. (Page 115)

[105] Hanzhe Liu, Yilei Li, Yong Sing You, Shambhu Ghimire, Tony F. Heinz, and David A. Reis. High-harmonic generation from an atomically thin semiconductor. *Nature Physics*, **13**(3):262–265, Mar 2017. (Page 115)

[106] H. Allmaier, L. Chioncel, and E. Arrigoni. Titanium nitride: A correlated metal at the threshold of a Mott transition. *Phys. Rev. B*, **79**:235126, Jun 2009. (Page 115)

[107] A. Korobenko, S. Saha, A. T. K. Godfrey, M. Gertsvolf, A. Yu. Naumov, D. M. Villeneuve, A. Boltasseva, V. M. Shalaev, and P. B. Corkum. High-harmonic generation in metallic titanium nitride. *Nature Communications*, **12**(1):4981, Aug 2021. (Page 115)

[108] R. E. F. Silva, Igor V. Blinov, Alexey N. Rubtsov, O. Smirnova, and M. Ivanov. High-harmonic spectroscopy of ultrafast many-body dynamics in strongly correlated systems. *Nature Photonics*, **12**(5):266–270, May 2018. (Page 115)

[109] G. Kotliar, S. Y. Savrasov, K. Haule, V. S. Oudovenko, O. Parcollet, and C. A. Marianetti. Electronic structure calculations with dynamical mean-field theory. *Rev. Mod. Phys.*, **78**:865–951, Aug 2006. (Page 115)